A diagnostic study on two low pressure plasma sources

Citation for published version (APA):
Grift, van de, M. (1997). *A diagnostic study on two low pressure plasma sources*. [Phd Thesis 1 (Research TU/e / Graduation TU/e), Applied Physics and Science Education]. Technische Universiteit Eindhoven. https://doi.org/10.6100/IR501160

DOI:
10.6100/IR501160

Document status and date:
Published: 01/01/1997

Document Version:
Publisher’s PDF, also known as Version of Record (includes final page, issue and volume numbers)

Please check the document version of this publication:

• A submitted manuscript is the version of the article upon submission and before peer-review. There can be important differences between the submitted version and the official published version of record. People interested in the research are advised to contact the author for the final version of the publication, or visit the DOI to the publisher's website.
• The final author version and the galley proof are versions of the publication after peer review.
• The final published version features the final layout of the paper including the volume, issue and page numbers.

Link to publication

General rights
Copyright and moral rights for the publications made accessible in the public portal are retained by the authors and/or other copyright owners and it is a condition of accessing publications that users recognise and abide by the legal requirements associated with these rights.

- Users may download and print one copy of any publication from the public portal for the purpose of private study or research.
- You may not further distribute the material or use it for any profit-making activity or commercial gain
- You may freely distribute the URL identifying the publication in the public portal.

If the publication is distributed under the terms of Article 25fa of the Dutch Copyright Act, indicated by the “Taverne” license above, please follow below link for the End User Agreement:

www.tue.nl/taverne

Take down policy
If you believe that this document breaches copyright please contact us at:

openaccess@tue.nl

providing details and we will investigate your claim.

Download date: 04. Oct. 2023

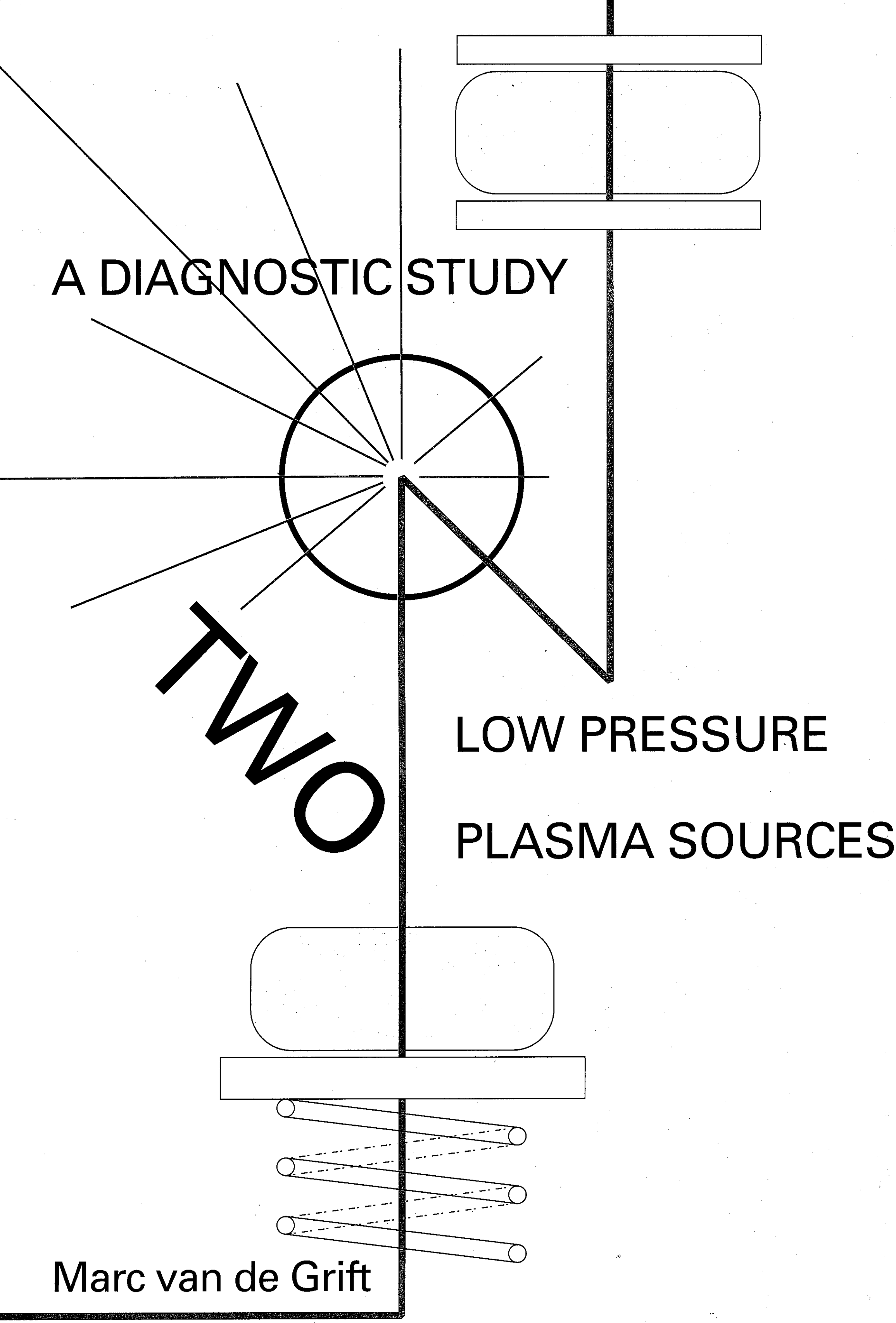

A DIAGNOSTIC STUDY

TWO

LOW PRESSURE
PLASMA SOURCES

Marc van de Grift

A DIAGNOSTIC STUDY ON TWO LOW PRESSURE PLASMA SOURCES

PROEFSCHRIFT

ter verkrijging van de graad van doctor aan de
Technische Universiteit Eindhoven, op gezag van de
Rector Magnificus, prof.dr. M. Rem, voor een
commissie aangewezen door het College voor
Promoties in het openbaar te verdedigen
op maandag 1 december 1997 om 16.00 uur

door

Marc van de Grift

geboren te Eindhoven

Dit proefschrift is goedgekeurd door de promotoren :

prof.dr. F.J. de Hoog

en

dr. N. Sadeghi

Copromotor :

dr.ir. G.M.W. Kroesen

CIP-DATA LIBRARY TECHNISCHE UNIVERSITEIT EINDHOVEN

Grift, Marc van de

A diagnostic study on two low pressure plasma sources / Marc van de Grift. -
Eindhoven : Technische Universiteit Eindhoven, 1997. - Proefschrift. -
ISBN 90-386-0597-8
NUGI 812
Trefw. : radiofrequent plasma / plasma-etsen / plasmadiagnostiek / argonplasma.
Subject headings: plasma devices / plasma production / plasma diagnostics.

Druk: Boek- en Offsetdrukkerij Letru, Helmond, (0492) 59 07 60

“Absence of evidence is not
the same as evidence of
absence”
dr. Carl Sagan (1934-1996)

Dit proefschrift draag
ik op aan mijn ouders,
Rob en Lenny.

Contents

1 Introduction 1

1.1 Plasmas 1
1.2 Plasma etching 1
1.3 Sources for plasma etching 3
  1.3.1 Capacitively coupled plasma (CCP) sources 3
  1.3.2 High density plasma (HDP) sources 4
1.4 Scope of this thesis 6

2 Aspects of radiation and plasma physics 9

2.1 Plasma physics 9
  2.1.1 General 9
  2.1.2 Collisions 13
2.2 Principles of radiation 15
  2.2.1 The classical atom model 15
2.3 The shape of spectral lines 16
  2.3.1 Natural linewidth 16
  2.3.2 Pressure broadening 18
  2.3.3 Transit time broadening 18
  2.3.4 Doppler broadening 18
  2.3.5 Voigt profile 20
2.4 Electronic transitions by radiation 20
  2.4.1 Absorption and stimulated emission : Einstein coefficients 20
  2.4.2 Absorption 23
  2.4.3 A two level system 24
    2.4.3.1 Homogeneously-broadened transitions : saturation 24
    2.4.3.2 Inhomogeneously-broadened transitions : hole burning 26
2.5 Doppler shifted laser induced fluorescence (DSLIF) 28
  2.5.1 A 3-level system 28

3 The Bohm criterion and presheath theory 33

3.1 Introduction 33
3.2 Sheath theory 33
3.3 Presheath formation 35
3.4 Modifications of the sheath - presheath theory 40

4 Plasma diagnostics 43

4.1 Introduction 43
4.2 Optical emission spectroscopy (OES) 43

4.3 Laser absorption spectroscopy 44
4.4 Langmuir probe 47
  4.4.1 Single probe theory 47
  4.4.2 Double probe theory 49
  4.4.3 Probe setup 52
4.5 Doppler shifted laser induced fluorescence (DSLIF) 54

5 Characterization of the 450 kHz plasma reactor 61

5.1 Introduction 61
5.2 Setup of the 450 kHz capacitively coupled, parallel plate plasma reactor 64
5.3 Measurements 67
  5.3.1 Langmuir probe 67
  5.3.2 IR laser absorption spectroscopy 70
  5.3.3 Doppler shifted laser induced fluorescence (DSLIF) 72
  5.3.4 Optical emission spectroscopy 77
5.4 1 dimensional fluid model 80
5.5 Conclusions 83

6 Transport of argon ions in a high density, inductively coupled plasma reactor 87

6.1 Introduction 87
6.2 Setup of the 13.56 MHz inductively coupled plasma reactor 88
6.3 Measurements 90
  6.3.1 IR laser absorption spectroscopy 90
  6.3.2 Langmuir probe 93
  6.3.3 Optical emission spectroscopy 100
  6.3.4 Doppler shifted laser induced fluorescence (DSLIF) 102
6.4 Monte-Carlo model 106
6.5 Conclusions 111

Appendix A : Argon data 115

Appendix B : Used symbols and abbreviations 121

Summary 127

Samenvatting 131

Dankwoord 135

Over de auteur 135

1. Introduction

1.1. Plasmas

In our every day life, we are used to arrange matter in our universe into three phases : solids, liquids, and gases. In ancient Greek society, the philosopher Aristotle distinguished four phases : earth, water, air and fire. The first three show a resemblance with the phases we use today. The last phase can be compared to what we call a plasma, a (partially) ionized gas. The plasma state is often named "the fourth phase". Although the word is relatively unknown, most of our universe is filled with plasma. Stars like the sun and stellar coronas are examples of cosmic plasmas. Lightning and fire are more familiar types of natural plasmas. Intensive research has lead to the use of various kinds of plasma configurations in industrial applications. Fusion reactors use plasmas of very high ion energies, exceeding 1keV (1 eV = 1 electron volt = $11.6\cdot10^3$ K). In street lights and neon tubes plasmas are used because of their efficient production of radiation. For the fabrication of integrated circuits (IC's), plasmas are commonly used for etching and deposition purposes. For deposition, the plasmas produce reactive species which are deposited on the substrate to make thin layers. For etching, structures with steep walls are created by enhanced etching perpendicular to the surface, caused by a directed flux of ions from the plasma.

1.2. Plasma etching

The reason for the success of plasma etching is that the process is highly anisotropic. Conventional, wet etching techniques use chemical etchants to selectively remove substrate material, without affecting the mask which covers other areas. Most of these

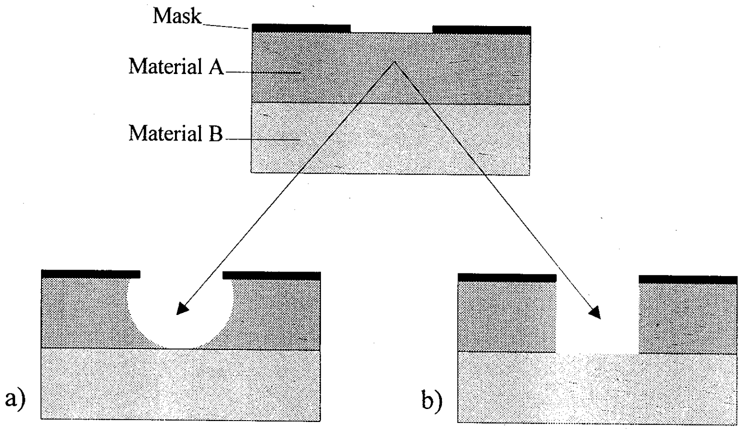

Figure 1.1 : Structures created by isotropic (a) and anisotropic (b) etching.

processes are isotropic because there is no preferential direction for etching. Typical structures as in figure. 1.1a are created with this method. The etchant is highly selective on substrate material A and not, or less active on material B.

The need for smaller structures to produce more components per unit area has increased the interest in plasma etching. Plasmas are able to etch structures with steep walls, as shown in figure 1.1b.

Four different etch mechanisms can be distinguished in the plasma :

1. *physical sputtering* : The ions from the plasma bombard the surface with typical energies of 1000 eV, which are much higher than the minimum energy needed to free particles from the substrate surface. The material is removed by transfer of kinetic energy due to the collisions of plasma ions with substrate molecules. The disadvantage of this technique is that high ion energies have to be produced, which can cause damage to the mask and the substrate. The selectivity is low and the etch rate is poor.
2. *chemical etching* : The plasma forms species, which are selectively reacting with the surface particles. When the chemical process forms volatile products which can desorb from the surface, the substrate is etched. This process is highly selective, but isotropic.
3. *ion assisted etching* : The etch effect of the previous mechanism can be enhanced when the reactive species are bombarded with energetic ions. Figure 1.2. shows the effect of this synergy. An argon ion beam is used in combination with a reactive gas (XeF_2) to etch amorphous silicon. Due to the vertical ion bombardment, this etch process is anisotropic.
4. *reactive ion etching (RIE)* : Here, the reactive species are molecular ions which bombard the surface. The combination of their kinetic energy and selectivity results in an anisotropic etch process.

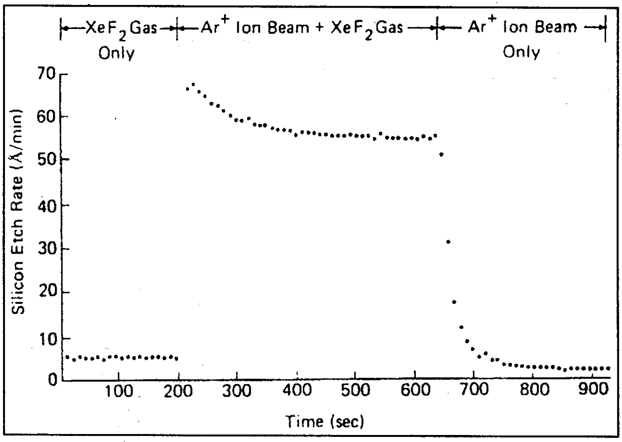

Figure 1.2 : Example of ion assisted etching, as measured by Coburn et al.[1]

The anisotropic effect is enhanced when the reaction products are covering the sidewalls of the structure. As a result, the etching stops. This effect is called "sidewall passivation". The directed ion beam removes only the layers at the bottom, resulting in steep walls[2].

A plasma etching application, which is well established nowadays, is the etching of silicon and silicon oxide with halo-carbons. When CF_4 is used as the main gas, it produces CF_3^+ by dissociative ionization in the plasma :

$$CF_4 + e \rightarrow CF_3^+ + F + 2e.$$

Also CF_2 and CF_3 are produced by electron-neutral dissociation. In these processes, F is formed in the plasma. The F atoms react selectively with the silicon at the substrate, creating the volatile SiF_4 :

$$Si(s) + 4F(g) \rightarrow SiF_4(g),$$

where (s) and (g) indicate the solid and gaseous phases of the products. The volatile SiF_4 is pumped away and the silicon is etched. For anisotropic etching, a high-energetic ion beam of CF_3^+ reaches the substrate. The effect of the bombardment can be that the ions remove the passivation layer at the bottom of the trench or that the reaction rate is increased. Silicon oxide is also etched by this process. By adding small amounts of hydrogen, the etch rate of Si decreases much faster compared to that of SiO_2. So hydrogen can be used to selectively etch silicon oxide over silicon. By adding amounts of oxygen, however, the etch rate of silicon is increased, while the etch rate of silicon oxide remains constant. This process can be used to selectively etch silicon over silicon oxide. The chemistry behind these processes is that the oxide reacts easily with C to form CO, leaving more F in the plasma to be used for etching of Si. Hydrogen however, reacts with F to form HF in the plasma. The decrease of free F results in an lower Si etch rate.

With ion enhanced etching, the anisotropy of the etch process is mainly determined by the velocity distribution of the ions reaching the surface. When the velocity component of the ions parallel to the surface is not small, the substrate will be underetched. The etch rate is determined by the ion energy and flux. In various etching applications a compromise must be made between high etch rate, surface damage and selectivity.

1.3. Sources for plasma etching

1.3.1. Capacitively coupled plasma (CCP) sources

The most commonly used plasma-etch reactor of today is the capacitively coupled RF discharge or RF diode. The reactor consists of two parallel electrodes, separated at a distance l, see figure 1.3. The most common RF frequency is 13.56 MHz, a frequency which does not interfere with radio and television broadcasting bands. Also higher and lower frequencies are used, like with the 450 kHz source described in chapter 5. The

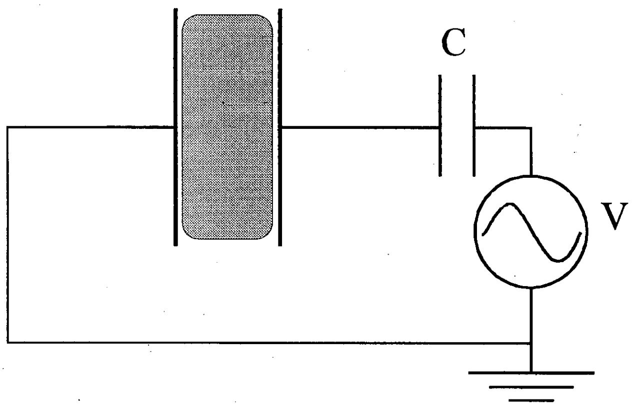

Figure 1.3 : Basic setup of a capacitively coupled plasma source.

gap between the electrodes is filled with the etch gas. When the gas is at a low pressure, typically in the order of 10 Pa, the sources are called reactive ion etchers (RIE's). This name is rather confusing, because the etch process can also be dominated by reactive neutrals, in combination with energetic ion bombardment. At 13.56 MHz, the ions are not able to follow the electromagnetic field, whereas the electrons are. Therefore, the electromagnetic energy will be mainly absorbed by the electrons, which can ionize the neutrals. The ions are much slower than the electron due to their mass. This results in a faster loss of negative charge to the walls. The resulting potential difference between the walls and the plasma creates an electric field region at the edge of the plasma. This region, the sheath, accelerates the ions and slows down the electrons, balancing the fluxes of positively and negatively charged particles to the walls. The ions, which now reach the substrate with a high energy, are responsible for the plasma etch process. The total ion energy is controlled by this effect, in combination with the potential of the wall itself, determined by the voltage over the electrodes. To produce more ions in the plasma, the electrode potential has to increase. Simultaneously the ion energy at the electrode surface increases, which can cause unwanted effects, like damage.

1.3.2. High density plasma (HDP) sources[3]

A major drawback of capacitively coupled plasma sources is that the ion flux to the substrate surface cannot be varied independently of the bombarding energy of the ions. When a high degree of anisotropy is desired, the pressure of the gas should be lowered to decrease the number of collisions in the ion acceleration region. For capacitively coupled plasma (CCP) sources this means that to achieve high etch rates, the voltage should increase. This will result in higher ion energies on the surface, causing damage and loss of selectivity. These limitations have led to the development of high density plasma (HDP) sources. Here, separate mechanisms are used to control the ion flux and the ion bombarding energy. The operational conditions and the resulting plasma parameters are shown in table 1.1. They are compared with the values for the capacitively coupled plasma sources.

Table 1.1 : Typical values for CCP and HDP sources.[4]

Parameter	Units	CCP source	HDP source
Pressure p	Pa	1 - 100	0.05 - 10
Applied power P	W	50 - 2000	100 - 5000
Frequency f	MHz	0.05 - 13.56	0 - 2450
Volume V	m^{-3}	10^{-3} - 10^{-2}	$2 \cdot 10^{-3}$ - $5 \cdot 10^{-2}$
Typical area A	m^2	$3 \cdot 10^{-2}$ - 0.2	$3 \cdot 10^{-2}$ - 0.1
Magnetic field B	kG	-	0 - 0.1
Plasma density n	m^{-3}	10^{15} - 10^{17}	10^{16} - 10^{18}
Electron temperature T_e	eV	1 - 5	2 - 7
Ion energy ε_i	eV	200 - 1000	20 - 500
Ionization degree α	-	10^{-6} - 10^{-3}	10^{-4} - 10^{-1}

In figure 1.4 some examples of high density sources are shown. A capacitively coupled RF bias source drives the electrode where the wafer is placed, to control the ion bombarding energy. All types use a non capacitive source to inject power in the system, resulting in a high ion density. Firstly, the electron cyclotron resonance (ECR) plasma reactor is shown. Here, one or more permanent magnets surround the plasma chamber to create a dc, axially varying magnetic field. Microwave power is injected into the plasma through a dielectric window. This heats the electrons, which can ionize the gas in the plasma chamber. The helicon source uses a dc magnetic field in combination with an RF driven antenna. The excited helicon wave interacts with the electrons in the chamber, resulting in a transfer of energy. The helical resonator consists of a resonating structure, creating a slow electromagnetic wave. The last source in figure 1.4 is the inductively coupled plasma (ICP) source. The cylindrical coil and the plasma together act as a transformer, where the latter is the secondary, single turn, conductor. The power is inductively coupled through a dielectric window without using external magnets. Present day research on high density sources focuses on the uniformity of the plasmas over a 200-300 mm wafer diameter. Disadvantages of these systems are the poor power efficiency through the dielectric window and the need for ultra high vacuum equipment to operate at low pressures.

A diagnostic study on an ICP source is presented in chapter 6.

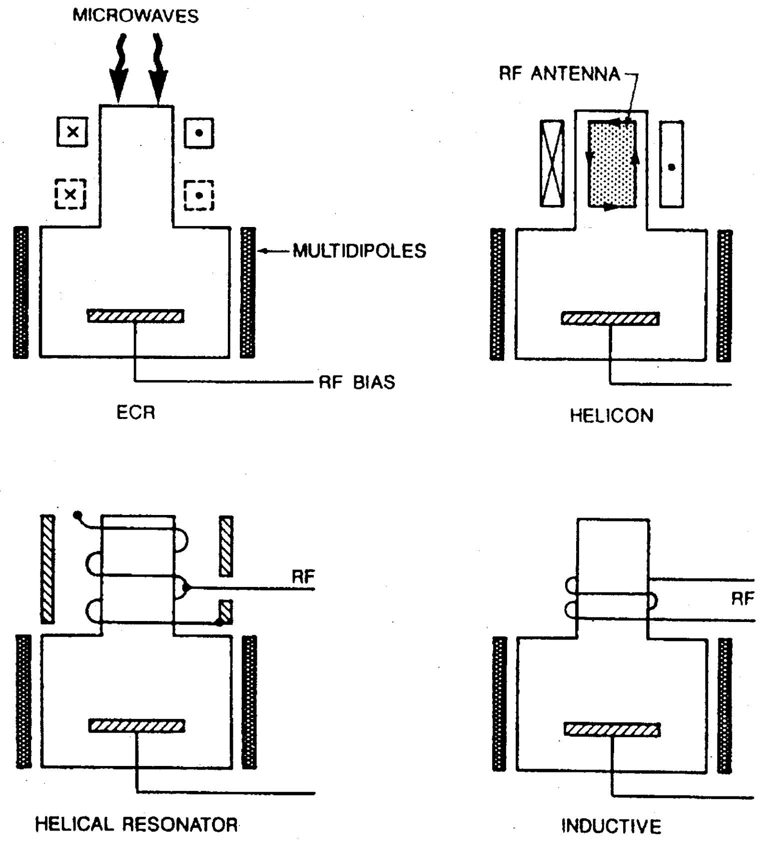

Figure 1.4 :Four examples of HDP sources.[3]

1.4. Scope of this thesis

This thesis focuses on etch plasmas. The measurements and models described here, give more insight in the processes in various types of plasma etch reactors. Studies on both of the above described systems are presented.

The first part of this thesis (chapters 2, 3, and 4) contains an introduction into the used theoretical and experimental techniques for the work described in the last chapters (5 and 6). Chapter 2 introduces various relevant plasma physical quantities and relations. A large part of this chapter is devoted to the theory of absorption. The influence of saturation on the linewidth is evaluated and applied to the Doppler shifted laser induced fluorescence (DSLIF) technique. Chapter 3 contains a review of the Bohm criterion and the presheath theory. The contents of this chapter are based on an article by Riemann[5]. An overview of the diagnostic tools, used in this work, is given in chapter 4. The setup and theoretical background of optical emission spectroscopy, IR-laser absorption spectroscopy, Langmuir probe, and the DSLIF measurement are presented. These techniques are all applied to the two plasma reactors described in the last two chapters.

In chapter 5 a capacitively coupled parallel plate reactor is introduced. A 21 Pa argon plasma is generated by a 450 kHz RF voltage. At this frequency, the ions can partially follow the electric field variations. This results in a time dependency in the energy distribution of the ions at the wafer surface. The energy of the ions is determined by the time in the RF period when the ions enter the sheath. With Doppler shifted laser induced fluorescence (DSLIF) the time resolved velocity distribution of the ions can be determined. Inside the sheath the density of ions is too low to be measured, but at the transition region between the sheath and the glow, the initial acceleration of the ions, at various moments inside the RF period, towards the electrode surface is measured. Additional measurements are used to determine several plasma parameters. With a double Langmuir probe and IR absorption spectroscopy the densities and temperatures of electrons and metastable atoms have been determined. With time resolved optical emission spectroscopy the excitation processes of several atomic and ionic energy levels are investigated. Some levels can be populated from metastable levels whereas others can not, giving rise to a different emission profile. The main time dependence is formed by the secondary electrons in the plasma. These are created at the electrode surface after ion bombardment and are accelerated in the electric field of the sheath. The results are compared with a 1D fluid model which includes this secondary electron effects.

In a high density inductively coupled plasma (ICP) reactor, which is operated at low pressures (0.2 - 10 Pa), the region before the sheath, the presheath, is much larger and extends to the middle of the plasma. The investigations carried out on this reactor are described in chapter 6. With DSLIF, the velocity distribution function of metastable ions in this region is determined. The velocity distribution function of the ions in the presheath determines the ion energy distribution at the wafer surface. It is therefore important to investigate the processes which influence this distribution function. Because the creation and loss mechanisms for the (measured) metastable ions and the ground state ions are different, it is necessary to investigate the relation between these two velocity distribution functions. For this purpose a Monte-Carlo model is developed, which takes excitation and ionization as well as elastic and charge exchange collisions with neutrals into account. The mean velocity of the ions at the transition between the presheath and the sheath has to obey the Bohm criterion. This criterion says that the velocity of ions entering the sheath must (on average) be larger than a critical value, the Bohm velocity. With DSLIF the acceleration of the ions in the presheath to the Bohm velocity is followed. Optical emission spectroscopy, IR laser absorption spectroscopy, and Langmuir probe measurements are used to obtain several plasma parameters, which are needed for the interpretations of the results.

References

[1] J.W. Coburn and H.F. Winters, J.Appl.Phys. **50** (1979), pp3189

[2] G.S. Oehrlein and Y.H. Lee, J.Vac.Sci.Technol. **A5** (1987), pp1585

[3] *Physics of Thin Films (vol. 18): Plasma sources for thin film deposition and etching*, edited by M.H. Fracombe and J.L. Vossen, Academic Press, ISBN 0-12-533018-9, pp1-119 : *Design of High-Density Plasma Sources for Materials Processing*, by M.A. Liebermann and R.A. Gottcho.

[4] *Principles of plasma discharges and materials processing*, M.A. Liebermann and A.J. Lichtenberg, J. Wiley & Sons, ISBN 0-471-00577-0

[5] K.-U. Riemann, J. Phys. D : Appl. Phys. **24** (1991), pp493

2. Aspects of radiation and plasma physics

In this chapter an overview is given of the relevant plasma physics and the various aspects of radiation theory. The latter is used to evaluate the theoretical background of the Doppler shifted laser induced fluorescence (DSLIF) technique.

2.1. Plasma physics

2.1.1. General

A plasma consists of neutrals, ions, and electrons. To classify the various plasma configurations, the ionization degree α_{iz} is often used :

$$\alpha_{iz} = \frac{N_i}{N_i + N_g}, \qquad 2.1$$

where N_i and N_g are the ion and neutral gas densities in the plasma. This quantity is unity for a fully ionized plasma and much smaller (in the order of 10^{-2} to 10^{-6}) for weakly ionized plasmas. The low pressure discharges treated in this thesis are all weakly ionized plasmas, which consist of only positive ions, electrons, and neutral atoms. These three categories of particles all have their own energy distribution, following the Boltzmann equation. Because the energy exchange between neutrals or ions and electrons is very inefficient due to the large mass ratio, the electrons have a much higher average energy than the ions and neutrals. At sufficiently high electron-electron collision frequencies, the velocities v_e of the electrons (with mass m_e) are distributed according to the Maxwell-Boltzmann distribution function with a characteristic temperature T_e :

$$f_v(v_e)\cdot \mathrm{d}v_e = \frac{4}{\sqrt{\pi}}\left(\frac{m_e}{2kT_e}\right)^{3/2} v_e^2 \exp\left[-\frac{m_e v_e^2}{2kT_e}\right]\cdot \mathrm{d}v_e . \qquad 2.2$$

According to the relation above, $N_e f_v(v_e)\mathrm{d}v_e$ represents the number of electrons having a velocity in the interval $[v_e,v_e+\mathrm{d}v_e]$. The average electron velocity is found by integration :

$$\langle v_e\rangle = \int_0^\infty v_e \cdot f_v(v_e)\mathrm{d}v_e = \sqrt{\frac{8kT_e}{\pi m_e}} . \qquad 2.3$$

The maximum of $f_v(v_e)$ is given by $\frac{1}{2}m_e v_e^2 = kT_e$.
The distribution function can also be expressed in terms of energy :

$$f_E(E_e)\cdot \mathrm{d}E_e = \frac{2}{\sqrt{\pi}}\left(\frac{1}{kT_e}\right)\sqrt{\frac{E_e}{kT_e}} \exp\left[-\frac{E_e}{kT_e}\right]\cdot \mathrm{d}E_e . \qquad 2.4$$

The maximum in the energy distribution function is found at $E_e = \frac{1}{2}kT_e$. The average energy is $3/2kT_e$. Typical electron temperatures in low pressure plasmas vary from 10^4 to 10^5 K. This corresponds to energies of 1 - 10 eV. These are much higher than the temperature of the neutrals (e.g. 300K ≈ 0.026 eV) or ions (e.g. 500K ≈ 0.04 eV). As an example, the Maxwell-Boltzmann distribution function of electrons with a temperature of 2 eV is plotted in figure 2.1.

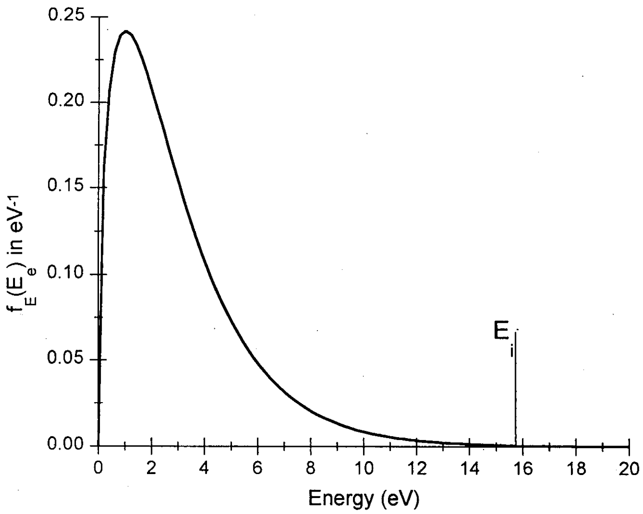

Figure 2.1 : Maxwell-Boltzmann distribution of 2 eV electrons. The ionization energy of argon is shown as a threshold.

The graph shows that e.g. argon neutrals (with ionization energy of 15.8 eV) can be ionized by a small number of electrons in the tail of the distribution.
The random flux Γ of particles in an arbitrary direction is given by:

$$\Gamma_{e,i} = \frac{1}{4} N_{e,i} \langle v_{e,i} \rangle, \qquad 2.5$$

with N the density and $\langle v \rangle$ the average velocity of the electrons (e) and ions (i). Since the average velocity of electrons is much larger than that of the ions, an electrically insulated object in the plasma will initially be bombarded with more electrons than ions. Therefore, the object will be charged negatively, until the resulting electric field is strong enough to balance the electron and ion fluxes. The region where electrons are repelled and ions are attracted, is called "the sheath". The theory behind this transition layer is treated in chapter 3. A sheath is present around every insulated object in contact with the plasma, like walls and probes. The equilibrium potential of the object is called the floating potential U_f. The definition of this potential is only meaningful if it is compared with the plasma potential U_{plasma}. When the object is at floating potential, the ion and electron flux balance. The electron flux is smaller than the thermal flux, due to the retarding field, while the ion flux is determined by the thermal flux at the edge of the sheath :

$$N_e \frac{\langle v_e \rangle}{4} \exp\left[-\frac{e\left(U_{plasma} - U_f\right)}{kT_e} \right] = N_i \frac{\langle v_i \rangle}{4}, \qquad 2.6$$

resulting in :

$$U_{plasma} - U_f = \frac{kT_e}{2e} \ln\left(\frac{m_i}{m_e} \frac{T_e}{T_i} \right). \qquad 2.7$$

This relation can be refined when the velocity at the edge of the sheath, the Bohm velocity (defined in chapter 3), is used instead of the thermal ion velocity. This alters equation 2.7 in :

$$U_{plasma} - U_f = \frac{kT_e}{2e} \ln\left(\frac{m_i}{2\pi m_e} \right). \qquad 2.8$$

For argon, this results in $U_{\text{plasma}} - U_f = 4.7\ kT_e/e$.

To investigate the influence of a small charged object (e.g. an ion) in a homogeneous plasma, the one-dimensional Poisson equation :

$$\frac{d^2\phi}{dz^2} = -\frac{e(N_i - N_e)}{\varepsilon_0} \qquad 2.9$$

is used to calculate the space dependence of the potential $\phi(z)$. According to Boltzmann, the electron density is given by :

$$N_e(z) = N_e^o \exp\left[-\frac{e\phi(z)}{kT_e} \right] \qquad 2.10$$

and the ion density is supposed to be constant :

$$N_i(z) = N_i^0, \qquad 2.11$$

where $N_i^0 = N_e^0 = N_0$ are the ion and electron densities in the plasma. Substituting this in the Poisson equation and assuming only small potential variations ($e\phi(z) \ll kT_e$) :

$$\frac{d^2\phi(z)}{dz^2} = \frac{eN_0}{\varepsilon_o} \frac{e\phi(z)}{kT_e}. \qquad 2.12$$

This has an exponentially decaying solution :

$$\phi(z) = \phi_o \exp\left[-\frac{z}{\lambda} \right], \qquad 2.13$$

where

$$\lambda = \sqrt{\frac{\varepsilon_0 k T_e}{e^2 N_0}} \equiv \lambda_D , \qquad 2.14$$

with λ_D the Debye length. This length parameter is the typical distance over which small potential variations stretch out over the plasma. Because the exponential decay is much stronger than the Coulomb interaction ($\sim r^{-1}$), this effect is called "Debye shielding". For length scales $l \gg \lambda_D$, the plasma is quasineutral.

When a disturbance in the plasma causes a displacement ξ of the electrons, the net space charge on the edges is $eN_e\xi$. The resulting electric field is given by :

$$E = \frac{eN_e\xi}{\varepsilon_0} . \qquad 2.15$$

The reaction of the electrons is :

$$m_e \frac{\mathrm{d}^2\xi}{\mathrm{d}t^2} = -eE , \qquad 2.16$$

or

$$\frac{\mathrm{d}^2\xi}{\mathrm{d}t^2} = -\omega_{pe}^2 \xi . \qquad 2.17$$

This corresponds to an oscillatory motion with angular frequency ω_{pe} given by :

$$\omega_{pe} = \sqrt{\frac{e^2 N_e}{\varepsilon_0 m_e}} , \qquad 2.18$$

which is called the electron plasma frequency. When the non-infinite ion mass m_i is taken into account, the oscillation frequency changes to :

$$\omega = \sqrt{\omega_{pe}^2 + \omega_{pi}^2} , \qquad 2.19$$

with

$$\omega_{pi} = \sqrt{\frac{e^2 N_e}{\varepsilon_0 m_i}} , \qquad 2.20$$

the ion plasma frequency. In a low pressure argon plasma, with typical ion densities of 10^{16} m^{-3}, the electron and ion plasma frequencies are 898 MHz and 3.31 MHz, respectively. This shows that the electrons can easily follow the typical electric field of 13.56 MHz, whereas the ions cannot.

For charged particles in a plasma, the momentum balance can be evaluated to yield :

$$\Gamma = N\mathbf{v} = \pm\mu N\mathbf{E} - D\nabla N , \qquad 2.21$$

with the plus or minus sign depending on the charge of the particle. The mobility,

$$\mu = \frac{|q|}{m \nu_m} , \qquad 2.22$$

depends on the electric charge q and the momentum transfer collision frequency ν_m (see section 2.1.2). The diffusion coefficient D can be related to the particle temperature through the Einstein relation :

$$\frac{D}{\mu} = \frac{kT}{e} . \tag{2.23}$$

In a stationary plasma, besides the densities, also the fluxes of ions and electrons must be equal. Evaluating equation 2.21 results in :

$$\Gamma = -\frac{\mu_e D_i + \mu_i D_e}{\mu_i + \mu_e} \nabla N = -D_a \nabla N , \tag{2.24}$$

with D_a the ambipolar diffusion coefficient. In the plasmas treated here, $\mu_e \gg \mu_i$, so using equations 2.22 and 2.23 :

$$D_a \approx D_i \left(1 + \frac{T_e}{T_i}\right) \approx \mu_i \frac{kT_e}{e} . \tag{2.25}$$

This indicates that the ambipolar diffusion coefficient is in first approximation determined by the mobility of the ions and the temperature of the electrons. In situations where the ambipolar diffusion coefficient is constant, the particle density decays exponentially with a time constant τ. The ambipolar diffusion coefficient and the decay constant are then related through the diffusion length Λ as :

$$D_a = \frac{\Lambda^2}{\tau} . \tag{2.26}$$

2.1.2. Collisions

When two or more particles interact, their internal energy can be unchanged. In this case, the collision is elastic. The kinetic energy of the particles is exchanged, but the total kinetic energy is conserved. When the initial state of the particles changes during a collision, the process is inelastic. Examples of these processes are excitation and ionization.

When a beam of particles with velocity v and density N collides with a group of particles in rest with density N_g, only a fraction of the incoming particles will collide. The initial flux $\Gamma = Nv$ changes with $\mathrm{d}\Gamma$ over a distance $\mathrm{d}x$ according to :

$$\mathrm{d}\Gamma = -\sigma(v)\Gamma N_g \mathrm{d}x . \tag{2.27}$$

The proportionality constant σ is the cross-section, which is determined by the collision process. When σ is uniform, equation 2.27 can be solved :

$$\Gamma = \Gamma_0 \exp\left[-\frac{x}{\lambda_m}\right], \tag{2.28}$$

where the mean free path λ_m is given by :

$$\lambda_m = \frac{1}{N_g \sigma} . \tag{2.29}$$

Often the mean time between collisions τ is used :

$$\tau = \frac{\lambda_m}{v}, \tag{2.30}$$

or the inverse :

$$\nu = \frac{1}{\tau} = N_g \sigma v, \tag{2.31}$$

which is the collision frequency.
When this coefficient is expressed per unit of density, the rate constant K is obtained :

$$K = \sigma v. \tag{2.32}$$

Often, the cross-section is a function of velocity. Then equation 2.32 must be replaced with the integration over the velocity distribution $f(v)$:

$$K = \int \sigma(v) v f(v) \mathrm{d}v. \tag{2.33}$$

In general, the cross-section depends on the scattering angle θ. Therefore, the differential scattering cross-section $I(v,\theta)$ should be used. The total scattering cross-section, σ_{sc}, is then defined as :

$$\sigma_{sc} = 2\pi \int_0^\pi I(v,\theta) \sin\theta \mathrm{d}\theta. \tag{2.34}$$

The cross-section σ_{m} for momentum transfer includes the fractional loss of the initial momentum, which depends on the scattering angle :

$$\sigma_m = 2\pi \int_0^\pi (1-\cos\theta) I(v,\theta) \sin\theta \mathrm{d}\theta. \tag{2.35}$$

For elastic, hard-sphere collisions the cross-sections for scattering and momentum transfer are equal.
For elastic collisions, the energy fraction which is transferred can be written as :

$$\varsigma_L = \frac{2m_1 m_2}{\left(m_1 + m_2\right)^2}(1-\cos\theta), \tag{2.36}$$

with m_1 and m_2 the masses of the colliding particles.
For coulomb interactions, the interaction potential is :

$$U(r) = \frac{q_1 q_2}{4\pi\varepsilon_0 r}, \tag{2.37}$$

with q_1 and q_2 the charges of the two particles separated at distance r. The corresponding differential scattering cross-section can be determined to be :

$$I = \left(\frac{b_0}{2\sin^2\left(\theta/2\right)}\right)^2, \tag{2.38}$$

where b_0 the classical distance of closest approach is defined as :

$$W_R = \frac{q_1 q_2}{4\pi\varepsilon_0 b_0}, \qquad 2.39$$

with W_R the kinetic energy of the center of mass system, determined by the initial velocities. For a scattering angle of $\pi/2$ the differential cross-section is b_0^2. It can be seen from equation 2.38 that the cross-section is large for forward scattering. When the change in momentum is incorporated (equation 2.35), the momentum transfer cross-section for Coulomb interaction can be evaluated to be :

$$\sigma_m = 4\pi b_0^2 \ln\left(\frac{\lambda_D}{b_0}\right) = 4\pi b_0^2 \ln \Lambda_c, \qquad 2.40$$

with the use of the Debye length λ_D, which determines the distance for the charged particle interaction.

2.2. *Principles of radiation*[1,2]

2.2.1. The classical atom model

In the classical model, the atom is considered as a nucleus of mass m and charge $+Ze$, surrounded by Z electrons of mass m_e and charge $-e$, moving in orbits around it. When the atom is excited, an electron moves from its equilibrium position. As a result, the electron performs a simple harmonic oscillation around the nucleus with a characteristic angular frequency ω. This frequency corresponds to the wavelength of the emitted radiation as :

$$\lambda_i = 2\pi \frac{c}{\omega}. \qquad 2.41$$

The simple harmonic oscillator can be described in terms of the dipole moment :

$$\mathbf{p}(t) = \mathbf{p}\exp(-i\omega t), \qquad 2.42$$

with

$$\mathbf{p} = -ed\hat{\mathbf{e}}_r. \qquad 2.43$$

$d\hat{\mathbf{e}}_r$ is the space vector between the nucleus with the other electrons at rest in the origin and the electron which performs the oscillation. At large distances $r \gg d$, the electric and magnetic field of this dipole at position $P(r,\theta,\varphi)$ are given by :

$$\mathbf{E} = \frac{k^2}{4\pi\varepsilon_0} \cdot \left(\hat{\mathbf{e}}_r \times \mathbf{p}\right) \times \hat{\mathbf{e}}_r \cdot \frac{\exp\left(i(kr - \omega t)\right)}{r} \qquad 2.44$$

$$\mathbf{H} = \varepsilon_0 c \cdot \frac{k^2}{4\pi\varepsilon_0} \cdot \left(\hat{\mathbf{e}}_r \times \mathbf{p}\right) \cdot \frac{\exp\left(i(kr - \omega t)\right)}{r}, \qquad 2.45$$

with

$$k = \frac{\omega}{c}. \qquad 2.46$$

The time averaged radiative energy loss per unit area is calculated by evaluating the Poynting vector :

$$\mathbf{S} = \frac{1}{2}\mathrm{Re}\left[\mathbf{E} \times \mathbf{H}^*\right]. \tag{2.47}$$

According to the Poynting theorem, integrating **S** over the whole area of a sphere of radius r gives the time averaged flux of energy through the sphere. Using equations 2.44, 2.45 and 2.47 the energy loss per unit time is :

$$\frac{\mathrm{d}W}{\mathrm{d}t} = \frac{k^4 c}{12\pi\varepsilon_0}|\mathbf{p}|^2. \tag{2.48}$$

The total energy of an oscillating dipole is :

$$W = \frac{m_e \omega^2 d^2}{2}. \tag{2.49}$$

The time-averaged fractional energy loss over one period is :

$$\frac{1}{W}\left(\frac{2\pi}{\omega}\frac{\mathrm{d}W}{\mathrm{d}t}\right) = \frac{e^2\omega}{3\varepsilon_0 m_e c^3}. \tag{2.50}$$

So, the differential equation for the energy function is:

$$-\frac{\mathrm{d}W}{\mathrm{d}t} = \frac{e^2\omega^2}{6\pi\varepsilon_0 m_e c^3}W, \tag{2.51}$$

which results in an exponential decay function

$$W(t) = W_0 \exp\left[-\frac{t}{\tau_{cl}}\right], \tag{2.52}$$

with the classical lifetime of the atom given by :

$$\tau_{cl} = \frac{6\pi\varepsilon_0 m_e c^3}{e^2\omega^2} = \frac{3\varepsilon_0 m_e c\lambda^2}{2\pi e^2}. \tag{2.53}$$

This theory is only valid for calculations of the lifetimes of excited atom levels which can decay directly to the ground state. In general the lifetime τ of an excited level k is determined by the sum of all transition probabilities A_{ki} to lower states i :

$$\tau_k = \frac{1}{\sum_i A_{ki}}. \tag{2.54}$$

2.3. *The shape of spectral lines*

2.3.1. Natural line width

In the previous section, the radiation from the oscillating atom was considered monochromatic. In real life, every spectral line has a certain width. By using the classical atomic model it can be shown that every spectral line has a natural or radiative lineshape. By introducing a radiation reaction force F_r the loss of energy emitted as radiation has to be equal to the work done by this force during one cycle of the electron. This can be evaluated to yield[3] :

$$F_r = m_e \gamma \dot{z}\,, \tag{2.55}$$

where γ is the damping constant. The solution of the equation of motion has for $\gamma \ll \omega_0$ the form of a damped oscillation :

$$z = z_0 \cdot \exp\left[-\gamma \frac{t}{2}\right] \cdot \exp\left[-i\omega_0 t\right]. \tag{2.56}$$

The electric field caused by this moving electron is then :

$$E(t) = E(0) \cdot \exp\left[-i(\omega_0 - i\gamma/2)t\right] \tag{2.57}$$

for $t \geq 0$. The intensity of the field, $I \propto E^2$, decreases to 1/e of its initial value after the decay time $\tau = 1/\gamma$. The wave of equation 2.57 is not infinitely long, so it has lost its monochromatic character. Its frequency distribution can be calculated by taking the Fourier transform:

$$\begin{aligned} E(\omega) &= \left[\frac{1}{2\pi}\right]^{1/2} \cdot \int_0^\infty E(t) \cdot \exp[i\omega t]\mathrm{d}t \\ &= -\frac{1}{\sqrt{2\pi}} \cdot \frac{E(0)}{i\left\{(\omega - \omega_0) + i\gamma/2\right\}}\,, \end{aligned} \tag{2.58}$$

or in terms of the intensity $I(\omega)$, which is proportional to $|E(\omega)|^2$:

$$\begin{aligned} I(\omega) &= I_0 \cdot \frac{\gamma/2\pi}{(\omega - \omega_0)^2 + \gamma^2/4}\,, \\ &= I_0 \cdot L(\omega - \omega_0, \gamma) \end{aligned} \tag{2.59}$$

with

$$I_0 = \int_0^\infty I(\omega)\mathrm{d}\omega\,. \tag{2.60}$$

The lineshape function L in equation 2.59 is the normalized Lorentz function. The frequency dependence for absorption and emission are generally shaped according to this profile. The full width at half maximum (FWHM) is :

$$\Delta\omega_{1/2} = \gamma = \frac{1}{\tau} \quad \text{or} \quad \Delta\nu_{1/2} = \frac{\gamma}{2\pi} = \frac{1}{2\pi\tau}\,, \tag{2.61}$$

with τ the lifetime of the level. In the case of the transition used in this thesis (argon ion: $4p'^2F_{7/2} \rightarrow 4s'^2D_{5/2}$: $\lambda = 460.956$ nm) the lifetime of the upper level is 8.5 ns (see Appendix A). Hence, the classical approximation yields $\Delta\omega_{1/2}$= 117 MHz and $\Delta\nu_{1/2}$=

18.7 MHz. The maximum of the Lorentz distribution is $I(\omega_0) = 2/(\gamma\pi)$, or when expressed in ν: $I(\nu_0) = 4/\gamma$.

2.3.2. Pressure broadening

Due to the interaction of an atom with its neighbors, the energy levels will change when the two particle approach. This leads to a variation in the frequency of the emitted light, resulting in a broadening of the line. This broadening is a function of pressure. Therefore it is called pressure broadening. The resulting lineshape will be a Lorentz profile with a full width at half maximum (FWHM) of[4] :

$$\Delta\omega_{1/2} = \gamma + 2N\sigma v , \qquad 2.62$$

with N the density of atoms, σ the cross-section and v the average velocity. For 10 Pa, 300 K argon gas, and a cross-section of 100 Å^2, the second term of equation 2.62 yields 1 MHz, which is much smaller than the natural line width.

2.3.3. Transit time broadening

The linewidth of a transition can also be broadened by the limited residence time T of the particles inside a reaction region, e.g. a laser beam. This means that equation 2.58 should be integrated from 0 to T instead of to infinity. The resulting lineshape has a FWHM of[4] :

$$\Delta\omega_T = \frac{5.6}{T} . \qquad 2.63$$

The time T is defined as :

$$T = \frac{v}{d} , \qquad 2.64$$

with v the velocity component perpendicular to the laser beam direction and d is the width of the beam. If the laserbeam is Gaussian, the FWHM of the transit time broadened line is given by :

$$\Delta\omega_{tt} = \frac{4.8v}{w} , \qquad 2.65$$

where w is the width of the beam where the laser field is 1/e of its central value. The shape of the spectral intensity distribution of the last case is again Gaussian. For the interaction of an argon gas of 300 K with a 1 mm diameter laserbeam, the transit time broadening is according to equation 2.65 approximately 2 MHz.

2.3.4. Doppler broadening

Because the atoms have a certain thermal velocity, the emitted light is Doppler broadened. If an atom is moving towards an observer with velocity **v** much smaller than the speed of light c, the observer "sees" an emitted light wave of frequency ω_0 as

$$\omega = \omega_0 - \mathbf{v} \cdot \mathbf{k} , \qquad 2.66$$

where **k** is the incident wave vector of the light traveling from the atom to the observer. If the z-axis is chosen in the direction of **k**, the distribution function $P(v_z)\mathrm{d}v_z$ of velocity components v_z of a group of atoms is described by Maxwell as :

$$P(v_z)\mathrm{d}v_z = \sqrt{\frac{M}{2\pi kT}} \cdot \exp\left[-\frac{Mv_z^2}{2kT}\right]\mathrm{d}v_z, \qquad 2.67$$

where M is the mass of the particles and T is the temperature. Combining equation 2.66 with equation 2.67 results in a frequency distribution function $P(\omega)\mathrm{d}\omega$ which is measured by the observer :

$$\begin{aligned} P(\omega)\mathrm{d}\omega &= \frac{2}{\Delta\pi^{1/2}} \cdot \exp\left[-4\frac{(\omega-\omega_0)^2}{\Delta^2}\right]\mathrm{d}\omega, \\ &= G_\Delta(\omega-\omega_0)\cdot\mathrm{d}\omega \end{aligned} \qquad 2.68$$

where

$$\Delta = 2\left(\frac{\omega_0}{c}\right)\sqrt{\frac{2kT}{M}} \qquad 2.69$$

and G is the normalized Gaussian distribution function, with a full width at half maximum of :

$$\Delta\omega_{1/2} = \Delta\cdot\sqrt{\ln 2} = 2\left(\frac{\omega_0}{c}\right)\cdot\sqrt{\frac{2kT}{M}\ln 2}. \qquad 2.70$$

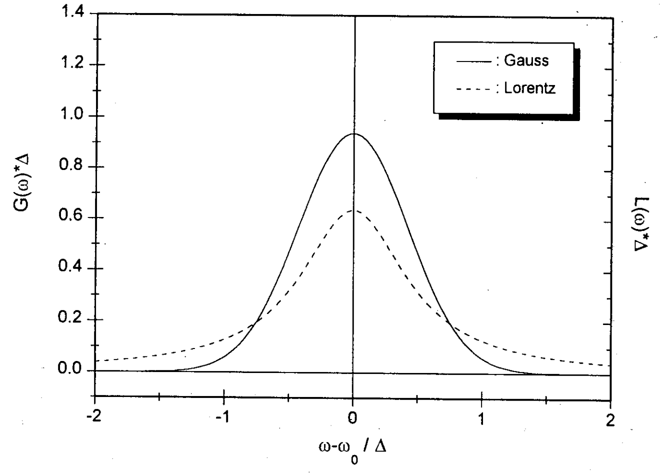

Figure 2.2 : Normalized Lorentz and Gauss distribution functions.

As an example, the Doppler width of the 611 nm line in 300 K argon is 1 GHz.
In figure 2.2 the normalized Gauss and Lorentz functions are compared. The areas under both curves are unity.

2.3.5. Voigt profile

Up to now, only separate broadening mechanisms are described, but in general combinations of effects are present. A particle which is emitting radiation with frequencies near ω_0, with a FWHM of Γ due to collisions and/or the radiative life time, is described by the Lorentz profile, $L_\Gamma(\omega - \omega_0)$. An observer is detecting radiation from a group of these particles, all moving with thermal velocities components v_z, in his direction, according to the Maxwell distribution (equation 2.68). He observes an intensity profile around ω_0 given by the convolution of the Lorentz and the Doppler profile:

$$V(\omega-\omega_0, {}^{\Gamma}\!/\!_{\Delta}) = \int_0^\infty L_\Gamma\left(\omega-\omega_0\left(1+v_z/c\right)\right)\cdot G_\Delta\left(v_z\right)\mathrm{d}v_z \ . \qquad 2.71$$

This profile, which can not be expressed analytically, is called a Voigt profile. If $\Delta \gg \Gamma$, the Voigt profile evolves to a Gauss profile and vice versa.

2.4. *Electronic transitions by radiation*

2.4.1. Absorption and stimulated emission : Einstein coefficients

The classical atom model is based on a solution of the interaction of an electron with an electric field $\mathbf{E}(t)$:

$$\ddot{\mathbf{r}} + \gamma\dot{\mathbf{r}} + \omega_0^2\mathbf{r} = -\frac{e}{m}\mathbf{E}(t)\,, \qquad 2.72$$

where $\mathbf{r}$ is the position vector of the electron relative to the atom. For the real atom, a different approach is used. All atoms have energy levels E_i, E_j, E_k, .. with statistical weights g_i, g_j, g_k, .. In equilibrium at temperature T, all electrons will be distributed over the levels according to Boltzmann :

$$N_i = \frac{N g_i \exp\left[-{}^{E_i}\!/\!_{kT}\right]}{\sum\limits_i g_i \exp\left[-{}^{E_i}\!/\!_{kT}\right]}\,, \qquad 2.73$$

with N_i the population density of the level i and N is the total atom density of all levels. The transition between two levels i and k ($E_k > E_i$) is investigated in an irradiated volume[3]. The energy density of the light is considered constant over frequency close to the transition frequency ω_{ki}.

- Absorption of a photon $\hbar\omega_{ki}$ results in an upward transition *i*→*k*. The transition probability P_{ik} is proportional to the energy density of radiation per unit frequency, $\rho(\omega)$ [$Jm^{-3}s$]. The proportionality constant is named $B_{ik}^{\rho(\omega)}$, the Einstein coefficient for absorption. The upward rate for the transition is given by :

$$\frac{dN_i}{dt} = -N_i P_{ik} = -N_i B_{ik}^{\rho(\omega)} \cdot \rho(\omega_{ki}). \qquad 2.74$$

- Stimulated emission with a photon $\hbar\omega_{ki}$ results in an downward transition (*k*→*i*). The transition probability P_{ki} is proportional to the energy density of radiation per unit bandwidth, $\rho(\omega)$. The proportionality constant is named $B_{ki}^{\rho(\omega)}$, the Einstein coefficient for stimulated emission. The downward rate for the transitions are formed by spontaneous decay and stimulated emission :

$$\frac{dN_k}{dt} = -N_k P_{ki} = -N_k\left\{A_{ki} + B_{ki}^{\rho(\omega)} \cdot \rho(\omega_{ki})\right\}. \qquad 2.75$$

The spontaneous decay coefficient A_{ki} is equal to the damping coefficient γ, used in the previous section. In thermal equilibrium, the two rates of equations 2.74 and 2.75 have to be the same. Hence :

$$\frac{N_k}{N_i} = \frac{B_{ik}^{\rho(\omega)} \cdot \rho(\omega_{ki})}{A_{ki} + B_{ki}^{\rho(\omega)} \cdot \rho(\omega_{ki})}. \qquad 2.76$$

But, the Boltzmann equation is also valid for this rate, so :

$$\frac{N_k}{N_i} = \frac{g_k}{g_i} \cdot \exp\left[-\frac{\hbar\omega_{ki}}{kT}\right]. \qquad 2.77$$

This has to be valid for all temperatures *T*. Evaluation leads to :

$$\rho(\omega_{ki}) = \frac{g_k A_{ki} \exp\left[-\frac{\hbar\omega_{ki}}{kT}\right]}{g_i B_{ik}^{\rho(\omega)} - g_k B_{ki}^{\rho(\omega)} \exp\left[-\frac{\hbar\omega_{ki}}{kT}\right]}, \qquad 2.78$$

for the energy density of radiation per unit bandwidth. According to Planck's black body radiation theory, the energy density is :

$$\rho(\omega) = \frac{\hbar\omega^3}{\pi^2 c^3} \cdot \frac{1}{\exp\left[\frac{\hbar\omega}{kT}\right] - 1}. \qquad 2.79$$

This leads to the conclusion that :

$$g_i B_{ik}^{\rho(\omega)} = g_k B_{ki}^{\rho(\omega)} \qquad 2.80$$

and

$$B_{ki}^{\rho(\omega)}=\frac{\pi^2c^3}{\hbar\omega_{ki}^3}A_{ki}\,. \qquad 2.81$$

These equations are often used in calculations on atomic systems interacting with light. To consider more general cases, the interaction between the two level system and a monochromatic light source is evaluated. Because the absorption lines all have a certain absorption profile $g(\omega)$, the induced rates should be proportional to this profile. When the energy density of the monochromatic source (of frequency ω) is ρ_ω, the induced transition rate changes to :

$$P_{ik}=\frac{\pi^2c^3A_{ki}}{\hbar\omega^3}\rho_\omega g(\omega) \qquad 2.82$$

In general, when the light is distributed according to $\rho(\omega)$, the induced transition rate is :

$$P_{ik}=\frac{\pi^2c^3A_{ki}}{\hbar}\int_0^\infty\frac{\rho(\omega)g(\omega)}{\omega^3}\mathrm{d}\omega \qquad 2.83$$

When $\rho(\omega)$ changes much slower than $g(\omega)$, the integral can be approximated to yield :

$$P_{ik}=\frac{\pi^2c^3A_{ki}}{\hbar\omega_{ki}^3}\rho(\omega_{ki})=B_{ki}^{\rho(\omega)}\rho\left(\omega_{ki}\right) \qquad 2.84$$

Which is the known definition of the Einstein coefficient.

Quantum mechanical calculations show that the relations above are also valid for system with more than two levels.

The so-called Einstein coefficients for absorption and stimulated emission appear in various forms, depending on the definitions used. When the intensity per unit bandwidth,

$$I(\omega)=c\rho\left(\omega\right), \qquad 2.85$$

is used instead of the energy density per unit bandwidth, the B-coefficient changes to

$$B_{ki}^{I(\omega)}=\frac{\pi^2c^2}{\hbar\omega_{ki}^3}A_{ki}\,, \qquad 2.86$$

so

$$B_{ik}^{I(\omega)}=\frac{1}{c}\cdot B_{ik}^{\rho(\omega)} \qquad 2.87$$

for a medium with a refractive index of 1.When frequencies are used instead of angular frequencies, the Einstein coefficients change to $B_{ik}^{I(\upsilon)}$ and $B_{ik}^{\rho(\upsilon)}$, which differ by factor of 2π :

$$B_{ki}^{I(\nu)} = \frac{B_{ki}^{I(\omega)}}{2\pi} = \frac{\lambda^3}{8\pi hc} A_{ki}$$
$$B_{ki}^{\rho(\nu)} = \frac{B_{ki}^{\rho(\omega)}}{2\pi} = \frac{\lambda^3}{8\pi h} A_{ki} \tag{2.88}$$

In spectroscopy, the oscillator strength f_{ki} is a commonly used quantity. Due to its historic background, it is defined as :

$$f_{ki} = \frac{A_{ki}}{3\gamma_{cl}} = A_{ki} \frac{\varepsilon_0 m_e c \lambda^2}{2\pi e^2}, \tag{2.89}$$

with γ_{cl} the reciprocal of the classical lifetime in equation 2.53. The oscillator strength for emission f_{ki} and for absorption f_{ik} are related in the same way as the Einstein coefficients :

$$g_k f_{ki} = g_i f_{ik} . \tag{2.90}$$

For practical use equation 2.89 can be evaluated to :

$$f_{ki} = 1.4992 \cdot 10^4 \lambda^2 A_{ki} . \tag{2.91}$$

2.4.2. Absorption

When a beam of light is guided through a volume of particles, the light can be absorbed. If the frequency of the light ω_{ki} is around a transition from level i to level k, the theory of the previous paragraph can be used to determine the absorption characteristics. The decrease of the intensity of the beam over a small distance dx can be written as the product of the photon energy and the number of particles in the volume that make a transition per unit of time :

$$\mathrm{d}I(x,\nu) = -h\nu\left(N_i(x) B_{ik}^{I(\nu)} - N_k(x) B_{ki}^{I(\nu)}\right) I(x) g(\nu) \mathrm{d}x , \tag{2.92}$$

or

$$\frac{\mathrm{d}I(x,\nu)}{\mathrm{d}x} = -h\nu N_i(x) B_{ik}\left(1 - \frac{N_k(x)}{N_i(x)} \frac{g_i}{g_k}\right) I(x) g(\nu) , \tag{2.93}$$

with $g(\nu)$ the spectral absorption profile and $I(x)$ the spatial profile of the intensity. It is assumed that the spectral intensity distribution is very narrow, as compared to the absorption profile. The equations above also assume that stimulated emission and absorption are dominant over the natural decay. Because in most systems $N_k/g_k \ll N_i/g_i$, due to the Boltzmann factor, equation 2.93 can be simplified to :

$$\frac{\mathrm{d}I(x,\nu)}{\mathrm{d}x} = -h\nu N_i(x) B_{ik}^{I(\nu)} I(x) g(\nu) . \tag{2.94}$$

Often the absorption coefficient $\kappa(x,\nu)$ is defined :

$$\mathrm{d}I(x,\nu) = -\kappa(x,\nu) I(x) \mathrm{d}x . \tag{2.95}$$

Evaluating equation 2.94, the absorption coefficient can be written as :

$$\begin{aligned}\kappa(x,\nu) &= h\nu N_i(x) B_{ik}^{I(\nu)} g(\nu) \\ &= \frac{\lambda^2}{8\pi} N_i(x) \frac{g_k}{g_i} A_{ki} g(\nu)\,, \\ &= \frac{e^2}{2\varepsilon_0 m_e c} f_{ki} N_i(x) g(\nu)\end{aligned} \qquad 2.96$$

with the use of equations 2.88-2.90.

For the absorption over a distance *l* equation 2.95 leads to :

$$\begin{aligned}\ln\left(\frac{I(0,\nu)}{I(l,\nu)}\right) &= \int_0^l \kappa(x,\nu)\mathrm{d}x \\ &= \frac{e^2}{4\varepsilon_0 m_e c} f_{ik}\, l \langle N_i \rangle g(\nu)\end{aligned}\,, \qquad 2.97$$

with $<N_i>$ the density of level *i*, averaged over the distance *l*.

2.4.3. A two level system[4]

2.4.3.1. Homogeneously-broadened transitions : saturation

When a two level system is considered with level *i* and level *k* ($E_k > E_i$), in a volume of monochromatic light (e.g. a laser), the rates of population of levels *k* and *i* are given by :

$$\frac{dN_k}{dt} = C_k - \frac{N_k}{\tau_k} - \left(N_k B_{ki}^{I(\nu)} - N_i B_{ik}^{I(\nu)}\right) \cdot I^\nu g(\nu) \qquad 2.98$$

$$\frac{\mathrm{d}N_i}{\mathrm{d}t} = C_i - \frac{N_i}{\tau_i} + \left(N_k B_{ki}^{I(\nu)} - N_i B_{ik}^{I(\nu)}\right) \cdot I^\nu g(\nu) \qquad 2.99$$

where C_k and C_i are the source terms for population of levels *k* and *i*, defined as :

$$C_x = \sum_l A_{lx} + D_x\,, \qquad 2.100$$

where the summation is over all levels *l* higher than level *x*. D_x is the source term including diffusion and collisional transfer. τ_k and τ_i are the effective lifetimes of the levels, see figure 2.3. These are defined as :

$$\frac{1}{\tau_x} = \sum_l A_{xl}\,, \qquad 2.101$$

where the summation is over all levels *l* lower than level *x*. Also A_{ki} is included in τ_k. I^ν is the total intensity of the light of frequency ν and $g(\nu)$ is the absorption profile for the transition, which in general is Lorentzian. This means that $B_{ik}^{I(\nu)} I^\nu g(\nu)$ is the

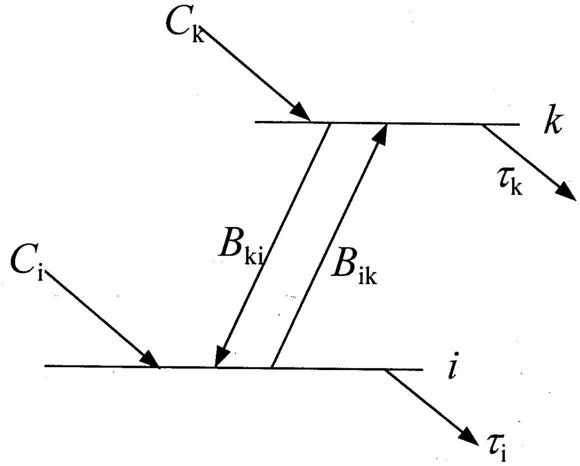

Figure 2.3 : The 2 level diagram.

absorption probability for this frequency. Analogous to equation 2.82, it is assumed that the spectral width of I^ν is much smaller than the width of $g(\nu)$. If not, equation 2.83 should be used instead. From the steady-state solution of equations 2.98 and 2.99 the inversion density is obtained :

$$\frac{N_k}{g_k}-\frac{N_i}{g_i}=\left(\frac{N_k^0}{g_k}-\frac{N_i^0}{g_i}\right)\cdot\left[1+S(\nu)\right]^{-1}. \qquad 2.102$$

The saturation parameter $S(\nu)$ is defined as :

$$S(\nu)=\tau^* g_k B_{ki}^{I(\nu)} I^\nu g(\nu)=\tau^* g_k A_{ki}\frac{\lambda^3}{8\pi hc} I^\nu g(\nu), \qquad 2.103$$

with

$$\tau^*=\frac{\tau_i}{g_i}+\frac{\tau_k}{g_k}, \qquad 2.104$$

the effective lifetime of the system.

The "no light ($I^\nu = 0$)" inversion density is given by :

$$\frac{N_k^0}{g_k}-\frac{N_i^0}{g_i}=\frac{C_k\tau_k}{g_k}-\frac{C_i\tau_i}{g_i}. \qquad 2.105$$

A major role in the equations is played by the saturation parameter $S(\nu)$. For high values of $S(\nu)$, the levels are totally coupled and the densities per statistical weight of the levels are equal. This effect is called saturation.

For Lorentzian shaped absorption profiles, saturation results in an absorption function with a full width at half maximum of :

$$\Delta\omega_{1/2} = \Gamma_k \left\{1 + S(v_0)\right\}^{1/2}, \qquad 2.106$$

with Γ_k the inverse of the lifetime of level k. Hence, the absorption line is broadened.

2.4.3.2.Inhomogeneously-broadened transitions : hole burning

The equations above are all based on Lorentzian shaped absorption profiles. When the particles have a velocity distribution function $P(v_z)$, with v_z the velocity in one direction, equations 2.98 and 2.99 change to :

$$\begin{aligned}\frac{\mathrm{d}N_k(v_z)}{\mathrm{d}t} = C_k P(v_z) - \frac{N_k(v_z)}{\tau_k} \\ -\left(N_k(v_z)B_{ki}^{I(\omega)} - N_i(v_z)B_{ik}^{I(\omega)}\right)\cdot I^{\omega} g(v_z,\omega)\end{aligned}, \qquad 2.107$$

$$\begin{aligned}\frac{\mathrm{d}N_i(v_z)}{\mathrm{d}t} = C_i P(v_z) - \frac{N_i(v_z)}{\tau_i} \\ +\left(N_k(v_z)B_{ki}^{I(\omega)} - N_i(v_z)B_{ik}^{I(\omega)}\right)\cdot I^{\omega} g(v_z,\omega)\end{aligned}, \qquad 2.108$$

where $g(v_z,\omega)$ is the Lorentzian absorption profile of atoms moving with velocity v_z. The atoms see a wave of angular frequency $\omega - \mathbf{v}\cdot\mathbf{k}$. When the z-axis is chosen in the direction of $\mathbf{k}$:

$$g(v_z,\omega) = \frac{\frac{\Gamma_k}{2\pi}}{\left(\omega(1-\frac{v_z}{c}) - \omega_{ki}\right)^2 + \frac{\Gamma_k^2}{4}}. \qquad 2.109$$

For the steady-state solution, it can be evaluated that :

$$\frac{N_k(v_z)}{g_k} - \frac{N_i(v_z)}{g_i} = \left(\frac{N_k^0}{g_k} - \frac{N_i^0}{g_i}\right) P(v_z)\left[1 + S(v_z,\omega)\right]^{-1}, \qquad 2.110$$

with :

$$S(v_z,\omega) = \tau^* g_k B_{ki}^{I(\omega)} I^{\omega} g(v_z,\omega) \qquad 2.111$$

the saturation parameter for hole burning.

In the absence of laser light ($I^{\omega} = 0$) the inversion density is proportional to the velocity distribution function. At small, but non-zero values of I^{ω} a reduction in the distribution occurs at the value $v_z = (\omega - \omega_{ki})/k$. The laser "burns a hole" in the velocity distribution, see figure 2.4. This hole is called a Bennet hole. The width of the hole may be evaluated by assuming that $P(v_z)$ is constant over the hole. This leads to a width, which

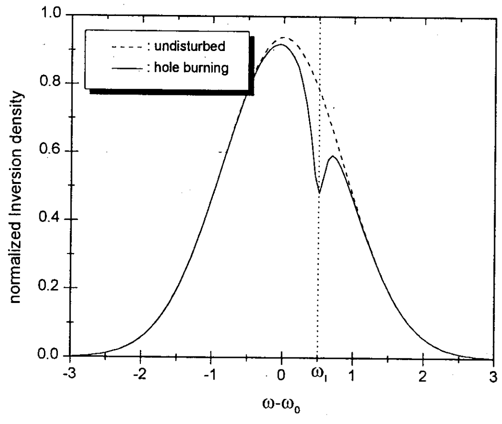

Figure 2.4: The effect of hole burning.

depends on the intensity of the laser, similar to the broadening described in equation 2.106.

If the intensity is low compared to the saturation intensity a change in the inversion density is created, which is proportional to the value of the velocity distribution function. If the velocity distribution variations are significant on velocity scales larger than $\Gamma_k\omega_{ki}/c$, scanning ω around ω_{ki} results in a change in the inversion density which is proportional to $P(v_z)$.

In order to measure the width of the saturated absorption line, the laser which creates the Bennet hole can be reflected back into the plasma, inducing a second Bennet hole. The second beam follows the same trajectory as the primary beam, but in the opposite direction. Only when the laser frequency is set close to the absorption frequency for stationary particles, a reduction of the signal is measured. This dip, centered around ω_{ki} is called Lamb dip. The width of this dip can be evaluated[4] in the same way as in the previous section, to be equal to the saturated absorption width, as defined in equation 2.106. Measurement of the Lamb dip provides a tool to compare the saturated absorption width and the width of the velocity distribution function.

2.5. Doppler shifted laser induced fluorescence (DSLIF)

With laser induced fluorescence (LIF) electrons are excited from level 0 to level 1 by laser radiation. The fluorescence signal is formed by the spontaneous emission from level 1 to level 2 (see figure 2.5). The atoms and ions in the investigating area are distributed according to Maxwell, which means that the spectral lines are Doppler broadened. The spectral width of the laser line is much narrower than the Doppler width. By scanning the laser frequency over the absorption spectrum of the particles, velocity information is obtained by looking at the signal produced by the decay from level 1 to level 2. This technique is called Doppler shifted laser induced fluorescence (DSLIF).

2.5.1. A 3-level system

The theory for a 3-level system uses the same approach as for the 2-level system in section 2.4.3. In this situation, the laser produces light with a spectral distribution which can be described by :

$$\begin{aligned} I(\omega')\mathrm{d}\omega' &= I^{\omega}\cdot L_{\Gamma_L}\left(\omega'-\omega_L\right)\mathrm{d}\omega' \\ &= I^{\omega}\cdot\frac{\Gamma_L/2\pi}{\left(\omega'-\omega_L\right)^2+\Gamma_L^2/4} \end{aligned} \qquad 2.112$$

Where I^{ω} is the total intensity of light distributed around ω_L with a line width Γ_L. The resulting absorption probability is :

$$\begin{aligned} P_{01}\left(v_z,\omega_L\right) &= B_{01}\omega_{10}^3\, I^{\omega}\int_{-\infty}^{\infty}\frac{g_{\Gamma_a}(v_z,\omega')}{\omega'^3}\,L_{\Gamma_L}\left(\omega'-\omega_L\right)\mathrm{d}\omega' \\ &= B_{01}\cdot\Phi_{\omega_L}^{\omega_{10}}\left(v_z,\omega_L\right) \end{aligned} \qquad 2.113$$

In which $g_{\Gamma_a}\left(v_z,\omega'\right)$ is the absorption function for a particle moving with a velocity component v_z in the z-direction of the laser and interacting with Doppler-shifted light, see equation 2.109. Γ_a is the reciprocal of the lifetime of the upper state (1). If $\Gamma_a \gg \Gamma_L$

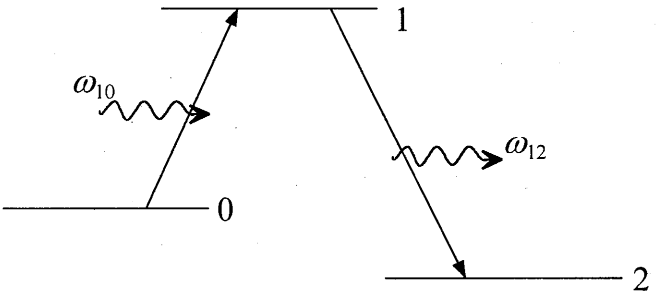

Figure 2.5 : The 3 level diagram.

then :

$$\Phi_{\omega_L}^{\omega_{10}}\left(v_z,\omega_L\right) = I^{\omega} g_{\Gamma_a}\left(v_z,\omega_L\right) = I^{\omega} L_{\Gamma_a}\left(\omega_L\left(1-\frac{v_z}{c}\right)-\omega_{10}\right) \tag{2.114}$$

Now, the rate equations can be constructed with the same approach as in equations 2.98 and 2.99.

In the stationary situation all time derivatives are zero and the equations can be evaluated to :

$$\begin{aligned}\frac{N_1(v_z,\omega_L)}{g_1} &= P\left(v_z\right)\cdot C_1\frac{\tau_1}{g_1}\left[\frac{1+\left(1+\dfrac{C_0}{C_1}\right)\dfrac{S^{\Phi}\left(v_z,\omega_L\right)}{1+\dfrac{\tau_1}{\tau_0}\dfrac{g_0}{g_1}}}{1+S^{\Phi}\left(v_z,\omega_L\right)}\right], \\ &= \frac{N_1^0}{g_1}\cdot P(v_z)\cdot\left[\frac{1+\eta S^{\Phi}\left(v_z,\omega_L\right)}{1+S^{\Phi}\left(v_z,\omega_L\right)}\right]\end{aligned} \tag{2.115}$$

with

$$\eta = \left(\frac{1+\dfrac{C_0}{C_1}}{1+\dfrac{g_0}{g_1}\dfrac{\tau_1}{\tau_0}}\right). \tag{2.116}$$

Again, a saturation parameter is introduced :

$$S^{\Phi}\left(v_z,\omega_L\right) = \tau * g_1 B_{10}\Phi_{\omega_L}^{\omega_{10}}\left(v_z,\omega_L\right). \tag{2.117}$$

The total number of photons per second emitted by the decay of electrons from level 1 to level 2 is given by :

$$\begin{aligned}R_{tot}\left(\omega_L\right) &= A_{12}\cdot\int_{-\infty}^{\infty} N_1\left(v_z,\omega_L\right)\cdot \mathrm{d}v_z \\ &= C_1\tau_1 A_{12}\cdot\left[1+\int_{-\infty}^{\infty} P\left(v_z\right)\cdot T_{\omega_L}^{\omega_{10}}\left(v_z,\omega_L\right)\mathrm{d}v_z\right], \\ &= R_0 + R_{LIF}\left(\omega_L\right)\end{aligned} \tag{2.118}$$

with

$$T_{\omega_l}^{\omega_{10}}\left(v_z,\omega_L\right) = \frac{(\eta-1)S^{\Phi}\left(v_z,\omega_L\right)}{1+S^{\Phi}\left(v_z,\omega_L\right)}. \tag{2.119}$$

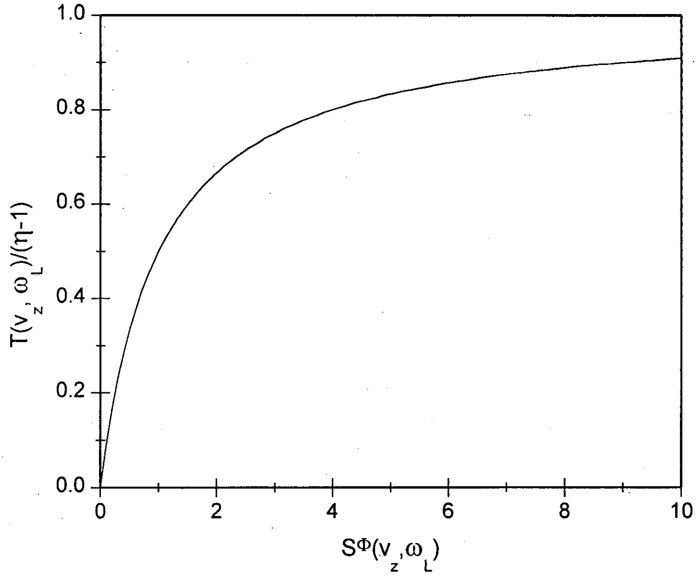

Figure 2.6: Relation between the *T*-function and the saturation parameter.

This relation is drawn in figure 2.6. Equation 2.118 shows that the signal consists of an normal decay contribution R_0 and an extra Doppler shifted LIF part R_{LIF}. The latter is the convolution of the velocity distribution and the *T*-function. When the laser wavelength is not near the Doppler shifted absorption frequency :

$$\left|\omega_L\left[1-\frac{v_z}{c}\right]-\omega_{10}\right| >> \Gamma_a, \Gamma_L, \qquad 2.120$$

the *S* and *T*-functions will be zero, resulting in a zero DSLIF signal rate. If the laser frequency is set on the velocity-corrected absorption frequency and when the laser line is much smaller than the absorption linewidth ($\Gamma_L \ll \Gamma_a$), equations 2.114 and 2.117 show that the saturation parameter is Lorentzian :

$$\begin{aligned} S^{\Phi}\left(v_z,\omega_L\right) &= \tau^* g_1 B_{10} I^{\omega} L_{\Gamma_a}\left(\omega_L\left(1-\frac{v_z}{c}\right)-\omega_{10}\right) \\ &= \frac{I^{\omega}}{I_{sat}}\frac{\pi\Gamma_a}{2} L_{\Gamma_a}\left(\omega_L\left(1-\frac{v_z}{c}\right)-\omega_{10}\right) \quad , \\ &= S_0^{\Phi} L_{\Gamma_a}\left(\omega_L\left(1-\frac{v_z}{c}\right)-\omega_{10}\right) \end{aligned} \qquad 2.121$$

with I_{sat} the saturation intensity, which determines the laser intensity for which the saturation parameter is unity at its maximum. The corresponding T-function is under these circumstances also Lorentzian :

$$T_{\omega_L}^{\omega_{10}}\left(v_z,\omega_L\right) = \left(\eta-1\right)\frac{S_0^{\Phi}}{\sqrt{1+\dfrac{2S_0^{\Phi}}{\pi\Gamma_a}}}\frac{\dfrac{\Gamma_a^*}{2\pi}}{\left(\omega_L\left[1-\dfrac{v_z}{c}\right]-\omega_{10}\right)^2+\left(\dfrac{\Gamma_a^*}{2}\right)^2} , \qquad 2.122$$

with the saturated line width Γ_a^* defined as :

$$\Gamma_a^* = \Gamma_a\sqrt{1+\frac{2S_0^{\Phi}}{\pi\Gamma_a}} = \Gamma_a\sqrt{1+\frac{I^{\omega}}{I_{sat}}} . \qquad 2.123$$

It can be seen that due to saturation, the T-function broadens and increases for an increasing laser intensity. If the saturated absorption width is much smaller than the profile of the velocity distribution function $P(v_z)$, the DSLIF rate is directly related to this profile. According to equations 2.118 :

$$R_{LIF}\left(\omega_L\right) = C_1\tau_1 A_{12}\left(\eta-1\right)\frac{S_0^{\Phi}}{\sqrt{1+\dfrac{2S_0^{\Phi}}{\pi\Gamma_a}}} P\left(v_z = c\frac{\omega_L-\omega_{10}}{\omega_L}\right) . \qquad 2.124$$

In this case, saturation only influences the intensity of the DSLIF signal, while the frequency profile is an image of the velocity distribution function.

References

[1] *Classical Electrodynamics* : J.D. Jackson; John Wiley & Sons, ISBN 0-471-43132-X

[2] *Atomic and Laser Spectroscopy* : A. Corney; Clarendon Press - Oxford, ISBN 0-19-851148-5

[3] *Quantum Electronics* : A. Yariv; Wiley & Sons, ISBN 0-471-97176-6

[4] *Laser Spectroscopy, Basic Concepts and Instrumentation* : W. Demtröder; Springer (1996), ISBN 3-540-57171-X

3. The Bohm criterion and presheath theory

3.1. Introduction

The region between the plasma and the wall determines the etching effects on the substrate. Theoretically, the transition region can be divided into two parts. First, the presheath where the ions are accelerated to the Bohm velocity. After that, the ions enter the sheath, where they are accelerated towards the wall. Here, the quasi-neutrality of the plasma is violated.

In this chapter a theory which describes the development of various quantities in the sheath and presheath region is presented. For simplicity, some assumptions have to be made.

The sheath region is expected to be collisionless. Since the Debye length λ_D is a typical length scale for the size of the sheath, the collisionless assumption is valid if the mean free path for collisions is much larger than the Debye length.

It is also assumed that the electrons in the plasma volume are distributed according to Boltzmann. Their distribution is determined by the electron temperature T_e. All particles which reach the wall will be absorbed. In first approximation, the ions are mono-energetic and cold ($T_i = 0$).

The theory in this chapter is based on the review article of Riemann[1].

3.2. Sheath theory

In this theory the sheath is the transition region from a neutral non-magnetized plasma with singly charged ions to an absorbing wall. The electrons, which have a higher mobility than the ions, charge the wall negatively. This results in an area where the electrons are repelled and the ions are accelerated. When the parameter z defines the distance to the wall, a dimensionless quantity is introduced to be used as the space coordinate in the sheath :

$$\xi = \frac{z}{\lambda_D}, \qquad 3.1$$

where the Debye length λ_D is defined as :

$$\lambda_D = \sqrt{\frac{\varepsilon_0 k T_e}{N_0 e^2}}. \qquad 3.2$$

T_e is the mean energy or temperature of the electrons, k is the Boltzmann constant, N_0 is the density of charged particles, e is the elementary charge, and ε_0 is the permittivity of free space. Also for the kinetic energy ($\frac{1}{2} m_i v_z^2$), the potential energy ($e\phi$), and the ion and electron densities ($N_{i,e}$), dimensionless quantities can be defined :

$$y = \frac{\frac{1}{2} m_i v_z^2}{kT_e}, \tag{3.3}$$

$$\chi = -\frac{e\phi}{kT_e}, \tag{3.4}$$

$$n_{e,i} = \frac{N_{e,i}}{N_0}. \tag{3.5}$$

The quantities on the edge of the sheath (ξ=0) are indicated by the subscript 0. Inside the sheath, the flux of ions must be constant, so :

$$n_i y^{1/2} = y_0^{1/2}. \tag{3.6}$$

The energy of the ions is conserved (no collisions) :

$$y = y_0 + \chi. \tag{3.7}$$

The electrons are distributed according to Boltzmann :

$$n_e = \exp[-\chi]. \tag{3.8}$$

The Poisson equation yields :

$$\frac{\mathrm{d}^2\chi}{\mathrm{d}\xi^2} = n_i - n_e. \tag{3.9}$$

Combining equations 3.6 and 3.7 results in :

$$n_i = \frac{1}{\sqrt{1 + \chi/y_0}}. \tag{3.10}$$

Inserting this result and equation 3.8 into the Poisson equation (3.9) :

$$\frac{\mathrm{d}^2\chi}{\mathrm{d}\xi^2} = \frac{1}{\sqrt{1 + \chi/y_0}} - \exp[-\chi]. \tag{3.11}$$

Integration of the equation above after multiplication with $\mathrm{d}\chi/\mathrm{d}\xi$ gives :

$$\left(\frac{\mathrm{d}\chi}{\mathrm{d}\xi}\right)^2 = 4y_0\left[\sqrt{1 + \chi/y_0} - 1\right] + 2\left(\exp[-\chi] - 1\right), \tag{3.12}$$

where the boundary conditions

$$\chi, \frac{\mathrm{d}\chi}{\mathrm{d}\xi} \xrightarrow{\xi \to -\infty} 0 \tag{3:13}$$

indicate no electric field in the plasma. Calculations show that only for $y_0 \geq 0.5$ the boundary conditions are satisfied. This can also be visualized using the Taylor expansion of equation 3.12 for small χ :

$$\left(\frac{\mathrm{d}\chi}{\mathrm{d}\xi}\right)^2 = \left(1 - \frac{1}{2y_0}\right)\chi^2 + O(\chi^3), \tag{3.14}$$

causing a contradiction for $y_0 < 0.5$.
The condition $y_0 \geq 0.5$ or :

$$v_{0z} \geq v_B = \sqrt{\frac{kT_e}{m_i}} \qquad 3.15$$

is known as the "Bohm criterion"[2,3] for the formation of the sheath. The velocities of the ions at the edge of the sheath have to exceed the critical value of the Bohm velocity v_B. The criterion implies also, according to equation 3.12, that in the sheath region the electron density decreases faster than the ion density.

3.3. Presheath formation

The previous section indicates that in order to fulfill the Bohm criterion, the ions must enter the sheath region with a velocity determined by the electron temperature. Usually, the electron temperature exceeds the ion temperature by several orders. Therefore, a small field must be present between the plasma and the sheath to accelerate the ions to the Bohm velocity. This region is named the "presheath"[4]. To develop a theory for this region, a quantity L is defined as the typical length scale of the presheath. A scaling parameter ε is introduced to relate the scales of the presheath to the sheath :

$$\frac{\lambda_D}{L} \equiv \varepsilon . \qquad 3.16$$

The value of L is much larger than the Debye length, so $\varepsilon \ll 1$. Because the sheath is defined through ion continuity and energy conservation, the presheath is determined by the violation of one of these relatons. Therefore, the quantity L is defined as :

a) the ion mean free path
b) the ionization length
c) geometry of the system

In the same way as in the previous chapter, a dimensionless space coordinate is introduced . Again the notation of Riemann[1] is followed :

$$x = \frac{z}{L}, \qquad 3.17$$

where the sheath edge is at $x = 0$ and the potential $\chi(0) = 0$. Poisson's equation changes to :

$$\varepsilon^2 \frac{\mathrm{d}^2 \chi}{\mathrm{d}x^2} = n_i(\chi, x) - n_e(\chi) . \qquad 3.18$$

Because ε is small, quasi-neutrality is obtained. With this, the presheath equations are evaluated. The ion density is :

$$n_i = \frac{j_i}{\sqrt{y}}, \tag{3.19}$$

where current density J_i is made dimensionless by :

$$j_i = \sqrt{\frac{m_i}{2kT_e}}\frac{J_i}{N_0}. \tag{3.20}$$

The electron density balances the ion density :

$$\frac{j_i}{\sqrt{y}} = \exp[-\chi]. \tag{3.21}$$

Taking the natural logarithm of equation 3.21 and differentiating it to x yields :

$$\frac{1}{2y}\frac{\mathrm{d}y}{\mathrm{d}x} - \frac{\mathrm{d}\chi}{\mathrm{d}x} = \frac{1}{j_i}\frac{\mathrm{d}j_i}{\mathrm{d}x}. \tag{3.22}$$

Inside the presheath, where the Bohm criterion is not yet fulfilled ($y < 0.5$) :

$$\frac{\mathrm{d}y}{\mathrm{d}x} - \frac{\mathrm{d}\chi}{\mathrm{d}x} < \frac{1}{j_i}\frac{\mathrm{d}j_i}{\mathrm{d}x}. \tag{3.23}$$

The energy conservation law of equation 3.7 can be written as (after differentiation to x) :

$$\frac{\mathrm{d}y}{\mathrm{d}x} - \frac{\mathrm{d}\chi}{\mathrm{d}x} \leq 0. \tag{3.24}$$

The above relation equals zero when no energy loss is taken into account. Combining the relations above shows the possible situations :

1. $\mathrm{d}j_i/\mathrm{d}x > 0$ and no energy loss (equation 3.24) : The ion current density increases, when approaching the wall.
2. $\mathrm{d}y/\mathrm{d}x < \mathrm{d}\chi/\mathrm{d}x$: indicating energy loss due to a retarding force (friction) in the presheath.

These two cases can be expanded to the three situation described in the beginning of the section :

a) *Collisional presheath* : the ions loose their energy due to collisions, resulting in a $\mathrm{d}y/\mathrm{d}x < \mathrm{d}\chi/\mathrm{d}x$, determined by L, which is the ion mean free path.
b) *Ionizing presheath* : ions are created in the presheath. The current density j_i increases when approaching the wall. The parameter L is defined as the ionization length.
c) *Geometric presheath* : the current density increases because the potential distribution is not planar. L is defined as the curvature radius.

To investigate these cases, dimensionless quantities are introduced for the ion mean free path $\lambda(v_z)$, in terms of the collision cross section, and for the ionization rate S_i :

$$q(y)=\frac{L}{\lambda}, \tag{3.25}$$

$$r(\chi)=L\sqrt{\frac{m_i}{2kT_e}\frac{S_i}{N_0}}. \tag{3.26}$$

For simple geometries, the current continuity can be written as (after linearization) :

$$\frac{1}{A}\frac{\mathrm{d}}{\mathrm{d}x}\left(Aj_i\right)=r, \tag{3.27}$$

where

$$A(x)=(1\mp x)^{\beta} \tag{3.28}$$

is the surface area of a plane at distance x. For planar geometry $\beta=0$, for cylindrical $\beta=1$, and for spherical $\beta=2$. This changes equation 3.22 into :

$$\frac{1}{2y}\frac{\mathrm{d}y}{\mathrm{d}x}-\frac{\mathrm{d}\chi}{\mathrm{d}x}=\frac{r}{j_i}-\frac{1}{A}\frac{\mathrm{d}A}{\mathrm{d}x}, \tag{3.29}$$

and the momentum balance :

$$\frac{\mathrm{d}y}{\mathrm{d}x}-\frac{\mathrm{d}\chi}{\mathrm{d}x}=-2y\left[q+\left(r/j_i\right)\right]. \tag{3.30}$$

Equations 3.29 and 3.30 can be solved analytically for the geometric presheath around a spherical probe. Then $A=(1-x)^2$, $q=0$, and $r=0$:

$$x=1-\exp\left[\frac{\chi}{2}\right](1+2\chi)^{-1/4}, \tag{3.31}$$

after applying the boundary conditions $x,\chi\rightarrow 0$ for $y\rightarrow 0.5$ and $y\rightarrow 0$ for $x\rightarrow -\infty$.
In front of a planar electrode, $A=1$, and equation 3.29 does not contain a dependence on A. When the presheath is dominated by collisions, $q=1$ and $r=0$. In this case, the potential in the presheath can be evaluated by applying the same boundary conditions as before :

$$x=\frac{1}{2}\left(1-\exp[-2\chi]-2\chi\right). \tag{3.32}$$

The sheath length parameter L is then determined by the mean free path of the ions :

$$L=L_c\equiv\lambda_c=\frac{1}{N_g\sigma_c}, \tag{3.33}$$

where L_c is defined as the length parameter of the collisional presheath and N_g the gas density. The last equality is only valid when the collision cross-section is independent of the velocity of the ion and when the ions completely transfer their momentum to the neutral. In charge exchange collisions the q parameter should be changed to include the transfer of the total momentum during the collision :

$$q=L\left(\frac{1}{2\lambda_{el}}+\frac{1}{\lambda_{ce}}\right), \tag{3.34}$$

with λ_{el} the mean free path for elastic collisions and λ_{ce} the mean free path for charge exchange collisions, both determined by their cross-sections, analogous to equation 3.33.

When ionization dominates the build-up of the presheath, collisions can be neglected (q=0) and an ionization rate S_i can written as :

$$S_i = N_g N_e \langle \sigma_i v_e \rangle = N_g N_0 \langle \sigma_i v_e \rangle \exp[-\chi], \tag{3.35}$$

depending on the density of neutrals N_g and on the overlap of the cross-section and the velocity distribution of the electrons. This results in :

$$r = \exp[-\chi] \tag{3.36}$$

and

$$L = L_i \equiv \frac{1}{N_g \langle \sigma_i v_e \rangle} \sqrt{\frac{kT_e}{m_i}}, \tag{3.37}$$

with L_i the length parameter of the ionizing presheath. Using this in equations 3.29 and 3.30 and applying the same boundary conditions results in the analytical expression :

$$\begin{gathered} x = \sqrt{2}\left[\arctan X - \frac{1}{2}X + \frac{1}{2} - \frac{\pi}{4}\right]. \\ X = \sqrt{2\exp[\chi] - 1} \end{gathered} \tag{3.38}$$

When both ionization and collisions should be taken into account, it is useful to define L as :

$$L = \frac{L_c L_i}{L_c + L_i} \tag{3.39}$$

and to introduce a constant α :

$$\alpha = \frac{L_c}{L_c + L_i} = \frac{1}{1 + \dfrac{\sigma_c}{\langle \sigma_i v_e \rangle}\sqrt{\dfrac{2kT_e}{m_i}}}. \tag{3.40}$$

When α=0, the presheath is collisional. When α=1, ionization is dominant.
Introducing L changes q and r in equations 3.25 and 3.26 :

$$\begin{gathered} q = \frac{L}{L_c} \\ r = \frac{L}{L_i}\exp[-\chi] \end{gathered}, \tag{3.41}$$

resulting in the presheath equations :

$$\frac{1}{2y}\frac{\mathrm{d}y}{\mathrm{d}x} - \frac{\mathrm{d}\chi}{\mathrm{d}x} = \alpha y^{-\frac{1}{2}}, \tag{3.42}$$

$$\frac{\mathrm{d}y}{\mathrm{d}x} - \frac{\mathrm{d}\chi}{\mathrm{d}x} = -2y\left(1 - \alpha + \alpha y^{-\frac{1}{2}}\right). \tag{3.43}$$

These can be evaluated to :

$$\frac{\mathrm{d}\chi}{\mathrm{d}x} = S_\alpha(y)\frac{\mathrm{d}y}{\mathrm{d}x}, \tag{3.44}$$

with

$$S_\alpha(y) = \frac{1-\alpha+2\alpha y^{-\frac{1}{2}}}{2y\left(1-\alpha+\alpha y^{-\frac{1}{2}}\right)+\alpha y^{-\frac{1}{2}}}. \tag{3.45}$$

Integrating over x and applying the boundary conditions $y(\chi = 0) = 0.5$ yields :

$$\chi = \int_0^\chi \mathrm{d}\chi' = \int_{1/2}^{y(\chi)} S_\alpha(y')\mathrm{d}y'. \tag{3.46}$$

Also x can be evaluated as an integral over y with $y(x=0) = 0.5$:

$$x = \int_0^x \mathrm{d}x' = \int_{1/2}^{y(x)} \frac{\frac{1}{2}-y'}{\alpha(1+2y')y'^{\frac{1}{2}}+2(1-\alpha)y'^2}\mathrm{d}y'. \tag{3.47}$$

The numerically computed solutions of the two integrals are combined and shown in figure 3.1 for various values of α.

The α=0 and α=1 solutions are the analytical expressions of equations 3.32 and 3.38.

It can be seen that the solution of α=0 is monotonously decreasing, requiring a residual

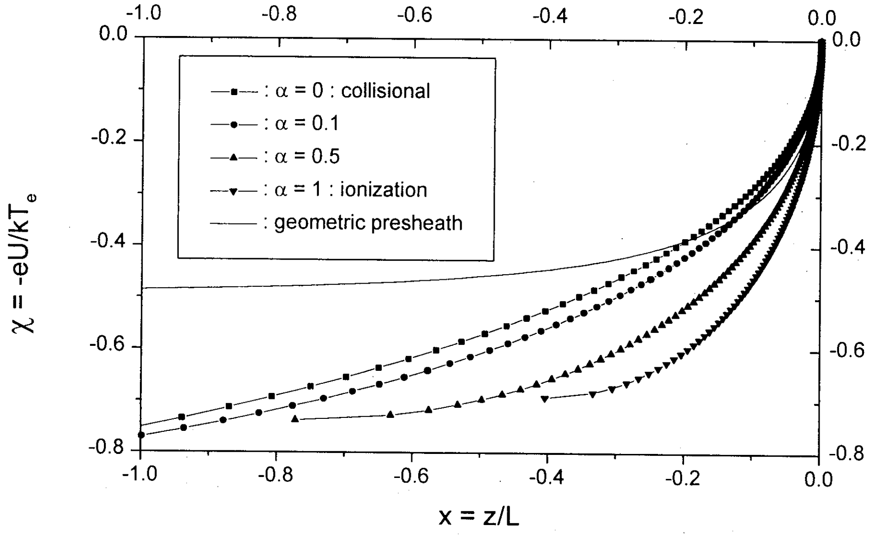

Figure 3.1 : Presheath potential for various cases.

field. The solution of $\alpha > 0$ stops at certain x values, where the electric field is zero. For α=1, $x_{\min} \approx 0.4$. Also the geometric presheath of equation 3.31 is shown. This solution tends towards $\chi = 0.5$ because of energy conservation. All solutions have a singularity at the sheath edge ($x = 0$). The increasing field leads to the violation of quasi-neutrality.

3.4. Modifications of the sheath - presheath theory

For generalization, an effective negative particle temperature is introduced :

$$\theta = \left(-\frac{\mathrm{d}n_-}{\mathrm{d}\chi}\bigg|_{\chi=0} \right)^{-1}, \qquad 3.48$$

where n_- is the dimensionless negative particle density. When Boltzmann distributed electrons are the only negative particles in the plasma, $\theta = 1$. When the plasma consists of two classes of negative particles, like in a two temperature plasma or a plasma with negative ions, θ changes to :

$$\theta = \frac{1+\kappa}{1+\alpha\kappa}, \qquad 3.49$$

with κ the ratio of the negative particle densities and α the ratio of the temperatures. The Bohm criterion for these generalized situations yields :

$$m_i \langle v_z \rangle_0^2 \geq \theta \cdot kT_e . \qquad 3.50$$

For ions having a non-zero temperature T_i, the sheath theory can be extended. The Bohm velocity in this case yields :

$$v_B' = \sqrt{\theta \cdot \frac{k(T_e + \gamma T_i)}{m_i}}, \qquad 3.51$$

with γ a constant equal to 1 for isothermal flow, 5/3 for adiabatic flow with isotropic pressure, and 3 for one-dimensional adiabatic flow.

For the development of a sheath model for ions with a certain velocity distribution function, a hydrodynamic formulation uses the separation of :

$$v_z = u + \zeta, \qquad 3.52$$

where $|\zeta| \ll u$. The mean velocity $u = \langle v_z \rangle$, and the random velocity $\langle \zeta^2 \rangle = kT_i/m_i$. The Bohm criterion for this situation yields :

$$m_i \langle v_z \rangle_0^2 \geq \theta \cdot k\left(T_e + 3T_i\right) \qquad 3.53$$

showing a one-dimensional adiabatic solution for the factor in front of the ion temperature (see equation 3.51). This indicates that in this approach, there is no interchange between the parallel and perpendicular ion velocity distribution functions on the scale of the sheath.

References

[1] K.-U. Riemann, *J. Phys. D : Appl. Phys* **24** (1991), pp493

[2] I. Langmuir, *Phys. Rev.* **33** (1929), pp954

[3] D. Bohm, *The Characteristics of Electrical Discharges in Magnetic Fields*, edited by A. Guthry and R.K. Wakerling (MacGraw-Hill (NY)) (1949) chapter 3, pp77

[4] P.N. Hu and S. Ziering, *Phys. Fluids* **9** (1966), pp2168

4. Plasma diagnostics

4.1. Introduction

To investigate the properties of various plasma configurations, it is necessary to experimentally determine the parameters which characterize the plasma. The electron, ion, and neutral densities and temperatures are examples of these parameters. Also the populations of the atomic and molecular energy levels, the ion velocities, the electric field, and the potential are important quantities. For the plasma physicist, several diagnostic methods are available to determine these parameters for the plasma under investigation.

In this chapter, the diagnostic tools used for the research described in this thesis are presented.

4.2. Optical emission spectroscopy (OES)

The light emitted from the plasma contains information about the density distribution of the energy states of the various species.

To obtain local information from the emitted radiation, an optical imaging technique (e.g. a lens system *L*) has to be used to focus a point (*S*) in the plasma on the detection system (*D*). To distinguish between the contributions from different transitions, a dispersion element, e.g. a monochromator, is used. This method is called optical emission spectroscopy (OES).

Usually, the detected light originates not only from the focus point (*S*) of the imaging system, but also from adjacent volumes. It is therefore not possible to measure the local emission signal directly. Often, the measured emission is integrated along a line of sight, which is determined by the small opening angle of the detection system *D*, or by

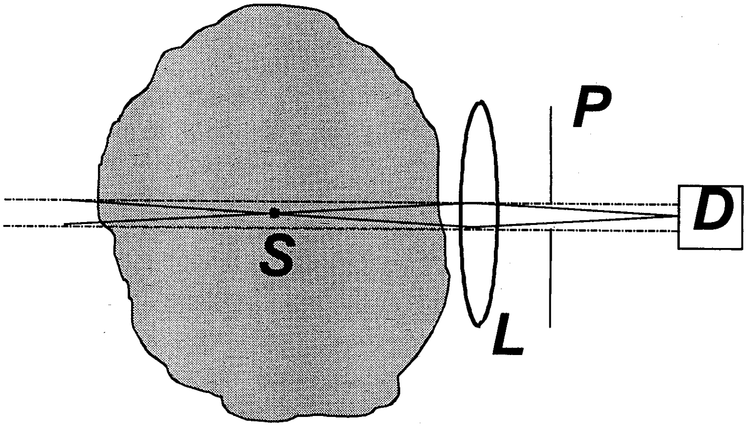

Figure 4.1 : 'Line of sight' emission spectroscopy setup. The point *S* is focused with lens *L* on the detector *D*. The observation angle is limited by the aperture *P*.

an aperture P, see figure 4.1.

In cylinder symmetric systems with coordinates (r,θ,z), multiple measurements along parallel lines of sight in the constant z-plane can be used to derive the local emission $I(r,z)$. A mathematical procedure, known as the Abel inversion, is necessary to convert the line integrated emission into local information. When the emission does not depend on the radial position r, Abel inversion is not needed and the measured line integrated intensity $I(z)$ is proportional to the emission from any point on the line of sight.

Besides the spatial dependence, a second item which can be investigated is the time dependence of the emitted light. The temporal emission is related to the time dependent source term for the population of the level which produces the emitted light. The time dependence of the upper level density $N(t)$ can have a phase difference compared to the source term for the population $C(t)$. This time dependence is caused by the non-zero lifetime τ of the upper level. The time evolution of the level density is given by :

$$\frac{\mathrm{d}N(t)}{\mathrm{d}t} = C(t) - \frac{N(t)}{\tau}. \qquad 4.1$$

If the lifetime is constant in time, the population rate $C(t)$ can be deduced from the density profile, as measured with OES, by rewriting equation 4.1 as :

$$C(t) = \frac{N(t)}{\tau} + \frac{\mathrm{d}N(t)}{\mathrm{d}t}. \qquad 4.2$$

Since the population rate $C(t)$ is periodic, the solution of equation 4.1 is given by[1] :

$$N(t) = \int_{-\infty}^{t} C(t-\xi)\exp\left(-\frac{t-\xi}{\tau}\right)\mathrm{d}\xi. \qquad 4.3$$

Using the above formula it is possible to predict the density when the source term is known.

In this thesis, only argon gas is used. Some of the levels of the argon atom and ion are shown in appendix A with their corresponding lifetimes.

4.3. Laser absorption spectroscopy

When a monochromatic light beam (e.g. a laser) is guided through a plasma, it can be partially absorbed. By tuning the laser frequency ν around an absorption frequency ν_0 of a transition of one of the species in the plasma, the intensity of the transmitted light shows a minimum at ν_0. When the transmission intensity is subtracted from the light intensity without absorption (no plasma), the absorption profile is obtained. This function is an addition of all local absorptions over a line of sight L. The change in intensity is determined by the absorption coefficient $\kappa(x,\nu)$, see equation 2.96 :

$$\kappa(x,\nu) = \frac{e^2}{4\varepsilon_0 m_e c} f_0 N(x) g(\nu), \qquad 4.4$$

with f_0 the oscillator strength for the transition, $N(x)$ the density of the lower level, and $g(\nu)$ the spectral profile of the absorption. When the velocities of the particles are distributed according to Maxwell-Boltzmann and pressure and saturation broadening effects can be neglected, the spectral profile $g(\nu)$ is Gaussian shaped, resulting in the absorption coefficient (see equation 2.68) :

$$\kappa(x,\nu)=\frac{e^2 f_0}{2\varepsilon_0 m_e c\gamma_D}\sqrt{\frac{\ln 2}{\pi}}N(x)\exp\left[-4\ln 2\left(\frac{\nu-\nu_0}{\gamma_D}\right)^2\right], \qquad 4.5$$

with the Doppler width (at half maximum) :

$$\gamma_D=\frac{2\sqrt{\ln 2}}{\lambda_0}\sqrt{\frac{2kT}{M}}, \qquad 4.6$$

with M the mass of the particle and T its temperature. In the above expression for the absorption coefficient it is assumed that the spectral shape is no function of x, indicating a constant temperature over the whole absorbing region. For the absorption over a distance l, equation 2.97 is used to deduce the absorption profile :

$$\begin{aligned}\ln\left(\frac{I(0,\nu)}{I(l,\nu)}\right)&=\frac{e^2}{4\varepsilon_0 m_e c}f_0 l\langle N\rangle g(\nu)\\&=\frac{e^2 f_0 l}{2\varepsilon_0 m_e c\gamma_D}\sqrt{\frac{\ln 2}{\pi}}\langle N\rangle\exp\left[-4\ln 2\left(\frac{\nu-\nu_0}{\gamma_D}\right)^2\right]'\end{aligned} \qquad 4.7$$

with $I\ (l,\nu)$ the intensity of the laser beam at position l and frequency ν and $<N>$ the density of the lower level, averaged over the distance l.
The integration of equation 4.7 yields :

$$S=\int_0^\infty \ln\left(\frac{I(0,\nu)}{I(l,\nu)}\right)\mathrm{d}\nu=\frac{e^2 l f_0}{4\varepsilon_0 m_e c}\langle N\rangle. \qquad 4.8$$

This shows that when calculating the logarithm of the ratio of the spectral intensity profile before and after absorption, the width of the profile corresponds to the temperature (equation 4.6) and the area under the curve corresponds to the density of the particles (equation 4.8).
In this thesis, the absorption profiles of argon metastable atoms are measured. The $1s_5$ and $1s_3$ levels can be excited by applying 772.376 nm ($1s_5\rightarrow 2p_7$) and 772.421 nm ($1s_3\rightarrow 2p_2$) light, respectively (see appendix A). For these transitions, the particle temperature T and the average "line of sight" particle density $<N>$ can be evaluated to :

$$\begin{aligned}T&=516(\gamma_D)^2\\\langle N\rangle&=\frac{1}{lf_0}3.8\cdot 10^{14}S'\end{aligned} \qquad 4.9$$

with γ_D and S in GHz, T in K, $<N>$ in m^{-3} and l in m.
The oscillator strengths are 0.0306 and 0.341 for the $1s_5$ and $1s_3$ metastable levels, see appendix A.

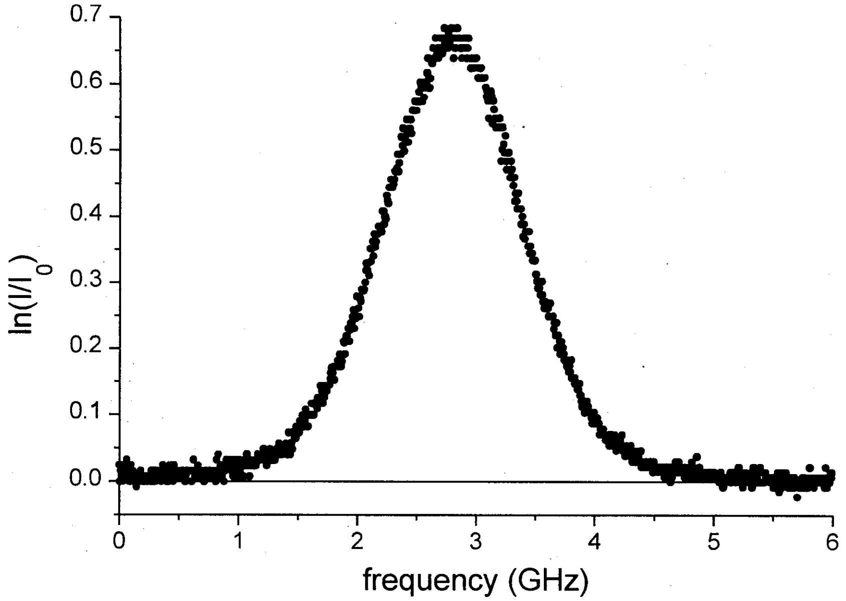

Figure 4.2 : Gaussian absorption profile of the $1s_5 \rightarrow 2p_7$ transition in a 0.5 Pa, 500 W argon plasma, generated in the ICP reactor of chapter 6.

To investigate these transitions a 772.4 nm IR diode laser with a 0.2 cm^2 beam is guided through the plasma. The power of the laser is kept below a few μW to avoid saturation. The transmission profile with and without the plasma are measured with an EG&G SGD100A photo diode and stored in a digital 500 MHz oscilloscope. The data is read from the oscilloscope by a PC and the absorption profile is calculated using equation 4.7. The density and temperature of the investigated level is deduced with PC software, which fits the data to Gaussian profiles.

In figure 4.2 an example of the $1s_5 \rightarrow 2p_7$ absorption profile is shown. The natural logarithm of the ratio of the intensity after and before the absorption is plotted. From this graph and with the use of equations 4.9 the gas temperature of 700 K and metastable density of $8 \cdot 10^{16}$ m^3 are deduced.

For an intensity of 0.1 Wm^{-2} (corresponding to 2 μW in 0.2 cm^2), the saturation parameter is smaller than 0.1 (see equation 2.103), under the assumption that the lifetime of the lower level is 10^{-6}s and in the situation that the linewidth of the laser is much smaller than the natural linewidth.

4.4. Langmuir Probe

4.4.1. Single probe theory

When a metal surface (a probe) at potential V is in contact with a plasma, it will collect a current I from the charged particles in this plasma, see figure 4.3. A counter electrode (mostly a grounded wall) closes the electric circuit. When a negative voltage (relative to the potential of the plasma, U_{plasma}) is applied to the probe, ions are extracted from the plasma. To balance the total current, the potential of the plasma decreases slightly, causing a larger negative flux to the counter electrode. When the area of the counter electrode is much larger than of the area of the probe, the changes in the plasma potential can be neglected and U_{plasma} is considered independent of the applied voltage.
A typical $I(V)$ characteristic of a cylindrical probe is shown in figure 4.4, where three regimes can be distinguished. When the potential of the probe V_p is higher than the plasma potential U_{plasma}, no ions are able to reach the probe surface and the measured current consists of electrons only. This is called the electron saturation regime (region C). When the potential is decreased below plasma potential, ions are able to reach the probe. Only a fraction $\exp[-e(V_p-U_{\text{plasma}})/kT_e]$ of the electrons will be able to reach the probe surface. In this intermediate regime (B) the zero current at floating potential V_f indicates the point where the ion and electron currents to the probe are equal. When the probe potential is much lower than the floating potential, only ions can reach the probe and the contribution of electrons can be neglected due to the exponential factor. This is the ion saturation regime (A).
The measured $I(V)$ profile is determined by the electron temperature and the charged particle density in the plasma. Here, only plasmas are considered with electrons and positive ions. The Langmuir probe is an often used tool to determine the electron temperature and the ion density is the plasma.
Theories which predict the ion saturation part of the probe characteristic have been subject of many discussions. In first approximation, only the ions which reach the

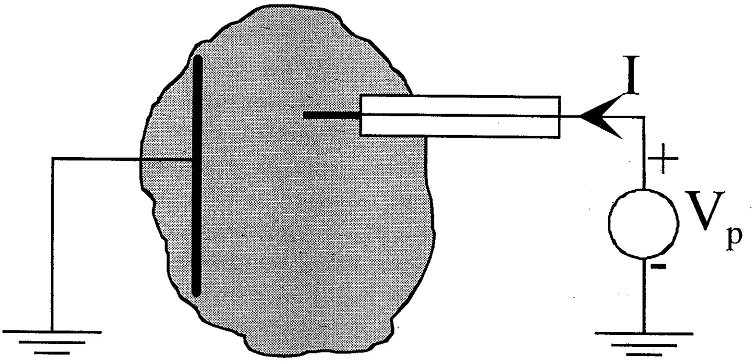

Figure 4.3 : Schematic of the single probe setup.

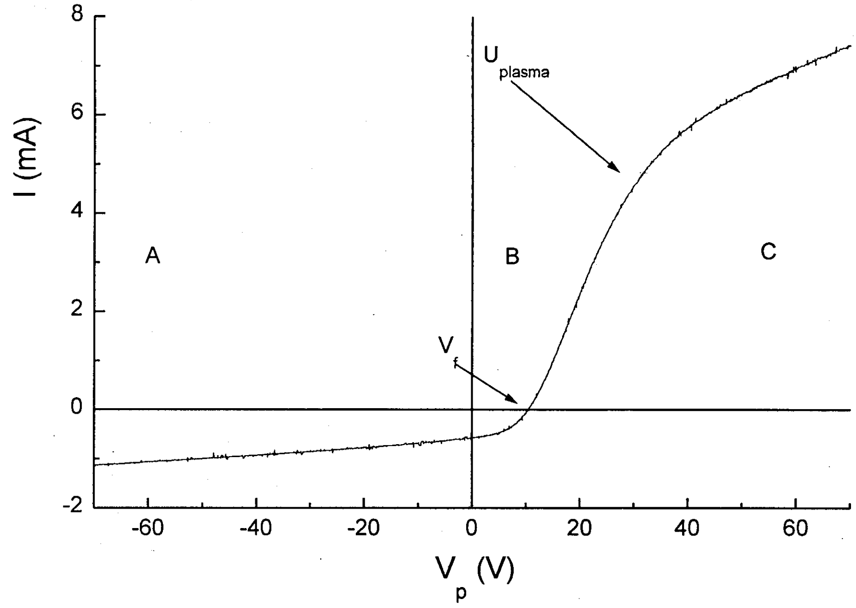

Figure 4.4 : Typical single probe trace, measured in an argon plasma, created in the ICP source of chapter 6.

outside of the "Debye shield" surrounding the probe are attracted to the probe and contribute to the ion current. The theories which describe the flux of ions to the probe depend on the plasma conditions in the vicinity of the probe. The mean free path of the ions λ_i, the Debye length λ_D, and the probe radius r_p are characteristic lengths which determine the validity of probe current theories. In the low pressure plasmas described here $\lambda_i \gg \lambda_D$ and the sheath can be considered collisionless.

The sheath is considered to be thick or thin, depending on the ratio of the Debye length and the probe radius. When $\lambda_D \gg r_p$, the orbital motion limit (OML) theory is used to describe the transport of ions in the thick sheath towards the probe surface. In the thin sheath limit (TSL), for $\lambda_D \ll r_p$, the ions in the sheath have an angular momentum which can be neglected and they cross the sheath radially.

The OML theory was introduced by Langmuir and Mott-Smith[2]. When applied to a cylindrical probe of surface A_p, the ion current to the probe can be evaluated. Using conservation of momentum and energy in the collisionless sheath, the following equation is obtained for a Maxwellian velocity distribution :

$$I_i = eN_i A_p \frac{2}{\sqrt{\pi}} \sqrt{\frac{kT_e}{2\pi m_i}} \left(\frac{e\left(U_{plasma} - V_p\right)}{kT_e} \right)^{1/2}, \qquad 4.10$$

with N_i the density of ions. Equation 4.10 is only valid in the ion saturation region, because it does not take the electron current into account. A common method to calculate the ion density from the probe trace is by plotting I_i^2 versus V_p. Equation 4.10 shows that the slope of the resulting straight line determines N_i. The axis crossing determines the plasma potential U_{plasma}.

The electron current to the probe for voltages below the plasma potential can be evaluated using equation 2.6 :

$$I_e = eN_e A_p \sqrt{\frac{kTe}{2\pi m_e}} \exp\left(-\frac{e\left(U_{plasma} - V_p\right)}{kT_e} \right), \qquad 4.11$$

with the use of the Maxwellian velocity distribution for the electrons.

When the ion and electron current are in equilibrium, the probe voltage is at floating potential, V_f. Combining equations 4.10 and 4.11 yields :

$$e\left(U_{plasma} - V_f\right) = \alpha k T_e, \qquad 4.12$$

with α a numerical factor. When this theory is applied to an argon plasma, $\alpha = 4.71$. The floating potential can directly be measured, so the electron temperature can be deduced using equation 4.12.

In cases when the OML theory is not justified, other approaches are being used. Chen[3] calculated solutions of the TSL theory equations given by Allen et al.[4] for various values of r_p/λ_D. In general, the ion current from Chen's curves can be fitted with :

$$I_i = I_{norm} a \left(\frac{e\left(U_{plasma} - V_p\right)}{kT_e} \right)^b, \qquad 4.13$$

with :

$$I_{norm} = \frac{2\pi\varepsilon_0 l k T_e}{r_p e} \sqrt{\frac{2kT_e}{m_i}}, \qquad 4.14$$

and a and b two constants depending on the ration of r_p/λ_D. Comparing Chen's curves with the measured characteristics results in fitted values for the a and b factors. From these, the ion density can be deduced directly.

4.4.2. Double probe theory

A Langmuir double probe consists of two single probes positioned close to each other, where the voltage V_a is applied over both probe tips. The whole system is insulated from ground, so the total current is conserved and a counter electrode is not needed. This has large advantages in systems with a less well defined ground, like the ICP

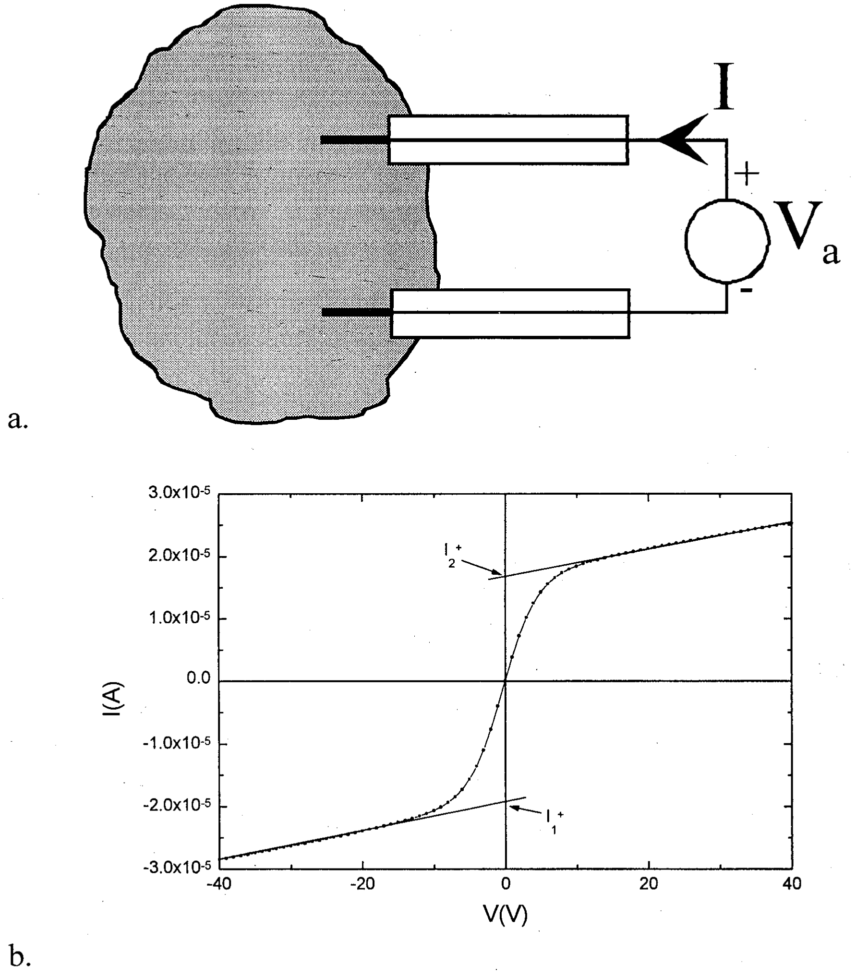

Figure 4.5 : Double probe system : a) Schematic setup. b) Typical measured double probe characteristic, as obtained in an argon plasma created in the 450 kHz source of chapter 5.

system in chapter 6. A schematic drawing of the double probe configuration is shown in figure 4.5a. In figure 4.5b a typical double probe $I(V)$ trace is shown. When the applied double probe voltage $V_a = 0$, both probe tips are at floating potential V_f, because no charge escapes from the system. The total current drawn from the plasma must be zero, therefore the ion currents to probe tips 1 and 2 must balance the electron currents :

$$I_{i1} + I_{i2} = -\left(I_{e1} + I_{e2}\right), \tag{4.15}$$

where the indices 1 and 2 refer to the respective probe. The random electron current to probe x can be written as :

$$I_{ex} = j_{ex} A_{px} \exp\left[\frac{e\left(V_x - V_{plasma}\right)}{kT_e}\right], \qquad 4.16$$

with A_{px} and V_x the area and potential of probe x. The random electron current density to probe x is j_{ex}. Using $V_2 - V_1 = V_a$ and equation 4.15 yields :

$$I_{i1} + I_{i2} = -I_{e1}\left[1 + \frac{j_{e2}}{j_{e1}} \frac{A_{p2}}{A_{p1}} \exp\left(-\frac{eV_a}{kT_e}\right)\right]. \qquad 4.17$$

If the areas of both probes are equal, $A_{p1} = A_{p2} = A_p$, and the random electron current densities are also equal, the total current through the double probe is then given by :

$$I = I_{e1} + I_{i1} = I_i \tanh\left[-\frac{eV_a}{2kT_e}\right], \qquad 4.18$$

where the ion current is assumed to be independent of the applied voltage :

$$I_{i1} = I_{i2} = I_i\,. \qquad 4.19$$

For large values of V_a, $|I| = I_i$.
At $V_a = 0$:

$$\left[\frac{\mathrm{d}I}{\mathrm{d}V_a}\right]_{V_a=0} = \frac{eI_i}{2kT_e}\,. \qquad 4.20$$

This equation is used for the fast determination of the electron temperature from the double probe characteristic.
In general, the assumption of equation 4.19 is only valid at $V_a = 0$. For other values of V_a, the ion currents to the tips are different. The contributions from the ion current (I_1^+, I_2^+) to the total current have to be determined (see figure 4.5b). To deduce the electron temperature, a different form of equation 4.20 is used :

$$\left[\frac{\mathrm{d}I}{\mathrm{d}V_a}\right]_{V_a=0} = \frac{1}{R_0} = \frac{1}{4}\left[I_1^+ + I_2^+\right]\frac{e}{kT_e}\,. \qquad 4.21$$

This method is known as the equivalent resistance (R_0) method.
In more general cases, the $I(V_a)$ characteristic of the double probe does not follow the function of equation 4.18. A more general relation can be used instead[5] :

$$I = C_1 + C_2 \tanh\left(-\frac{eV}{2kT_e} - C_3\right) + C_4 V\,, \qquad 4.22$$

with the constant C_4 incorporating the increasing Debye shield. A shift in the zero position of the probe characteristic is incorporated in the constants C_1 and C_3. The second derivative of I to V has two extrema, separated a distance ΔV. Evaluating equation 4.22 yields :

$$\frac{kT_e}{e} = \frac{\Delta V}{\beta}, \qquad 4.23$$

with

$$\beta = \ln\left(\frac{2+\sqrt{3}}{2-\sqrt{3}}\right) = 2.63\,. \qquad 4.24$$

This provides an easy way to determine the electron temperature from the double probe trace. When this approach is used for non-TSL situations, the results do not change dramatically. When it is applied to the OML, the difference is 5%[6].

4.4.3. Probe setup

In this work, a Langmuir double probe is used, consisting of two equally sized tungsten tips of a few millimeters length (see figure 4.6a). The rest of the tungsten wire is shielded from the plasma with a glass tube, a grounded metal shield and a glass cover. The tips are placed a few millimeters apart. The other ends of the tungsten wires are connected to a vacuum feed-through to be able to control the probe outside the plasma chamber. The whole probe system is fixed to bellows to move the probe in the plasma.

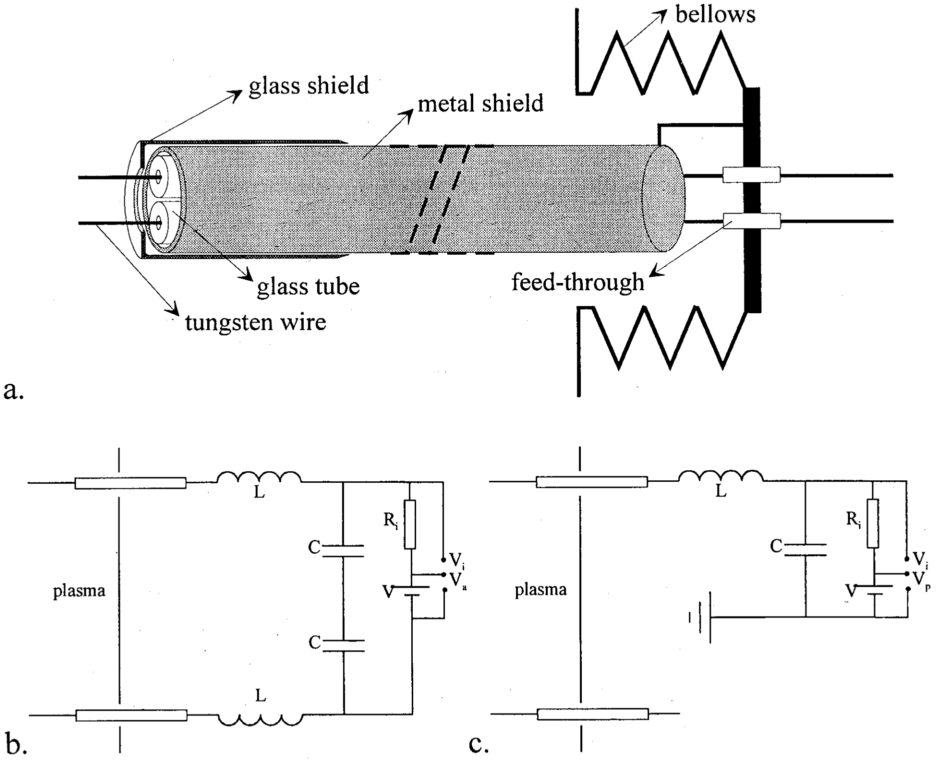

Figure 4.6 : Probe measurement setup. Part a. shows the schematic probe construction. The probe system can work in the double (b) or in the single probe configuration (c).

The probe is operated with an external circuit as shown in figure 4.6. In part b. the setup for a double probe is shown and in part c. for the single probe. A LC low-pass electronic filter, placed outside the vacuum, filters the RF pickup using a 220 nF capacitor and a 100 mH coil with a cut-off frequency of 1 kHz.

A floating voltage supply with a range of -60 to 60 V applies a differential voltage between the tips, without drawing current from the plasma to ground. The current through the probe is measured using the voltage drop V_i over a resistor R_i. When one probe tip is disconnected and the voltage supply is grounded at one side, the system works as a single probe, see figure 4.6c.

In principle the single probe works as a double probe, where the second tip is the grounded counter electrode, as shown in figure 4.3. A consideration must be made when the single probe is used in a plasma where the charged particles have a limited access to grounded surfaces, so the counter electrode is less well defined. In the absence of the counter electrode, it is not possible to draw current from the plasma. When the probe is biased with a voltage below floating potential, it will collect more ions than electrons, resulting in a decrease of the plasma potential, until the floating potential (which is directly related to the plasma potential through equation 4.12), equals the applied voltage level. When the bias voltage is higher than floating, the plasma potential increases. The single probe theories are based on the assumption that the plasma potential is independent of the applied voltage. It is clear that the assumption does not hold in the described situation.

In the presence of a counter electrode, a change in the plasma potential will induce a variation in the current to the electrode until it balances the current to the probe. This means, that the single probe theories are only justified when the current to the probe is balanced by a current to the counter electrode, which induces a negligible variation in the plasma potential. This situation can be created with a large counter electrode, placed inside the plasma. The change in electron current dI_e from a variation dU in the plasma potential can be evaluated by expanding equation 4.11 :

$$dI_e = \frac{dI_e}{dU_{plasma}} dU = I_e\left(U_{plasma}\right)\left(-\frac{e}{kT_e}\right) dU \,, \tag{4.25}$$

which is proportional to the electrode surface.

In situations where the counter electrode is not in full contact with the plasma, similar problems can occur. The random electron and ion fluxes to the counter electrode will be smaller, resulting in a larger changes of the plasma potential to balance the probe current. In this situation, the changes are larger when the probe is in the electron saturation regime than when it is in the ion saturation regime. This has two reasons. First, the current is larger in the electron saturation regime. This requires a larger current to the counter electrode, resulting in a larger change in the plasma potential. In the second place, when electrons are removed from the plasma, the random ion flux to the counter electrode determines the change in the plasma potential needed for the current equilibrium. In the ion saturation case, the random electron flux to the counter electrode determines the variation in the plasma potential. In general, electrons react much faster on changes in the plasma potential than ions. Therefore, in most cases where the charged particles have a limited access to the counter electrode, the ion saturation part of the probe trace can be used, while the electron saturation part cannot. Another factor which can influence the current to the probe is contamination. To remove a contamination layer from the probe, both probe tips are biased with large negative voltages. This produces a high energetic ion bombardment, which sputters the probe's surface. In plasmas where deposition is present, it is necessary to clean the probe between each measurement to have the same starting situation.

4.5. Doppler shifted laser induced fluorescence (DSLIF)

For the etch process it is important that the ion flux to the substrate has a limited degree of divergence to prevent under-etching. Inside the plasma the ions start with thermal velocities and are accelerated towards the Bohm velocity at the sheath edge. There, the ions are accelerated in the electric field, which is determined by the electrode potential, to gain their final energy with which they reach the wafer surface.

In low pressure plasmas, where the mean free path of the ions is much larger than the Debye length, the sheath is considered collisionless. In this case, the spread in the ion velocities at the surface is directly determined by the three dimensional ion velocity distribution function (IVDF) at the edge of the sheath. While traveling through the sheath, the velocity in the direction towards the electrode (z-direction) is increased, whereas the velocities in the perpendicular directions remain unchanged.

The only way to measure the local velocity distribution function (VDF) of the ions in the plasma is with Doppler shifted laser induced fluorescence (DSLIF). Using a laser, the ions are selectively pumped to a higher level when their velocity components in the direction of the laser beam fit to the Doppler shifted angular absorption frequency ω:

$$\omega - \omega_0 = \mathbf{k} \cdot \mathbf{v}\,, \tag{4.26}$$

with ω_0 the angular absorption frequency for stationary particles and $\mathbf{v}$ the three dimensional velocity vector. The wave vector $|\mathbf{k}| = \omega/c$ determines which component of the velocity is measured. When the direction of the laser beam is chosen as the z-axis, the frequency shift of the laser is :

$$\Delta\nu = \nu - \nu_0 = \lambda_0 v_z\,, \tag{4.27}$$

with λ_0 the absorption wavelength and v_z the velocity in the z-direction.

In this thesis the VDF's of argon ions in low pressure discharges are investigated. Unfortunately, at this moment it is not possible to use the DSLIF technique to determine the VDF of the ground state argon ions. The absorption wavelength to the first excited argon ion levels lies in the UV and the current state of laser technology does not provide a tunable, small bandwidth UV laser for this transition. Instead, the metastable $^2G_{9/2}$ ion level is used, which can be excited to the $^2F_{7/2}$ level with 611.493 nm. The particles which make the laser induced transition will decay to lower levels. In this work, the transition form the $^2F_{7/2}$ to the $^2D_{5/2}$ level at 461.0 nm is used (see appendix A), because the lifetime of the upper level is short and the main decay is by this transition.

For the visible light induced transition a stabilized single mode continuous wave dye laser is used. The dye fluid Rhodamine 6G has a large yield in this wavelength region. The frequency of these lasers is tunable and the spectral width is in general not broader than 1 MHz.

Despite the small bandwidth, the application of DSLIF requires a keen eye on the several mechanisms that cause broadening of the absorption profile. The most important in these low pressure discharges is saturation broadening. Therefore, the laser power must not be too high to keep the saturated absorption width below the Doppler width. The details of how to determine the width of the saturated absorption line are described in chapter 2. Several factors contribute to the saturation broadening. Firstly, the natural absorption profile, having a spectral width Γ_a, must be compared with the intensity profile of the laser. The total laser intensity is I_ω and the width is Γ_L. The convolution of these two profiles determines the saturation parameter $S^\Phi(v_z,\omega_L)$, see equations 2.113 and 2.117. In this case, the absorption width of 21.2 MHz (see appendix A) is much larger than the laser width, which is below 1 MHz. Therefore, when both profiles are being considered Lorentzian, the saturation parameter has a spectral width equal to Γ_a, while the Doppler theory determines the frequency of the laser ω_L at which the maximum absorption will occur :

$$\omega_L\left(1-\frac{v_z}{c}\right)=\omega_{10}, \qquad 4.28$$

with v_z the velocity component of the particle in the z-direction of the laser beam, c the speed of light, and ω_{10} is the absorption frequency for stationary ions. For pulsed lasers the spectral width is much larger and this simplification cannot be made.

The resulting DSLIF rate $R_{LIF}(\omega_L)$ from the upper level is, according to equation 2.118 determined by the convolution of the ion velocity distribution function $P(v_z)$ and the T-function, defined in equation 2.119. Under the conditions that the saturation parameter is Lorentz-shaped, the corresponding T-function is also a Lorentz function. Its width Γ_a^*, however, is determined by the magnitude S_0^Φ of the saturation parameter :

$$\Gamma_a^*=\Gamma_a\sqrt{1+\frac{2S_0^*}{\pi\Gamma_a}}=\Gamma_a\sqrt{1+\frac{I^\omega}{I_{sat}}}, \qquad 4.29$$

with I_{sat} the saturation intensity. This relation is shown in figure 4.7a. The T-function shows an increase for an increasing laser intensity, see figure 2.6. Figure 4.7b shows dependence of the DSLIF rate R_{LIF} on the laser intensity. From parts a. and b. can be seen that for intensities below the saturation intensity, the main cause for the increasing DSLIF rate is the higher laser intensity. When the intensity is above the saturation intensity, the broadening of the absorption profiles continues. Now, the DSLIF rate increases, because the broadening of the absorption line becomes important.

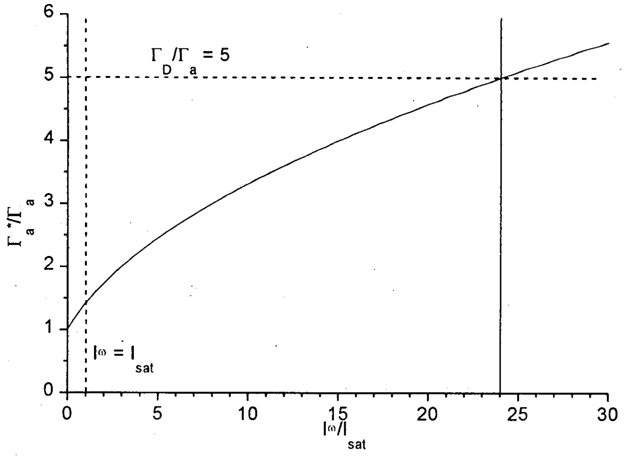

a.

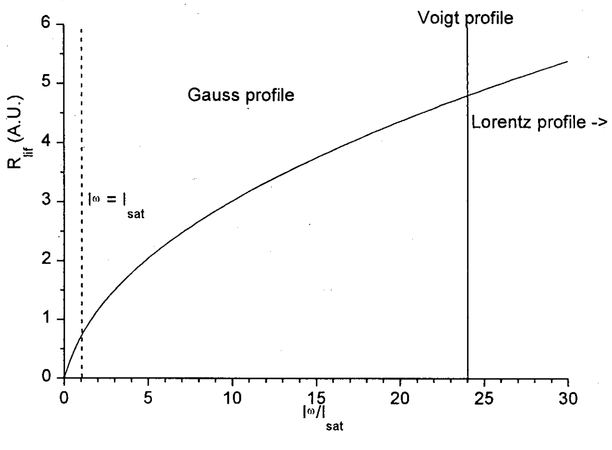

b.

Figure 4.7 : Variation of the absorption width (a) and the DSLIF rate (b) as a function of the laser intensity.

Particles having adjacent velocities are now also able to absorb the light and go to the higher level. The broadening at this stage is however low enough that the absorption width Γ_a^* is still below the Doppler width Γ_D of the particles. In this situation the spectral DSLIF profile is a good image of the velocity distribution profile of the particles which are probed, see equation 2.124. If the laser intensity increases above the level where the saturated absorption profile becomes comparable to the Doppler width, the DSLIF profile is not anymore a good image and the convolution of the velocity distribution and the absorption profile leads to a Voigt profile with a larger width. Further increase of the intensity leads to a larger broadening and to a spectral DSLIF profile, which is an image of the Lorentzian shaped absorption profile.

This evaluation shows that in order to measure the VDF with DSLIF, the saturated absorption width should always be smaller than the typical width of the VDF itself.

The 461.0 nm light from the upper level is focused from the plasma on a detection system containing a monochromator and a photomultiplier. Unfortunately, the upper level is also populated by electronic excitation from lower levels and by decay from higher levels. Therefore, the laser induced fluorescence is separated from the background emission signal with a lock-in technique. A chopper modulates the laser beam with a frequency around 300 Hz and the time varying component of the photomultiplier signal is extracted. In chapter 5 the lock-in technique uses photon counting to obtain the time resolved DSLIF signal and in chapter 6 the time averaged LIF signal is measured by applying the photomultiplier current to the input of a lock-in amplifier.

The intersection of the laser beam and the focus point of the detection system determines the position where the measurement takes place. The DSLIF technique therefore determines the local velocity distribution function of the particles.

Figure 4.8 shows a typical measurement setup for DSLIF. The dye laser (A) is guided through a chopper (B) after which it enters the plasma chamber (C). An element (D) to blow up or to limit the beam (e.g. an aperture) can be used to increase the signal intensity or to increase the detection resolution. The detection system (E) is placed perpendicular to the beam. It focuses the detection point (S) on the entrance slit of the monochromator (F). Optionally, an optical fiber (G) can be used to transport the light signal from the focus point to the entrance slit of the monochromator. The photomultiplier (H) converts each photon into an electric current pulse. A lock-in device (I) extracts the laser induced fluorescence from the total signal. A PC (J) reads the lock-in and stores the data. An iodine absorption cell (K) is used to measure the well documented absorption lines of iodine. In this way, a wavelength calibration is obtained. Typical results of the DSLIF experiment consist of series of (x,y) points, where x value corresponds to the frequency shift and the y value to the laser induced fluorescence intensity.

The DSLIF technique as described above is able to resolve ion velocities according to the saturated absorption width of the used transition. For the previously described transitions it means than the spectral widths of the used lasers are small enough to excite velocity categories smaller than 1 ms^{-1}. For this a very low intensity must be used to avoid saturation effects. However, this also means that the laser induced fluorescence signal is low, due to the small number of particles which are in this category and are excited. When the high velocity resolution is not needed and the resolution can be in the order of 100 ms^{-1}, the saturated absorption width can be in the

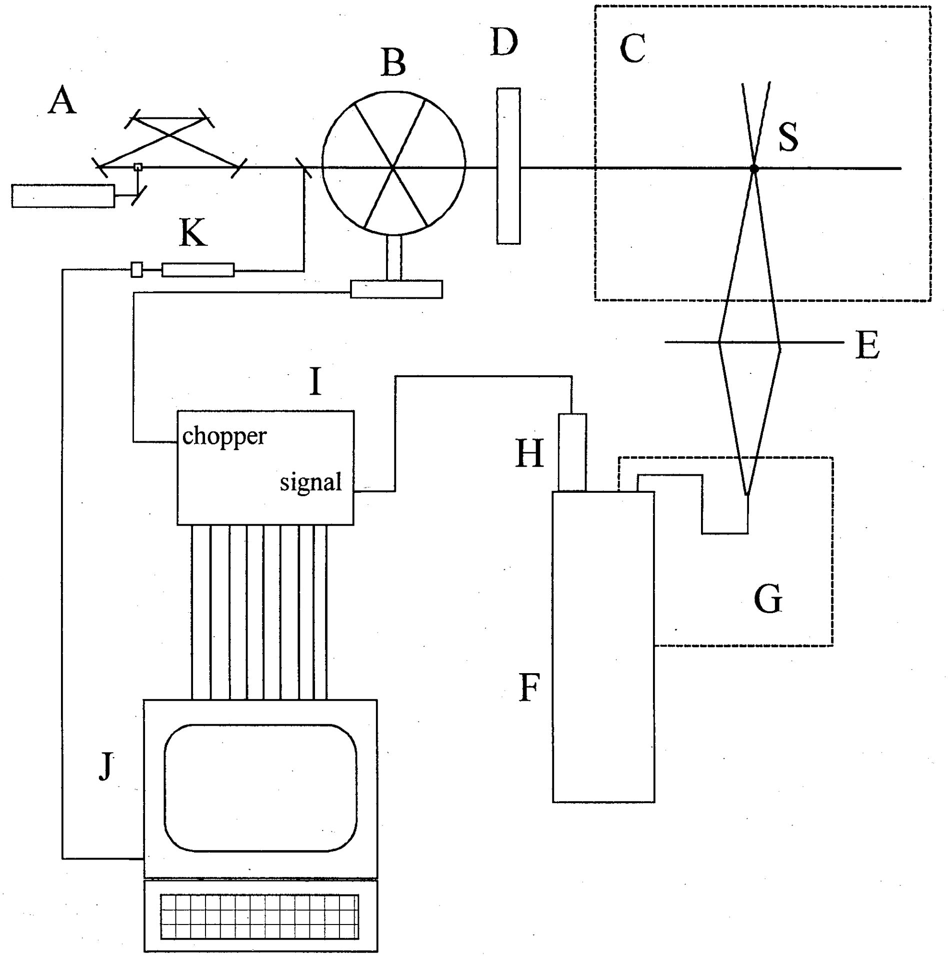

Figure 4.8 : Typical setup of the DSLIF experiment.

A	dye laser	D	beam shaper	G	optical fiber	J	PC
B	chopper	E	lens system	H	photomultiplier	K	iodine absorption cell
C	plasma chamber	F	monochromator	I	lock-in amplifier		

order of 160 MHz, which is much larger than the spectral laser width.
Consequently, the intensity of the laser may be much higher to saturate the transition. As a result, the LIF signal is also higher, which makes it possible to measure lower metastable densities than with low laser intensities.

References

[1] B. Pelissier and N. Sadeghi, Rev. Sci. Instrum. **67**, No. 10 (1996), pp3405-3410

[2] I. Langmuir and H. Mott-Smith, General Electric Rev. **27**, 449 (1924)

[3] F.F. Chen, Plasma Physics (J. Nucl. Energy C) 1965, Vol. 7, pp. 47-67

[4] J.E. Allen, R.L.F. Boyd and P. Reynolds : Proc. Phys. Soc. Lond. **70B**(1957), pp. 297

[5] H. Amemiya : Jap. J. Appl. Phys. Vol. 27, No. **4**, (1988), pp.694-695

[6] A. Brockhaus, C. Borchardt and J. Engemann : Plasma Sources Sci. Technol. **3** (1994) pp. 539-544

5. Characterization of the 450 kHz plasma reactor

5.1. Introduction

Low pressure radio frequency (RF) discharges are widely used in the plasma-based chemical processing industry. As an example, these plasmas are applied in the fabrication of integrated circuits because of their effective etching properties. Most research projects on etch plasmas examine the relations between the plasma parameters (like the densities and temperatures of various species and surface effects) and the external factors (like the gas pressure, mixture, and the applied power).

The frequency of the driving RF voltage has a large impact on the characteristics of the plasma. When the frequency is in the microwave region (GHz) the electrons and ions cannot travel a large distance during one period. The lighter electrons will absorb the major part of the power and will use this to make excitations and ionizations all over the plasma volume.

At intermediate frequencies, like the commonly used 13.56 MHz, the ions still cannot follow the field variations, but the electrons are able to travel a considerable distance.

At lower frequencies, the discharge is similar to DC situations. Electrons are accelerated in the electric field and are able to cross the reactor within times in the order of 10 ns. The ions reach the electrode with a large kinetic energy, because they are accelerated in the sheath. The energetic ion bombardment on the electrode surface produces secondary electrons. This process is controlled by the secondary emission coefficient γ, while the ionization in the glow is determined by the ionization coefficient α. The secondary electrons are accelerated in the sheath and travel through the plasma towards the other electrode with a large velocity. During their trajectory they lose energy by excitation and ionization processes. These high-velocity electrons are also called beam electrons. The number of beam electrons in the plasma is directly related to the number of electrons created at the electrodes. At these low frequency plasmas the discharge is sustained by the secondary electrons. This situation is named the γ- or beam-dominated regime, in contrast with the α-regime at higher frequencies where the electrons in the bulk sustain the plasma. The transition between these regimes depends on the applied power and on the frequency.

The ion transit frequency (ITF) is a characteristic frequency, which is determined by the time that ions need to cross the sheath. Below this frequency, the ions can cross the sheath in a time less than half a RF cycle. A typical value for the ITF of argon ions is 1 MHz.

To investigate the differences between the regimes, several studies have been carried out. Köhler[1] and Bruce[2] showed the influence of the frequency on the bombarding ion energy. For frequencies higher than the ITF, the energy of the ions at the wall is controlled by the time averaged electric field in the sheath region. For frequencies below the ITF, the ions reach the electrode within one RF period. Their energy is determined by the temporal value of the electric field on the moment that they enter the sheath region. Therefore, some ions reach the electrode with small kinetic energies. Others arrive with large energies, which can induce surface damage and lead to contamination of the plasma. In this case, the saddle-shaped ion energy profile[3] at the electrode is broad and can extend from zero energy up to the maximum electrode potential, while for frequencies above the ITF the profile is much narrower.

Flamm[4] and Donnelly[5] investigated the frequency effects on various parameters (emission and electrical, ion, and etching characteristics) in a 300 mTorr chlorine plasma. At 220 kHz they found two sharp peaks in the temporal emission profile, indicating electrons going to and from the electrode. The latter are created by the ejection of secondary electrons at the surface after ion bombardment. They also found a sharp decrease of the poly-silicon etch rate when increasing the applied frequency above about 1 MHz. This effect is a direct result of the simultaneous decrease of the maximum ion energy when going to the regime where the ions cannot cross the sheath within one RF period.

Ganguly[6] determined the 2D time resolved emission patterns of a 30 and 200 kHz helium discharge. At 200 kHz the emission is symmetric. The low frequency shows an asymmetric pattern for complementary phases, which corresponds to a DC discharge with an increasing and decreasing current.

Kakuta[7] investigated the effects of frequency on the sustaining voltage and on the spatio-temporal emission profile in a 1 Torr argon discharge. The sustaining voltage is high at low frequencies and low at high frequencies. This effect is caused by the transportation and subsequent loss of charged particles from the plasma to the electrodes by drift and diffusion, which is smaller for high frequencies. As a result, no high voltage is required to sustain the plasma. From the emission measurements it is shown that at frequencies below the ITF, the discharge is mainly sustained by the secondary electrons emitted from the electrodes, while at higher frequencies the plasma is sustained by the electrons reflected by the oscillating sheath.

In this chapter, a low frequency discharge is investigated. A 450 kHz RF voltage drives a capacitively coupled parallel plate plasma reactor filled with 21 Pa argon (see section 5.2). Several experimental techniques are applied to this reactor to characterize the plasma (section 5.3). Time and space resolved optical emission spectroscopy is used to determine the population of atomic and ionic states. From this, more insight is obtained in the various excitation mechanisms. The movement of the ions near the sheath edge is investigated by the determination of the time and space resolved ion velocity distribution function (IVDF) using Doppler shifted laser induced fluorescence (DSLIF). With a Langmuir probe, space resolved ion densities and electron temperatures are measured. IR laser absorption spectroscopy is used to measure the density and temperature of the metastable argon atoms. The plasma is described with a one dimensional fluid model (section 5.4) and the simulations are compared with the measurements (section 5.5).

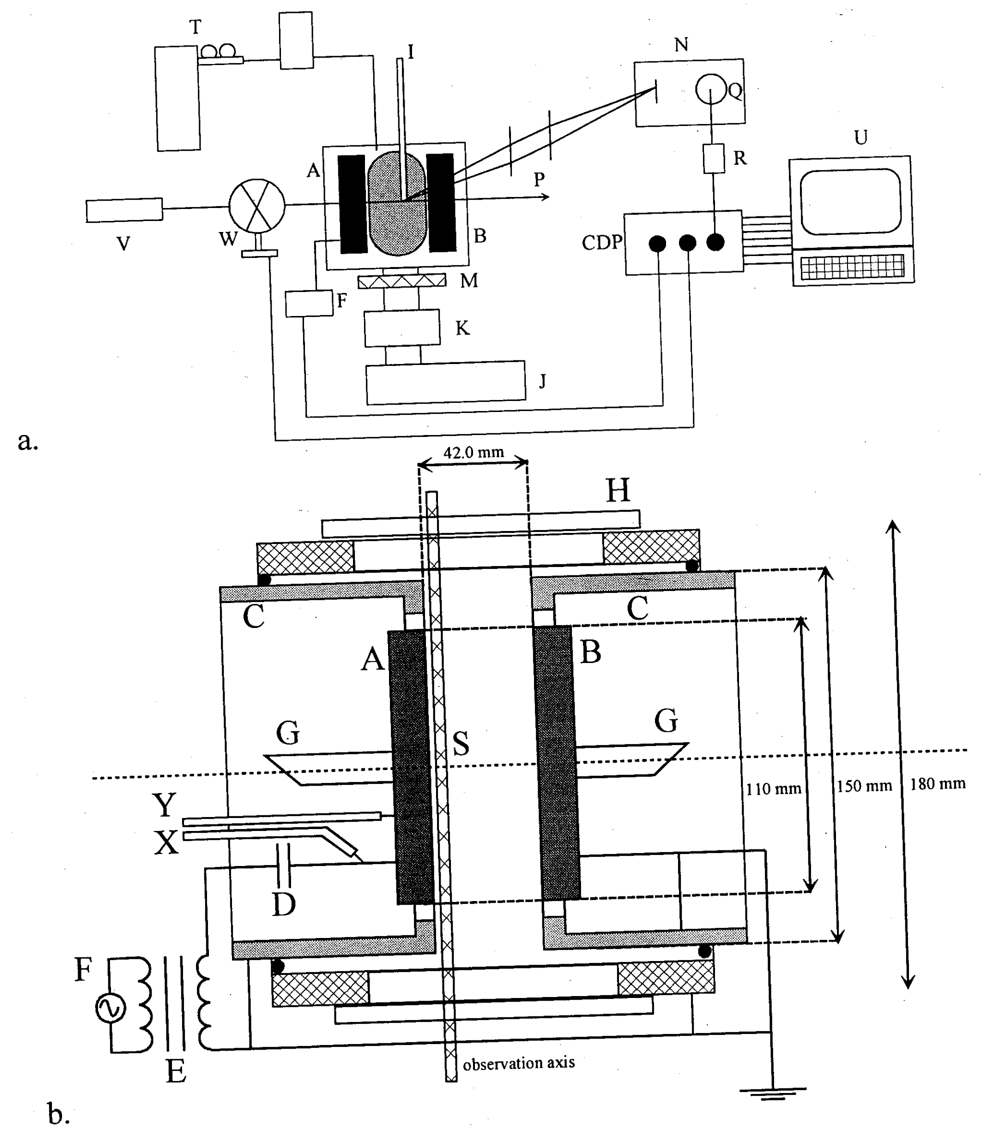

Figure 5.1 : Setup of the 450 kHz reactor. Part a. contains a global view of the total setup. Part b. shows a schematic close-up of the reactor.

A powered electrode
B grounded electrode
C grounded shields
D capacitor
E transformer
F 450 kHz source
G Brewster windows
H window
I Langmuir probe
J rotary pump
K turbo pump
L flow controller
M variable valve
N monochromator
P lenses
Q photomultiplier
R pulse shaper
S plasma
T gas bottle
U PC
V ring dye laser
W chopper
X current probe
Y voltage probe

The pressure is 21 Pa for all measurements. The pumping system consists of an Edwards dual mode 12 m^3h^{-1} rotary vacuum pump (J) and a Pfeifer 190 ls^{-1} turbo pump (K). The base pressure is $5 \cdot 10^{-3}$ Pa. The combination of a continuous gas flow (L) from a argon gas bottle (T) and a variable valve (M) to the vacuum pumps controls the pressure in the vessel.

The emission or fluorescence radiation from the plasma (S) is focused onto the entrance slit of a 60 cm Jobin Yvon monochromator (N). To achieve a 1:1 projection, two lenses (P) of f=15 cm are used. The reactor can be moved horizontally to make axial measurements. A Hamamatsu type R1617 photomultiplier (Q), placed at the exit slit of the monochromator, counts the incoming photons. Using an EMI 1182 pulse shaper (R), the photomultiplier pulses are transformed into TTL pulses. A home made[8] pulse counting system (CDP) measures the delay between the photon pulses and the period of the applied RF voltage. After a trigger pulse, generated by the 450 kHz source, the CDP starts counting from zero with the internal clock of 80 MHz (12.5 ns). Each time a photon pulse is received, the counter is read and the value is stored in the memory. The counter is reset to zero when another start pulse is received. With a PC (U) the values are read from the memory and the corresponding array elements or channels are increased by 1 count (see figure 5.4). The channel x corresponds to the time t between the trigger pulse and the photon pulse as $t = x \cdot 12.5\,\text{ns}$. The apparatus

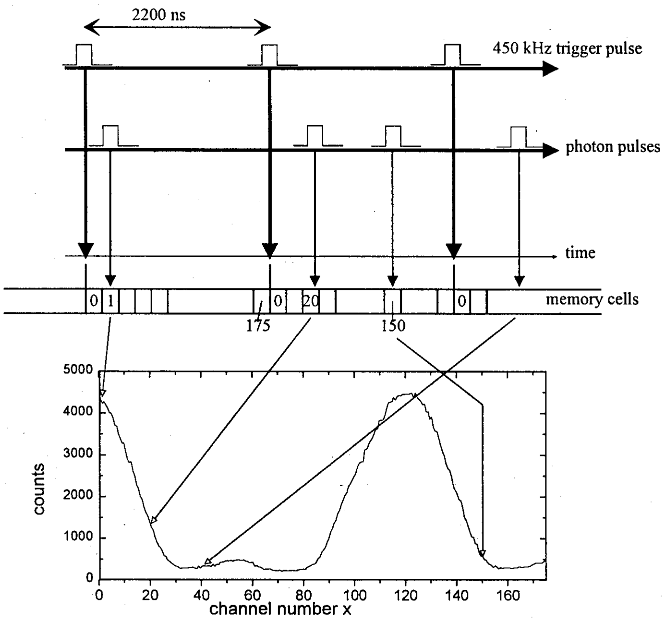

Figure 5.4 : Schematic presentation of the CDP operation. After a large number of counts the time resolved photon signal is obtained (bottom picture).

can collect all photon pulses up to a rate of $4.5 \cdot 10^5$ counts per second. When each channel has detected a sufficiently large number of photons (e.g. 1000 counts for a 3% statistical error), the obtained profile is a good representation of the time resolved photon signal.

In a different mode, the counter can be used as a lock-in device for measuring the time resolved laser induced fluorescence signal. In this situation the channel values are incremented when the laser beam, produced by a Spectra Physics 380D stabilized continuous wave (cw) ring dye laser (V), passes through the chopper (W) and the channel values are decremented during a period when the chopper blocks the laser beam. This operation extracts the laser induced fluorescence from the background emission.

5.3. Measurements

5.3.1. Langmuir probe

One of the most common instruments to measure the ion density and electron temperature is the Langmuir probe. Here, a double probe system is inserted into the plasma through an extension flange of the reactor. The setup is described in detail in

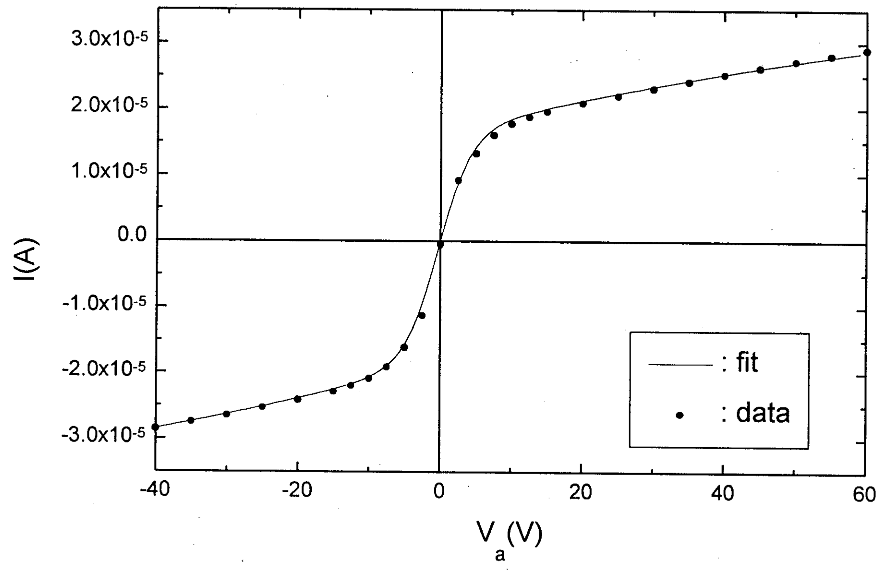

Figure 5.5 : Example of the measured and fitted double probe trace in the 21 Pa argon plasma at 18 W.

section 4.4.3. Both probe tips are made of tungsten wire of 300 μm diameter and are extended 3 mm from a metal shield covered with glass. The distance between the two tips is 2 mm. The 450 kHz pickup is filtered out of the probe signal with LC low-pass electronic filters. Consequently, less than 10 mV of the original RF signal is found after the filter. The probe system can be moved between the electrodes to obtain the spatial profiles (see figure 5.3).

The current I from one of the probe tips to the other is measured as a function of the applied voltage difference V_a between the two tips. An example of the resulting $I(V_a)$ characteristic is shown in figure 5.5. Several theories to interpret the measured $I(V_a)$ profiles can be found in section 4.4.2. In the double probe trace, at large V_a, the current is only determined by the ion density near the probe. The most negative probe tip only collects ions, while the other tip collects both ions and electrons. An increase in the applied voltage decreases the potential of the negative probe. The change in the collection of ions is minimal. As a result, the other probe can stay almost at the same potential. The resulting $I(V)$ characteristic at these high values of V_a is therefore quite flat. For small differential probe voltages, located around zero, the two probes collect both ions and electrons. A variation in the potential will result in a change in the electron current, while the ion current remains relatively constant. The $I(V_a)$ characteristic around zero potential shows therefore a large dependence on the applied voltage, determined by the energy distribution of the electrons. The electron temperature is deduced from this region by the calculation of the second derivative, see equation 4.23.

For each input set of values of the electron temperature T_e, the ion density n_i, and the plasma potential U_{plasma} the probe characteristic $I_x(V_x)$ for one of the probe tips (x=1,2) can be calculated from the exponential electron current (equation 4.11) and the ion current from Chen's curves (equation 4.13).

The double probe trace can be deduced from these single probe relations. For every double probe current value $I(V_a)$ the total current from probe 1 must be equal to the total current to probe 2 :

$$I(V_a) = I_1\left(V_1 - U_{plasma}\right) = -I_2\left(V_2 - U_{plasma}\right), \qquad 5.1$$

with $V_a = V_2 - V_1$. The small differences in probe area are taken into account. Using the measured electron temperature, the calculated double probe trace is fitted to the measured $I(V_a)$ characteristic by varying the ion density and the plasma potential. A typical fit is shown in figure 5.5.

Figure 5.6 shows the spatial profile of the obtained ion density for two values of the applied power. Also the results of the 1D fluid model, described later in section 5.4, are shown. Close to the electrode, from z = 0 - 10 mm, a drop in the ion density is observed, due to the acceleration of the ions inside the sheath. Due to the method of obtaining the spatial dependence (see figure 5.3), the two probe tips are only at the same z value when placed in the middle of the plasma. In the off-center position the probe does not measure the real local plasma parameters. The separation of the probe tips is shown in figure 5.6 by the horizontal error bars.

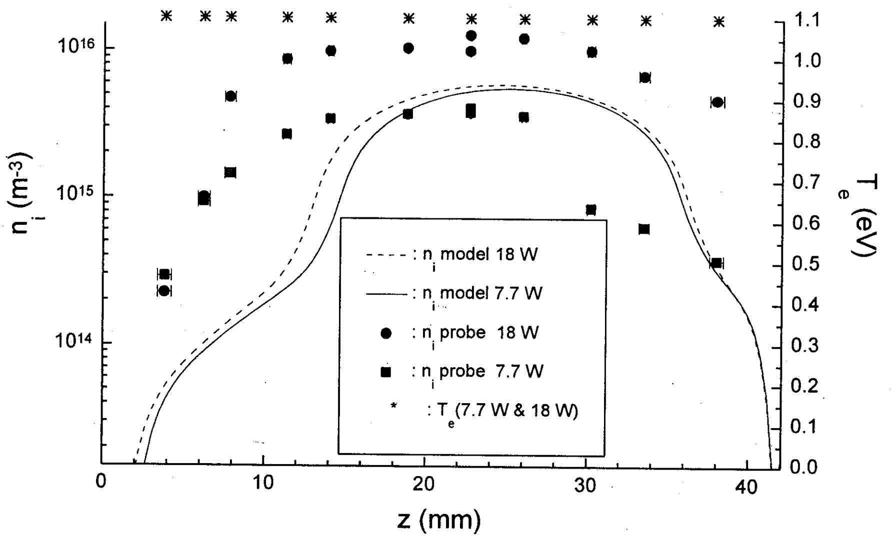

Figure 5.6 : Ion densities measured with Langmuir probe in a 18 W and 7.7 W plasma. The full and dashed lines represent the results from the 1D fluid model, described in section 5.4. z = 0 is the position of the powered electrode. The horizontal error bars refer to the spatial separation of the two probe tips. The asterix represents the electron temperature, which is 1.1 eV for both applied powers.

In figure 5.6 also the electron temperature is plotted. The measured values have no axial dependence and for both powers 1.1 eV is obtained.

The interpretation of the probe traces assumes that the plasma is stationary, i.e. the ion density and electron temperature do not (or slightly) change during the RF period. In this 450 kHz plasma however, these assumptions do not automatically hold. During the time between two cathodic phases of the powered electrode, the electrons could for instance lose their energy in collisions and ambipolar diffusion can decrease the density of charged particles.

The time variations in the ion density and electron temperature are determined by looking at the various loss processes.

The ambipolar diffusion coefficient D_a is typically in the order of 437 cm^{2}s^{-1} at 21 Pa[9]. The time constant τ for particle loss by ambipolar diffusion is given by (see equation 2.26) :

$$\frac{1}{\tau}=\frac{D_a}{\Lambda^2}, \qquad 5.2$$

with Λ the diffusion length. In first approximation, the diffusion length in a cylindrical plasma chamber with the electrode distance d much smaller than its radius, is $\Lambda = d/\pi$[10]. Using d=42 mm, τ = 4 ms, which is much larger than the RF period of 2.2 μs. Also the rate coefficients for radiative and 3-body recombination (R = $3\cdot10^{-19}$m^{3}s^{-1} and R = $9\cdot10^{-23}$m^{3}s^{-1}, respectively for T_e = 1 eV and n_i = 10^{16} m^{-3}, see appendix A) are too low and these loss process can be neglected.

It can therefore be concluded that the ion density in the plasma glow is constant during one RF period. In the sheath region however, the situation is different. There, the electrons will be pushed away from the electrode during its cathodic phase, while the ions are attracted. As a result, the probe theory may not be applied in the sheath region and the results are not an image of the real local ion density.

The electrons lose their energy in collisions, resulting in a decrease of the electron temperature. To estimate this loss, the number of collisions to leave an electron with 1/e of its initial energy E_e^0 is calculated. The energy after N elastic collisions is $E_e^0(1-2m_e/M)^N$, which leads to :

$$E_e^0\left(1-\frac{2m_e}{M}\right)^N = E_e^0\frac{1}{e}. \qquad 5.3$$

When the mass m_e of the electron and M of the argon atom are used, $N = 37\cdot10^3$ collisions. The cross-section for elastic collisions of electrons with atoms is in the order of 10 Å^2, see appendix A. According to equation 2.31 the collision frequency for 1.1 eV electrons is then $3.6\cdot10^8$ s^{-1}. It therefore takes 100 μs to lose 1/e of its energy. In other words, in 2.2 μs an electron makes just 792 collisions and loses only 2% of its energy.

Therefore it can be concluded that also the temperature of the low energy electrons remains fairly constant in time. The high energetic beam electrons however, are lost to the walls and the production varies with the ion energy at the electrode surface, determined by the electrode voltage. Hence, the density of these electrons changes during the period.

The resulting electron energy distribution consists of a low energy part, which is Maxwellian and has a minor time dependence, and a high energy beam electron tail of which the density varies during the RF period. The measured electron temperature is obtained at the origin of the probe trace, where the dependence of the current on the probe voltage is determined by the low energy electron distribution. Therefore, the measured T_e only represents the slow, bulk electrons.

5.3.2. IR laser absorption spectroscopy

With a tunable infrared diode laser, the density of the metastable argon $1s_5$ atom level is determined from the absorption profile of the 772.376 nm transition ($1s_5 \rightarrow 2p_7$, in Paschen notation) and of the metastable $1s_3$ level from the 772.421 nm transition

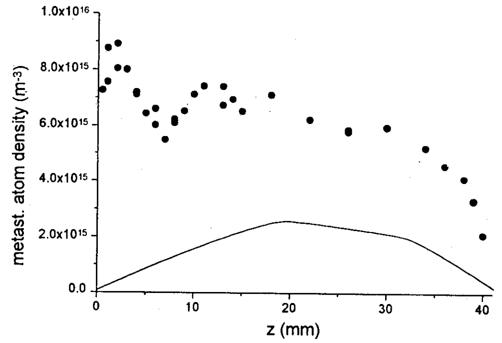

a.

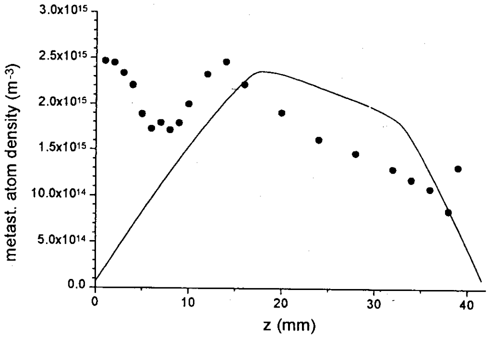

b.

Figure 5.7 : Metastable density distribution (•) for 18 W (a) and 7.7 W (b) applied power. In both figures also the results of the 1D fluid model, described in section 5.4, are shown (lines).

($1s_3 \rightarrow 2p_2$), see appendix A. The laser beam crosses the reactor parallel to the electrodes along the radial direction at various distances *z* to obtain the spatial variation of the absorption.

The measurement and interpretation of the absorption profiles with IR laser absorption is described in section 4.3.

From the width of the absorption profiles the neutral gas temperature is obtained. For both powers it is measured to be 300 K with no spatial dependence.

Figure 5.7 shows the metastable densities (dots) for 18 W (a) and 7.7 W (b) applied power. Also the results from the 1D model (described in section 5.4) are plotted (lines). The shown results are for the $1s_5$ level. The $1s_3$ level measurements show densities which are 5 times lower, as can be expected from the difference in the degeneracy of the two levels. The temperatures as obtained from the two metastable levels are the same.

There is a clear maximum in the metastable atom density close to the electrode, which is larger for the higher power, indicating an increased production of metastables. This phenomenon is not likely to be a result of an enhanced electron impact excitation from the ground state, because in the sheath region (which stretches out from approximately z = 1 cm up to the electrode surface) the electron density decreases. Phelps and Jelenkovic[11] reported the possibility of excitations by collisions of argon atoms with fast ions and neutrals. The fast neutrals are created in charge-exchange collisions of fast ions with stationary atoms in the vicinity of the electrode. This process leaves a slow ion and an highly energetic (10 - 200 eV) neutral. The fast neutrals and ions are able to excite one or some atoms from the ground state to the excited states, including the metastable levels. They found that this process occurs mainly at high ratios of the electric field over the gas density (above a few kTd, where 1 Td = 10^{-21} Vm^2).
In this plasma, the electric field in the sheath increases from a few Vcm^{-1} to more than 1 $kVcm^{-1}$. Hence, the creation of metastable atoms increases when going through the sheath towards the electrode. A typically value for the electric field is 1.5 $kVcm^{-1}$. At 21 Pa, the corresponding value for E/N_g is 30 kTd. According to Phelps et al.[11] the cross-section of charge exchange reactions between argon ions and neutrals is in the order of 50 $Å^2$. Therefore, each 0.4 mm a fast atom is produced. As a rough estimate, one ion makes 20 fast atoms while crossing the sheath. Taking the electric field into account, the fast atom will have an energy equal to the energy gain of the ion during its 0.4 mm travel. Therefore, the initial energy of the fast atoms will be approximately 60 eV. In the paper of Phelps and Jelenkovic[11], the cross sections for fast argon ion and atom collisions with stationary argon atoms are given for various processes. It can be seen that the dominant processes for the ion are charge exchange and excitation, and for the fast atom momentum transfer and excitation. Although little is known about the cross-sections for excitation, they are in the order of 0.1 - 1 $Å^2$ at these kinetic energies. This corresponds to a production rate of metastable atoms by 60 eV atoms or ions which is in the order of 10^{-16} m^3s^{-1}. The density of metastables is enhanced by cascade radiation from higher levels, populated by the same process.
When compared to the rate coefficient for excitation in the plasma, which is smaller than 10^{-18} m^3s^{-1} for this situation (see appendix A) and taking into account the density of fast atoms, which is higher than of the ions, the creation of metastable atoms by fast atoms is likely to play only a role close to the electrode.
The effect of the fast ions and neutrals is also observed in the emission results of section 5.3.4.

5.3.3. Doppler shifted laser induced fluorescence (DSLIF)

To determine the local velocity distribution function of the argon ions, Doppler shifted laser induced fluorescence (DSLIF) is used. An extensive description of the DSLIF technique can be found in section 4.5. Metastable $3d'^2G_{9/2}$ argon ions are pumped to the $4p'^2F_{7/2}$ level with 611 nm laser light. The 461 nm fluorescence from the upper level is used as a measure for the density of the metastable level. According to the Doppler effect, the metastable ions only make a transition when their velocity component in the direction of the laser beam fits the Doppler shifted laser frequency. By scanning the laser around the absorption line, the velocity distribution function (VDF) of the metastable ion is obtained.

The stabilized dye laser has a spectral width which is less than 0.5 MHz. After going through an optical chopper, operated at 300 Hz, the beam enters the plasma chamber. Reflections are minimized by using a Brewster window at the exit slit of the reactor. The detection system is positioned perpendicular to the laser beam and fixes the observation point in the plasma.

The CDP is used in the lock-in mode to separate the DSLIF signal from the background emission light. In this way, the time resolved DSLIF signal is obtained.

Moving the reactor parallel to the laser direction enables measurement of the spatial dependence.

In optimum conditions the DSLIF signal is 1% of the total measured 461 nm emission signal. Therefore, long measurement times are necessary to obtain a low statistical error. A wavelength calibration is obtained from the absorption response of an iodine cell, using known absorption frequencies[12].

Before entering the vacuum vessel the laser beam is expanded to 11 mm in the direction parallel to the optical axis of the detection system. This results in a larger laser volume and therefore a larger LIF signal. Also the intensity is decreased in this way, avoiding saturation effects. The laser power in the plasma is approximately 10 mW in 20 mm^2. At this intensity the saturated absorption width ($\approx$ 70 MHz) is much smaller than the Doppler width of 1GHz (300 K argon). As a result, the measured DSLIF profile is a good representative of the velocity distribution function of the metastable ions (see section 2.5).

In figure 5.8 the time dependent DSLIF signal is compared with the 461 nm emission signal at the same position (z=8 mm) and for the same applied power (18 W). The applied voltage on the powered electrode is shown in figure 5.2c. Clearly a different time profile is observed, which is caused by the lifetimes of the two levels involved. For the 461.0 nm emission, the upper level ($4p'^2F_{7/2}$) has a lifetime of 8.5 ns (see appendix A). This is much shorter than the RF period and as a result, the density of this level can be considered as an image of the excitation profile, see section 4.2.

Regarding the DSLIF measurements, the lifetime of the metastable $4s'^2D_{5/2}$ level is much larger. As a first approximation, it can be seen from figure 5.8 that the lifetime of the metastable level must be in the order of 250 ns. Application of equation 4.3 with τ = 250 ns to determine the metastable density from the excitation profile shows a perfect fit with the measured metastable ion density as obtained with DSLIF[8]. Ambipolar diffusion and recombination are too slow to explain the life time of the metastable ion, as already has been shown in section 5.3.1. However, unlike ground state ions, metastable ions are quenched when making collisions :

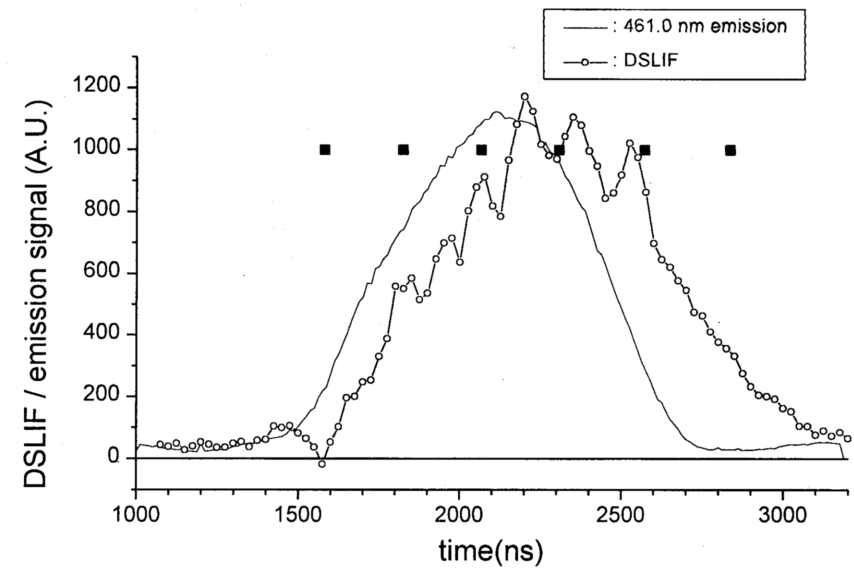

Figure 5.8 : Time dependent DSLIF and emission intensity at z=8 mm from electrode. The black squares refer to the times in figure 5.9.

$Ar^m + Ar \rightarrow Ar^* + Ar^*$.

The reaction product Ar* can be the ground state, an excited atom state, or the ion ground state.

Due to the acceleration of the ions towards the electrode, the velocity in the *z*-direction is increased. This results in a higher quenching rate and the corresponding lifetime decreases.

Figure 5.9 shows the time dependent DSLIF signal at various moments in the RF period (see also figure 5.8), for two positions at 18 W. A negative frequency shift indicates a velocity component towards the powered electrode. A clear time dependence is again seen in the DSLIF signal, due to the density variations of the metastable level and the varying excitation rate by the secondary electrons.

The position $z = 9$ mm from the powered electrode is always inside the glow region. A symmetric profile is shown with no average directed speed. At $z = 8$ mm, the measurement point is during some part of the RF cycle inside the sheath region. Clearly a shift to higher velocities towards the electrode can be seen. This is confirmed by the experiment where the laser is guided through the plasma in the opposite direction. Then, the same shift, but to the other direction is observed.

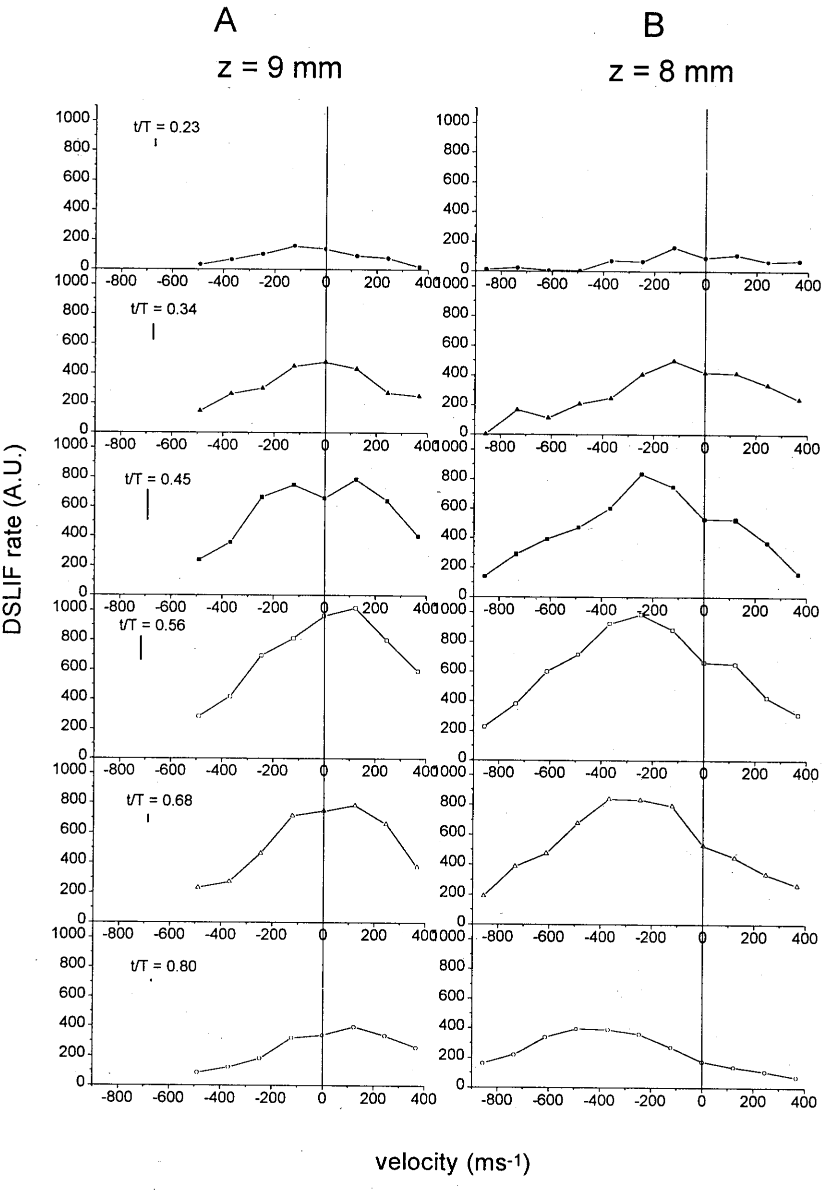

Figure 5.9: DSLIF results for various times *t* in the RF period *T* at two distances from the powered electrode : z = 9 mm (A) and z = 8 mm (B). The observation moments are displayed in figure 5.6. The error bars for each time are shown under the t/T values.

It is also shown in the figure that later in the period the frequency shift is larger, which indicates an increasing velocity. At $z = 8$ mm the velocity in the z-direction increases to approximately 0.5 $\mathrm{kms^{-1}}$ later in the period. When the observation point moves further inside the sheath region, the density of metastable ions drops and the DSLIF signal is too weak to be measured. Because the lifetime of the upper level is much shorter than of the metastable level, the background emission is decreasing faster than the LIF signal (see figure 5.8), resulting in a less noisy signal later in the period. The ratio between the DSLIF signal and the background emission is higher, which causes better statistics. The size of the error bars, shown in figure 5.9, depend therefore on the time in the period. If N counts are detected per channel, the noise per channel is $N^{1/2}$. When the assumption is made that the number of LIF photons is much smaller than the number of emission photons, the noise in the DSLIF signal is $(2N)^{1/2}$.

According to the theory of chapter 3, the collisional presheath length is typically in the order of the mean free path of the ions. Using the previously calculated collision frequency for quenching of 2.2 MHz, the mean free path of the metastable ions is approximately 0.2 mm at these velocities. It is therefore not possible to resolve the acceleration inside the presheath, because of the 0.5 mm spatial resolution of the measurement. At the edge of the presheath, the ions are accelerated to the Bohm velocity of 1.6 $\mathrm{kms^{-1}}$. This velocity corresponds to a kinetic energy of the ions of $1/2kT_e$. Because $T_e \gg T_i$, the velocity in the presheath exceeds several Doppler widths. Unfortunately, at this velocity the metastable density is already too low to measure the DSLIF signal.

The short mean free path of the metastable ions assures that the measured signal originates from metastables which are created locally. During the cathodic part of the powered electrode, the sheath stretches out up to 8 mm in the plasma. Only then are the newly created metastable ions being sufficiently accelerated in the electric field to observe an velocity shift. Because the life time and their corresponding mean free path is short, the acceleration of the metastable ions occurs within the detection volume. Hence, only during the last three observation moments of figure 5.9 the acceleration is observed. In the last plots it can be seen that the distribution function has a tail to higher velocities.

The excitation to the metastable ion level is mainly from the ground state atom level by the beam electrons. Therefore the metastable ion velocity distribution function is not an image of the velocity distribution of the ground state ions. The metastables have a shorter life time due to the quenching by collisions with electrons and atoms. The ground state ions, however, are not lost in collisions and they can survive multiple RF periods.

5.3.4. Optical emission spectroscopy

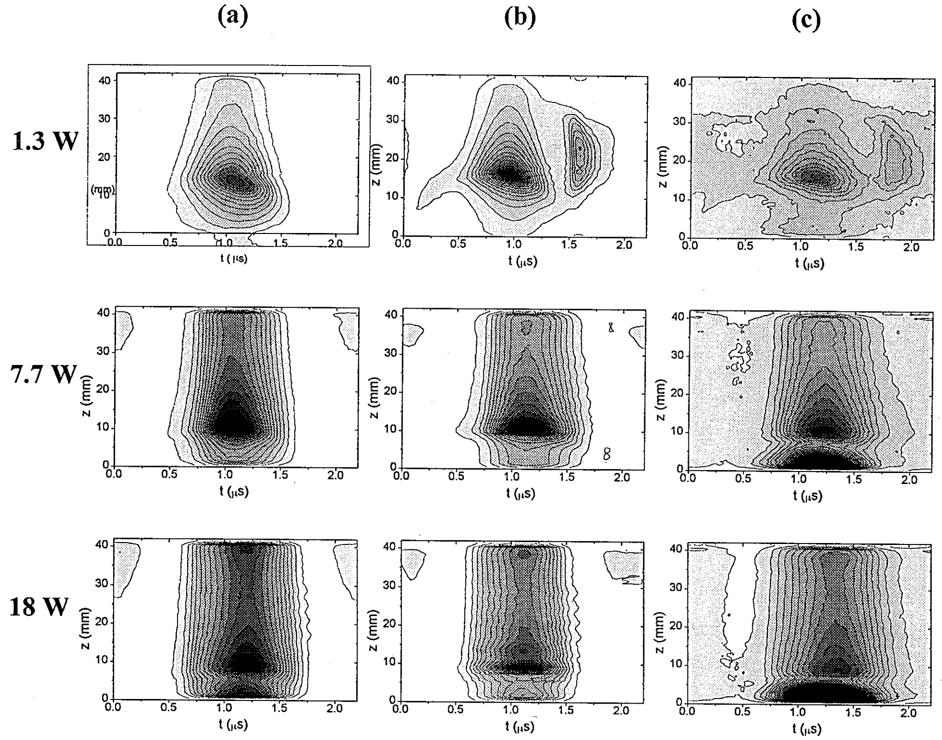

Figure 5.10 : Measured time and space resolved emission profiles for the 461.0 nm (a) ionic and the 750.4 nm (b) and 800.6 nm (c) atomic lines for three applied power levels.

Observation of the emission light from a plasma provides information about the various excitation mechanisms in the plasma. The population of the energy levels is determined by the possible excitation channels and their corresponding cross-sections. For this plasma both ionic and atomic argon lines are investigated. The setup of this experiment is described in section 4.2. A monochromator is used to distinguish between the contribution of the various lines. At each z-position the time resolved emission signal is obtained with the CDP photon counter (see section 5.2). Although the slit width of the monochromator is set at 0.4 mm, the spatial resolution of the experiment is determined by the 1 mm distance between two consecutive measurements. All measured profiles from $z = 0$ - 42 mm are combined and placed in an array which contains the spatio-temporal emission profile.

These profiles are shown in figure 5.10. The left column (a) shows the time and space dependence of the 461.0 nm argon ion line ($4p'^2F_{7/2} \rightarrow 4s'^2D_{5/2}$). The central column

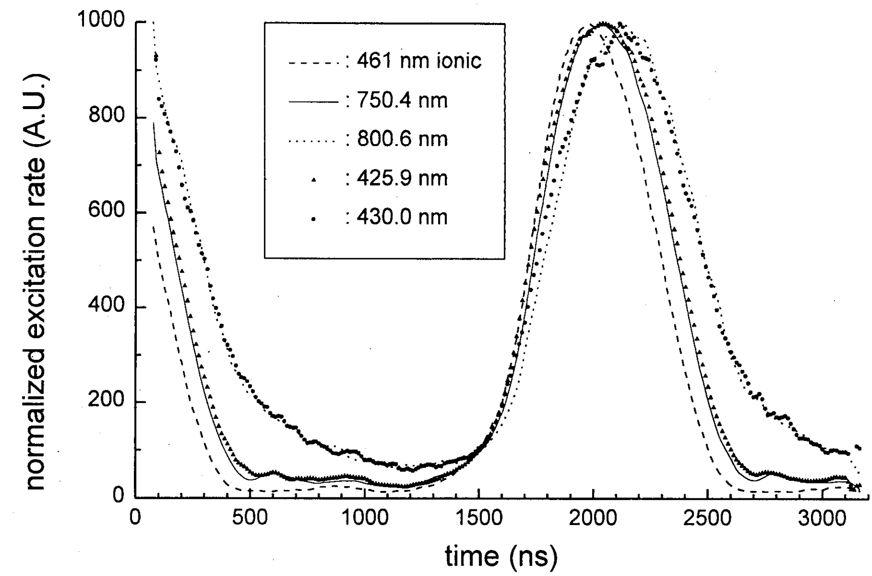

Figure 5.11 : Time dependent excitation rates of various lines at z=10 mm from the powered electrode at 7.7 W applied power.

(b) shows the emission profile of the 750.4 nm line ($2p_1 \rightarrow 1s_2$) of the argon atom. The right column (c) shows the atomic 800.6 nm emission line ($2p_6 \rightarrow 1s_4$). A strong time dependence can be seen for all lines, originating from the time dependent excitation rate from the energetic secondary electron beam during the cathodic phase of the powered electrode. Due to the smaller powered electrode area than grounded area, the voltage over the sheath in front of the powered electrode is much larger than for the sheath at the grounded electrode. Therefore also the beam electrons are much more energetic when the powered electrode is in the cathodic phase, giving rise to a much larger emission intensity during this time in the period than during the anodic phase.

The emission profiles are proportional to the density of the upper levels. According to the theory of section 4.2, the lifetime of the upper level determines the shift between the excitation rate to the upper level and its density. When equation 4.2 is used, the excitation rates can be expressed as a function of time.

In figure 5.11 the time dependent excitation profiles for various line at position $z = 10$ mm, which is always in the negative glow region, are shown. The excitation to the $2p_1$ (750.4 nm), $2p_6$ (800.6 nm), $3p_8$ (430.0 nm) and $3p_1$ (425.9 nm) atom levels, and to the $4p'^2F_{7/2}$ (461.0 nm) ion level are compared. Although the emission profiles are different, the excitation rates show a clear resemblance for certain lines. The ion level needs 21.1 eV to be excited from the ground state ion level and 36.9 eV for excitation from the ground state atom. Therefore, when the electric field decreases and the beam electrons become less energetic, the excitation to this level also decreases. The population of the 2p and 3p levels from the ground state atom level needs between 13 and 15 eV, which is much lower. Therefore, the electrons will be able to populate these levels for a longer time than for the ionic level, which can be seen in figure 5.11 by a slower decay than for the 461 nm curve.

The $2p_6$ (800.6 nm) and $3p_8$ (430.0 nm) lines however, show an even larger decay time than the other two atomic levels. This can be explained by taking a closer look at the possible excitation from the metastable atom level ($1s_5$). Excitation from this level requires only 1.62 eV and 2.96 eV respectively, which is much lower than what is needed for the excitation from the ground state. The excitation from the metastable level can therefore be performed by the (less energetic) bulk electrons and as a result, the excitation rate does not go to zero in figure 5.11 for these levels. For the $2p_1$ and $3p_1$ levels the cross-sections for electron impact excitation are much smaller than for the $2p_6$ and $3p_8$ levels. These cross-sections seem to follow the quantum rules for dipole transitions, with the rule for the J quantum number in particular : $\Delta J = \pm 1,0$ but not $0 \rightarrow 0$. The metastable $1s_3$ level has $J = 0$ and the $1s_5$ level has $J = 2$. The $2p_1$ and $3p_1$ levels, responsible for the 750.4 nm and 425.9 nm emission, have $J = 0$ and the transition to this level from one of the metastable levels is therefore forbidden. The cross-section for the electronic excitation from these levels is below 0.2 $Å^2$ and decreases rapidly for increasing electron energy[13]. The optically allowed transitions from the metastable $1s_5$ to the $2p_6$ ($J = 2 \rightarrow 2$) and $3p_8$ ($J = 2 \rightarrow 2$) levels have much larger excitation cross-sections of approximately 10 $Å^2$ and remain fairly constant for increasing electron energies up to 15 eV[13]. As a result, these levels can be much more efficiently populated from the $1s_5$ metastable level. The lifetime of the metastable levels is determined by the cross-sections of the quenching reactions. At this pressure, the lifetime is larger than the period (2200 ns) of the RF frequency. Hence, even when the beam is not present the $2p_6$ and $3p_8$ levels are still populated.

In figure 5.10 a difference between the 750.4 nm and 800.6 nm emission is also seen near the powered electrode, when it is in the cathodic phase. Again this difference cannot be caused by the differences in the electronic excitation, because the density of bulk electrons is very low inside the sheath. Excitation by beam electrons is possible, but the excitation from the ground or metastable state can not be responsible for the large difference between the emission intensity at the electrode and in the plasma. As mentioned before in section 5.3.2 and in the work of Phelps and Jelenkovic[11], excited states are created by collisions of fast neutrals and ions with stationary argon atoms. The fast neutral particles are produced by charge-exchange collisions of high energetic ions with stationary atoms. The enhanced emission effect is large near the powered electrode, where the ions are accelerated in the sheath. This effect is directly related to the ratio of the electric field and the gas density E/N_g. This factor increases when going closer to the electrode, resulting in a larger excitation rate by this process.

It can be seen that the population of the $2p_1$ level is much less efficient than the population of the $2p_8$ level. Consequently the cross-sections for these processes must be different, as they are for the electron impact excitation from the metastable levels (figure 5.11).

The additional feature in figure 5.10 at low powers is a small discharge appearing in one of the pumping tubes.

5.4. 1 dimensional fluid model

A one dimensional fluid model describes the transport of particles inside the discharge. The model is self-consistent. The electric field and particle densities are derived simultaneously. The model is similar to the one described previously by others[14,15]. For the low frequency, the plasma is mainly sustained by the secondary electrons emitted from the electrodes. To incorporate the influence of these beam electrons, three kinds of charged particles (fast electrons, slow electrons and positive ions) are assumed. Also neutral particles (excited and metastable atoms) are taken into account. The set of equations is formed by particle and momentum balance.

For the slow electrons :

$$\frac{\partial N_e}{\partial t}+\frac{\partial(N_e \mathbf{v}_e)}{\partial z}=S_e \qquad 5.4$$

$$N_e \mathbf{v}_e = N_e \mu_e \mathbf{E}-\frac{\partial}{\partial z}(D_e N_e) \qquad 5.5$$

and the ions :

$$\frac{\partial N_i}{\partial t}+\frac{\partial(N_i \mathbf{v}_i)}{\partial z}=S_i \qquad 5.6$$

$$N_i \mathbf{v}_i = N_i \mu_i \mathbf{E}-\frac{\partial}{\partial z}(D_i N_i)\,, \qquad 5.7$$

where N, $\mathbf{v}$, S and $\mathbf{E}$ are respectively the number density, the mean velocity, the source term and the electric field (only in the z-direction). The subscript i is related to the ion, e is related to the electron. The parameters μ and D represent the mobility and diffusion of the particle. The values of these quantities for argon are taken from the literature[16].

For the fast electrons, the following equations are used :

$$\frac{\partial N_{beam}\overline{\mathbf{v}}_{beam}}{\partial z}=S_{beam} \qquad 5.8$$

$$\frac{\partial \varepsilon_{beam}}{\partial z}=eE-L_{beam}\,. \qquad 5.9$$

ε_{beam} is the energy of the beam electrons, L_{beam} is the loss term for the beam electrons, which can be inelastic collision or a transition from a fast electron to a slow one. An electron from the beam (fast) becomes bulk electron (slow) when its energy is lower than the ionization threshold energy. To calculate the particle densities, the so called exponential scheme[17,18] is used. This method assumes a constant flux between two consecutive grid points. The advantage of this scheme is that large variations in the particle density, appearing in the sheath, can be solved more accurately than with other methods.

The electric field is obtained by:

$$\frac{dE(z)}{dz}=\frac{e}{\varepsilon_0}\left[N_i(z)-N_e(z)-N_{beam_1}(z)-N_{beam_2}(z)\right], \tag{5.10}$$

where the indexes 1 and 2 refer to the left and the right electrode.

For neutral particles the equations used are similar to equation 5.4 and 5.5 with the appropriate diffusion coefficient but no mobility. The source term for the excited atoms arises from the excitation of ground state atoms by electrons.

The space-time evolution of two excited level of argon ($2p_1$) and ($2p_6$) are followed. The values for the excitation rates from the ground state to these two levels are taken from Chutjian[19] and Padial[20].

The effect of metastable atoms in ionization is included in the model following the rate coefficients given by Tochikubo[21].

In figure 5.6 the measured ion density is compared with the results from the fluid model. One can see that the shape of the curve resembles the measurement, while the absolute values differ. This can be explained by the large uncertainty in the cross-section for the ionization and the secondary emission coefficient γ, which depends on the electrode surface material. The latter can easily change a factor of 2 depending on the condition of the surface (clean / oxidized / contaminated).

Figure 5.7 shows the calculated metastable density together with results from the IR laser absorption experiment. Here the two curves are in good agreement, except for the density close to the electrode. As explained before, this feature is caused by the production of metastable atoms by fast neutrals and ions with atoms, which is not taken into account in the simulation. The absolute values of the metastable density depend on the cross-sections for quenching and on the excitation rate. The latter is determined by the electron density. Because it is under-estimated, also the calculated metastable density will be lower than the measurement. Also the excitation rate to the metastable levels by the beam electrons depends directly on the secondary emission coefficient γ, which is not exactly known.

In figure 5.12 the calculated population of the $2p_1$ and $2p_6$ levels are presented at the three power levels. The strong time dependence of the signal is produced by the high energetic beam electrons. The beam electrons from the powered electrode have a higher energy because there is negative bias voltage due to the size of this electrode, which is smaller than the area of the grounded parts in contact with the plasma. Within the error of the measurement, the plots show a good resemblance with the emission results of figure 5.10, although the enhanced 800.6 nm emission near the electrode is missing. As seen before, this is caused by the population of excited states, due to the collisions of argon atoms with fast atoms and ions. The model does not take these reactions into account.

which forbid the excitation to the $2p_1$ and $3p_1$ levels from the metastable level.

In the 800.6 nm ($2p_6 \rightarrow 1s_4$) emission profile a clear maximum is observed near the electrode during the cathodic phase of the powered electrode. Again this difference is caused by the population of excited states by collisions of fast atoms and ions with neutrals. This maximum is not seen in the 750.4 nm ($2p_1 \rightarrow 1s_2$) emission profile. Analogous to electronic excitation, the cross-sections for production of 2p levels from the ground state level by fast ions and neutrals seem to depend on the state. Apparently, for the $2p_6$ level, the cross-section for this process is much larger than for the $2p_1$ level.

The time effects in the emission intensity profiles are well predicted by the 1D fluid model, although the model does not predict the maximum near the electrode. The process of production of metastables by fast atoms and ions is not taken into account in the model.

With Doppler shifted laser induced fluorescence (DSLIF) the time and space resolved velocity distribution function (VDF) of the metastable ions is measured. For 18 W applied power, at 9 mm and 8 mm from the powered electrode, the initial acceleration of the metastable ions from the glow into the sheath is observed. At 9 mm the detection point is always inside the negative glow region, while at 8 mm the sheath stretches out to this position during the most cathodic phase of the powered electrode. Only then the metastable ions are accelerated. Due to the limited spatial resolution (0.5 mm) it is not possible to resolve the acceleration inside the presheath. The size of the presheath is limited by the mean free path of the ions, which is 0.2 mm at this pressure. Because the metastable ions are quenched in collisions, the short mean free path ensures that they are created and accelerated in (or very close to) their observation volume. At this position a maximum velocity of 0.5 kms^{-1} is found. When moving closer to the electrode, the acceleration of the ions causes a sharp decrease in the ion density, which makes the DSLIF signal too weak to measure.

The metastable ion VDF is not a direct image of the ground state ion VDF, because during the cathodic phase of the powered electrode the metastable ions are produced by beam electron excitation from the ground state atom level. Due to collisions, metastable ions lose their state and are quenched. The ground state ions, however, can have collisions without changing state. Consequently they survive multiple RF periods before they arrive at the electrode.

References

[1] K. Köhler, D.E. Horne, and J.W. Coburn, J. Appl. Phys. **58** (1985), pp3350

[2] R.H. Bruce, J. Appl. Phys. **52** (1981), pp7064

[3] R.J.M.M. Snijkers, "The sheath of an RF plasma : measurements and simulations of the ion energy distribution", thesis Technische Universiteit Eindhoven (1993)

[4] D.L. Flamm and V.M. Donnelly, J. Appl. Phys. **59** (1986), pp1052.

[5] V.M. Donnelly, D.L. Flamm, and R.H. Bruce, J. Appl. Phys. **58** (1985), pp2135

[6] B.N. Ganguly and A. Garscadden, IEEE transactions on plasma science **24** (1996),

pp115

[7] S. Kakuta, T. Makabe and F. Tochikubo, J. Appl. Phys. **74** (1993), 4907

[8] B. Pelissier and N. Sadeghi, Rev. Sci. Instrum. **67** (1996), pp3405

[9] M.A. Biondi, Phys. Rev. **93** (1954), pp1136

[10] E.W. McDaniel : Collision phenomena in ionized gases, John Wiley & Sons Inc., 1964

[11] A.V.Phelps and B.M. Jelenkovic, Phys. Rev. A. volume **38**, number 6 (1988), pp 2975-2990

[12] "Atlas du Spectre d'Absorption de la Molecule d'Iode - 14800-20000 cm^{-1}" : S. Gerstenkorn & P. Luc; Editions du Centre National de Recherche Scientifique CNRS (1978).

[13] C.C. Lin, GEC conference 1996

[14] Ph. Belenguer and J. P. Boeuf, Phys. Rev. A volume **41**, number 8 (1990), pp4447-4459

[15] M. Surendra, D. B. Graves, and G.M. Jellum, Phys. Rev. A Volume **41**, number 2 (1990), pp1112-1125.

[16] A. L. Ward, J. Appl. Phys. **33** (1962), pp2789

[17] H.K. Gummel, IEEE Trans. Electron. Devices ED-**30** (1964), pp1097

[18] D.L. Scharfetter, and H.K. Gummel, IEEE Trans. Electron. Devices ED-**16** (1969), pp64

[19] A. Chutjian, D.C. Cartwright, Phys. Rev. A volume **23**, number 5 (1981), pp2178-2193

[20] N.T. Padial, G. D. Meneses, F. J. Da Paixào, and Gy. Csanak, and David C. Cartwright, Phys. Rev. A, volume **23**, number 5 (1981), pp2194-2211

[21] Fumiyoshi Tochikubo, Zoran Lj Petrovic, Shigeru Kakuta, Nobuhiko Nakano and Tochiaki Makabe Jpn. J. Appl. Phys. Vol. **33** (1994), pp4271-4275.

6. Transport of argon ions in a high density, inductively coupled plasma reactor

6.1 *Introduction*

In the semiconductor industry fast and large-area wafer processing is an important issue in the fabrication of integrated circuits. Recently this has lead to an increased interest in high-density sources, because of their ability of independent control of ion energy and density. One of the most common high density sources, the inductively coupled plasma (ICP), controls the ion density with an inductive coil and the ion energy at the wafer surface with a bias voltage. Some research projects focus on the uniformity of the ion bombardment over the wafer surface[1]. To understand how the etch results are influenced by the plasma conditions, it is necessary to investigate the formation of the ions in the plasma and to determine how they gain their energy during the trajectory towards the electrode.

Processes like collisions and ionization have a direct influence on the ion velocity distribution at the wafer surface. In these low pressure, high density plasmas, the sheath is collisionless and thin. The thickness of the presheath is of the same order of magnitude as the dimensions of the plasma. The velocity distribution function (VDF) of the ions at the electrode is therefore directly determined by the processes in the presheath. At the transition from the presheath to the sheath, the continuity of the charged particle flux implies that the ions must fulfill the Bohm criterion. This theoretical condition says that the velocity of the ions at the sheath edge must exceed the Bohm velocity, which is determined by the electron temperature and the ion mass. So far, an experimental proof of this theoretical velocity has not yet been given. In this chapter the velocity distribution function of the ions in the presheath is measured. It is shown that the ions fulfill the Bohm criterion, and the value of the Bohm velocity is determined.

The setup of the ICP reactor, used in the research presented in this chapter, is described in section 6.2. In this reactor, a number of measurements are carried out to determine various plasma parameters (section 6.3). From the infrared absorption profile, measured with a tunable diode laser, the metastable atom density and gas temperature are obtained at various distances from the top electrode (section 6.3.1). A Langmuir probe system is used in the double and single probe configuration to determine the electron temperature and the ion density in the plasma (section 6.3.2). The dependence of these quantities on the inductive power and the gas pressure is determined. The results are compared with a global model which uses the charged particle and energy balance in the total volume to predict the electron temperature and ion density. The spatial profile of the ion density is compared to the emission profile from atomic levels, which follows the density distribution (section 6.3.3). With Doppler shifted laser induced fluorescence (DSLIF) the velocity distribution function of metastable argon ions is determined inside the presheath of the ICP is measured (section 6.3.4). To investigate the relation between the (measured) metastable ions and the ground state ions (which are dominant in the etch process) a Monte-Carlo model (section 6.4) is developed. It follows the ions on their trajectories in the electric field of the presheath. The presheath theory of chapter 3 is used to calculate the electric field. The results of the measurements and the model are evaluated in section 6.5.

6.2 Setup of the 13.56 MHz inductively coupled plasma reactor

Figure 6.1 shows a schematic view of the ICP reactor and its surroundings. A 15 cm diameter Pyrex bucket (A) contains the plasma inside a 26.2 cm diameter, 20.6 cm high, vacuum chamber. A chromium coated copper cylinder (B) with radial slits is inserted into the bucket to insure Faraday shielding. The ICP is operated in two configurations. In the first situation (I) the metal bucket is placed inside the plasma chamber, as is shown in the figure. In the second situation (II) the bucket is taken out and the a Faraday shield is placed below the quartz window (G). The advantage of the latter configuration is that no sputtering of the chromium takes place and metal deposition on the windows is avoided. Measurements are made in both configurations (I and II). In configuration I it is possible to apply a bias voltage on the bucket to enhance the bombarding ion energy. To compare the two configurations no bias voltage has been applied in this work and the bucket is left floating.

A Pyrex plate (C) is placed on the top electrode to limit the plasma volume to a 15 cm diameter and 3.8 cm high cylinder. In configuration II (no metal bucket) the plasma is surrounded by glass walls. To insure optical access and pressure equilibrium within the vessel, both bucket and metal cylinder have eight equally spaced slits of 6 mm width and 40 mm height (D). In the top electrode a hole of 2 mm diameter, sealed with a Brewster window (E), is used to minimize reflections of the laser beam, going from the bottom to the top.

The pumping system, consisting of a Pfeifer Duo 030A 30 m^3h^{-1} rotary pump (J), a Pfeifer WKP 250 SP LHR 270 m^3h^{-1} roots pump (K), and a Pfeifer TPH 510 500 ls^{-1} turbo pump (L), can achieve a base pressure of 10^{-4} Pa. The gas inlet (M) in combination with an Alcatel automated throttling valve (N) can be set to operate the ICP with constant argon pressures in the range of 0.1-10 Pa.

A three turn, 10 cm diameter copper coil (F) is placed below the 12 mm thick quartz window (G). It is connected to a 13.56 MHz, 100-2000 W RF generator (H) through an L-type capacitive matching network (U). The RF power is dissipated in the plasma as well as in the external components. By applying the same current through the inductive coil with and without plasma the losses in the matching network and other components are determined[2]. The estimated actual power dissipated in the plasma is given in figure 6.2 for different pressures. At 400 W applied power, 40% (160 W) is absorbed in the

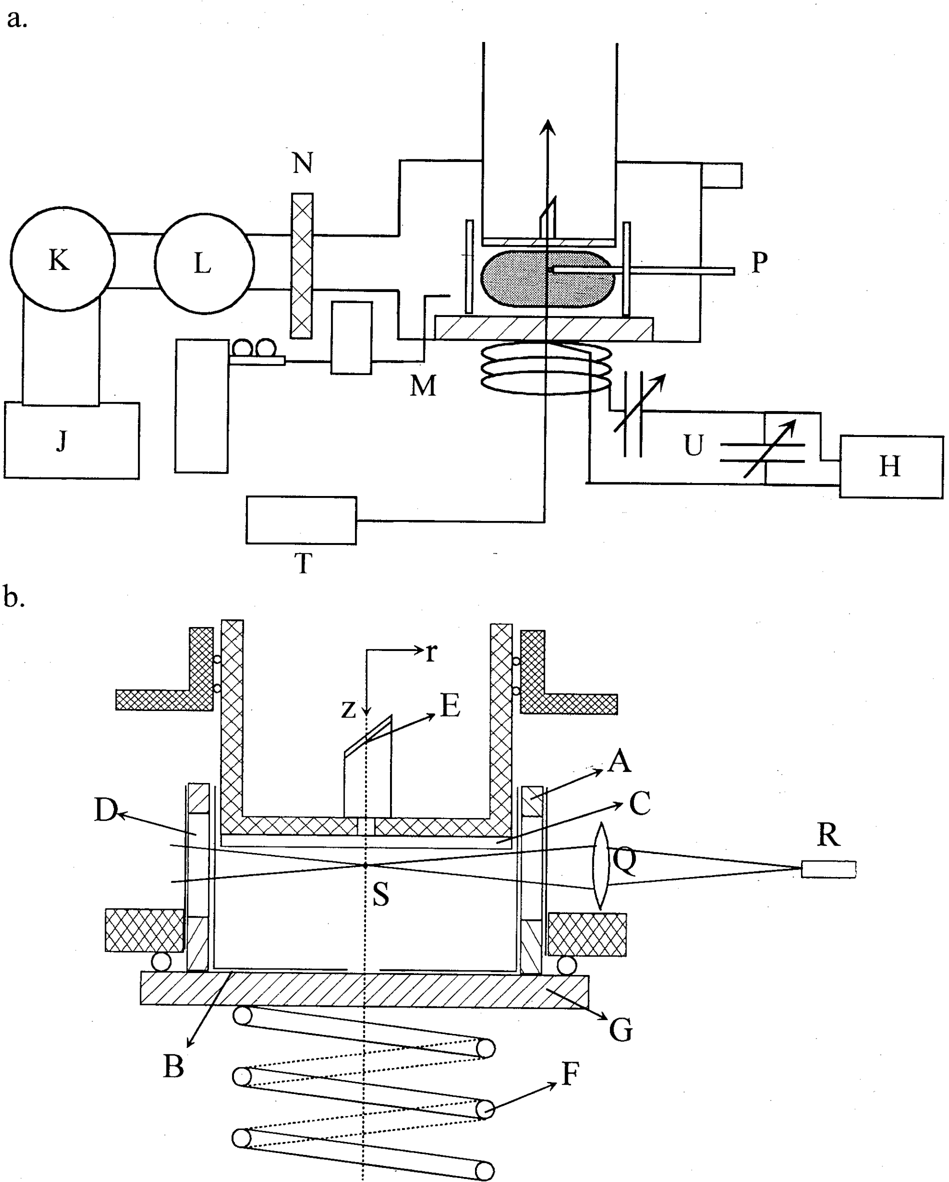

Figure 6.1 : A view of the total setup (a) and a close-up view of the ICP reactor (b).

A	bucket	F	coil	L	turbo pump	R	optical fiber
B	Faraday shield	G	quartz window	M	gas inlet	S	observation point
C	Pyrex plate	H	RF generator	N	throttle valve	T	Dye laser
D	observation slits	J	rotary pump	P	Langmuir probe	U	matching network
E	Brewster window	K	roots pump	Q	lens		

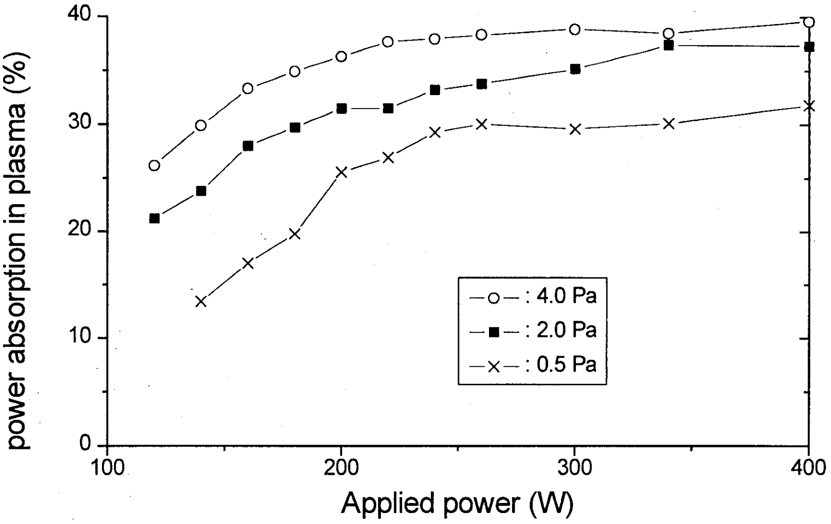

Figure 6.2 : Power efficiency of the ICP reactor.

plasma at 4 Pa and 32% (128 W) at 0.5 Pa. At low pressures the ion density will be lower, hence the conductivity decreases, resulting in a less efficient power transfer.

A Langmuir double probe system (P) can be inserted into the plasma through one of the slits in the bucket. It can be moved in the *z*-direction. The beam of a Coherent tunable dye laser (T) is guided through the plasma along the *z*- or *r*-axis.

The emission and fluorescence radiation is collected at a right angle to the laser direction by a 10 cm focal length lens (Q), located at 20 cm from the reactor axis. The observation point S on the reactor axis is imaged 1 to 1 into a 1 mm diameter optical fiber (R). The spatial resolution is therefore ±0.5 mm in both axial and radial directions. The slit-shaped other end of the fiber is positioned in front of the entrance slit of a 60 cm Jobin Yvon HRS2 monochromator equipped with an R1617 Hamamatsu photomultiplier.

6.3 Measurements

6.3.1 IR laser absorption spectroscopy

The gas temperature is an important quantity which determines the relation between the pressure as measured with the pressure gauge and the gas density. The latter is used in models to calculate the excitation and ionization rates. The temperature also determines the velocity distribution function of newly created ions.

Infrared laser absorption spectroscopy is a non-intrusive tool to measure both the temperature as well as the density of the absorbing level, see section 4.3. Here, a single mode diode laser is tuned on the 772.376 or 772.421 nm argon line which can be absorbed by $1s_5$ or $1s_3$ metastable atoms, respectively. Before crossing the ICP reactor along a line perpendicular to the reactor axis, the laser beam is attenuated to around 10 μWcm^{-2} to avoid saturation and optical pumping[3] (see also chapter 4). By tuning the diode laser frequency and recording the transmitted signal, the absorption profile of the line is obtained. The obtained curves are fitted with Gaussian functions and the gas temperature is deduced from the Doppler width of the profile, see section 4.3 and figure 6.3a. It is assumed that due to the high efficiency of the elastic and metastable-exchange collisions, the metastable and ground state argon atoms have the same temperature. The density of the metastable atoms is obtained by calculating the area under the Gaussian profiles.

As shown in figure 6.3c, the measured gas temperature, T_g, increases with the applied RF power. The temperature does not (or slightly) depend on the pressure. The uncertainty of T_g is around 5%. T_g does not depend on the position of the laser beam relative to the top glass plate and is homogeneous within the plasma volume. Considering a pressure equilibrium between the position in the vacuum vessel where the capacitance manometer is located and the ICP volume, T_g fixes the gas density inside the plasma.

The metastable density is larger for a higher pressure and shows only a slight dependence on the power (see figure 6.3b). Apparently the electron temperature (which determines the excitation to the metastable states) does not change significantly when the power is increased.

a.

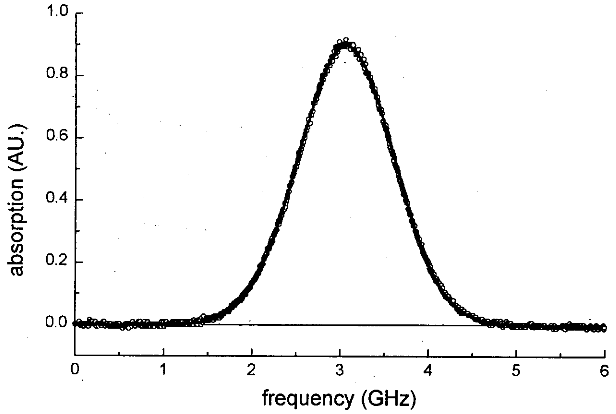

b.

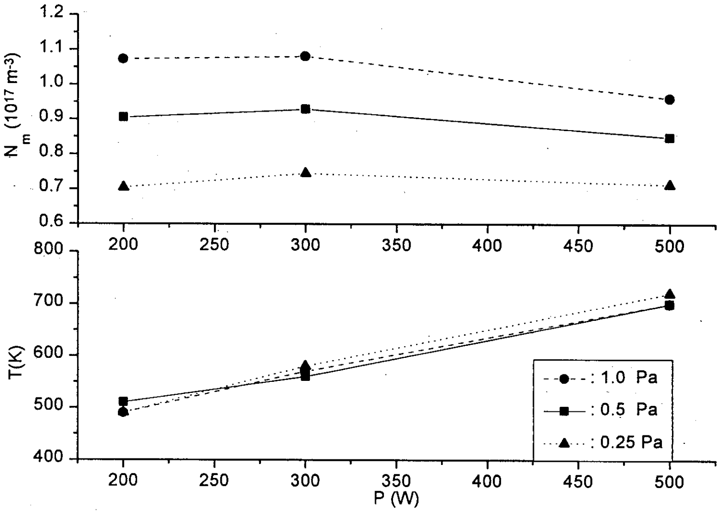

c.

Figure 6.3 : Graph a. shows an example of the obtained absorption profiles (o) together with the fitted Gaussian function (-). The gas pressure is 2 Pa and the power is 400 W. The density and temperature of metastable atoms as a function of the applied power for three pressures, obtained in the center of the plasma, are shown in parts b. and c.

6.3.2 Langmuir probe

The ion density N_i and electron temperature T_e are two of the most important parameters in the characterization of the plasma. Unfortunately, the measurement of N_i and T_e is not so straightforward. The most common technique to measure these parameters is with a Langmuir probe system. A metal probe in contact with the plasma collects a current I, which depends on the voltage V applied to the probe. Variation of the probe potential creates an $I(V)$ profile, which is analyzed to deduce the electron temperature and ion density. The main drawbacks of the Langmuir probe system are that it disturbs the plasma and that the theories which relate N_i and T_e are diverse. Section 4.4 describes the setup of the double cylindrical probe system used to obtain the ion density and electron temperature in the ICP reactor. The two cylindrical probe tips of 400 μm diameter and 3.9 mm length are placed 2 mm apart. The system is used in the double (DP) and in the single probe (SP) configuration.

In configuration I (bucket inside) the probe system is used in the single probe configuration. The results of this measurement are labeled SP-I. The current from one tip to ground is measured, while the other tip is left floating. Grounding the other tip has no influence on the measured probe traces. Using the square root form of the ion current (equation 4.10) and the exponential, Maxwellian electron current (equation 4.11), the single probe $I(V)$ characteristic can be simulated for any combination of the ion density N_i, electron temperature T_e and plasma potential U_{plasma}. For every measured probe trace the values for the N_i and T_e are obtained from the best fit of the calculated to the measured $I(V)$ characteristic.

The probe is also used to measure the electron temperature and ion density in the situation where the metal bucket and Faraday shield are moved outside the vacuum to prevent sputtering (configuration II). Here, the plasma is mainly surrounded by insulating glass walls and the access to the reactor wall and other grounded surfaces is limited. As a result, a variation in the voltage in the electron saturation part of the single probe induces non-negligible changes in the plasma potential. Therefore, it is not possible to use the same procedure as in configuration I to obtain the plasma parameters (see section 4.4.3). However, in the ion saturation part, the current to the probe is much lower and can easily be compensated by the flux of electrons to the walls of the ICP reactor, without considerable changes in the plasma potential. Therefore, the ion current part of this characteristic is reliable. From this, the electron density can be obtained by determination of the slope of the relation between I^2 and V, see section 4.4.1. The results of this measurement are labeled SP-II.

To deduce T_e in configuration II, the double probe traces are evaluated with the equivalent resistance method (see section 4.4.2). The slope of the $I(V)$ characteristic around zero potential is directly related to the electron temperature. These results are labeled DP-II. An example of the obtained probe traces in the SP-I and DP-II configurations is shown in figure 6.4.

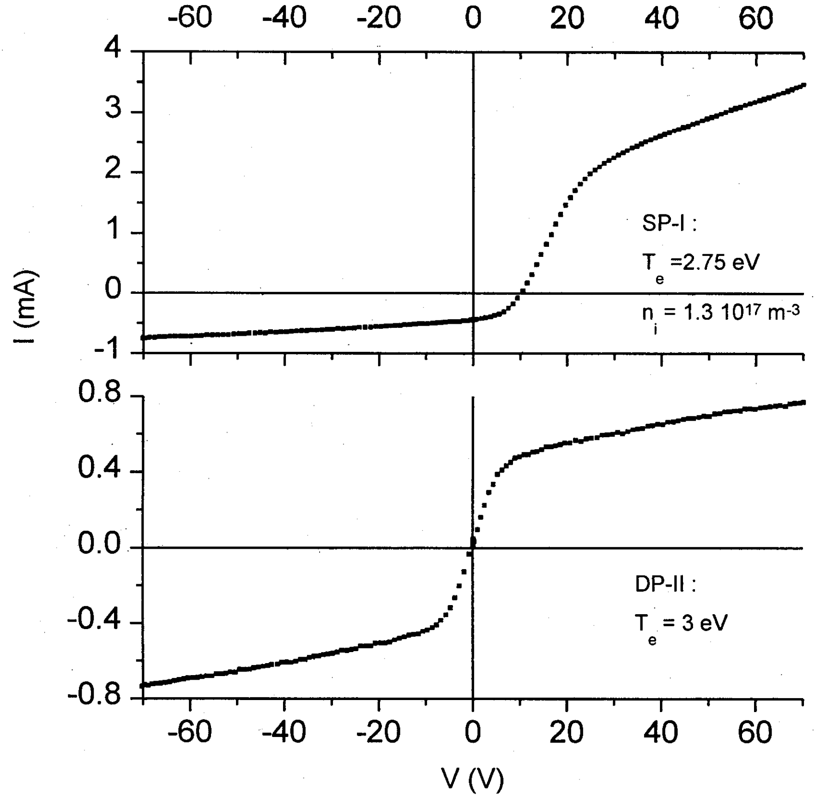

Figure 6.4 : Single and double probe traces for a 200 W, 2 Pa argon plasma at z=18 mm from the electrode.

The electron temperature and density are both measured on the reactor axis (r=0) as a function of distance z from the electrode, pressure p, and power P. The results are shown in figures 6.5-6.7. The figures show a good correspondence between the single and the double probe measurements.

The determination of N_i in figures 6.6 and 6.7 shows that the single probe measurements give the same results in both configurations I and II. It can therefore be concluded that the absence of the metal bucket has no influence on the plasma. Also the values of the electron temperature, as measured with the double probe, are in good agreement with the single probe measurements. Therefore, both double and single probe methods may be used independently for the determination of N_i and T_e. As a conclusion, the probe results can be used to give the N_i and T_e for both configurations (I or II) and they are independent of the measuring method (SP or DP).

Figure 6.5a shows that at 0.2 Pa the electron temperature is uniform throughout the plasma. At these low pressures the mean free path of the electrons is in the order of the reactor dimensions. As a result, an electron can travel a large distance before undergoing a collision. The energy of the electron is therefore distributed equally over the whole plasma volume, resulting in a uniform electron temperature. The spatial dependence of the ion density is shown in figure 6.5b. It decreases in the presheath region because the ions are accelerated towards the top glass plate. The profile is compared to the results of the optical emission measurements, which are described in section 6.3.3.

Figure 6.6 shows the dependence of the ion density and electron temperature on the pressure. At higher pressures, more atoms can be ionized, resulting in an increasing ion density. Due to the larger number of collisions, the electrons loose more energy per time interval. This results in a decay in the electron temperature for higher pressures.

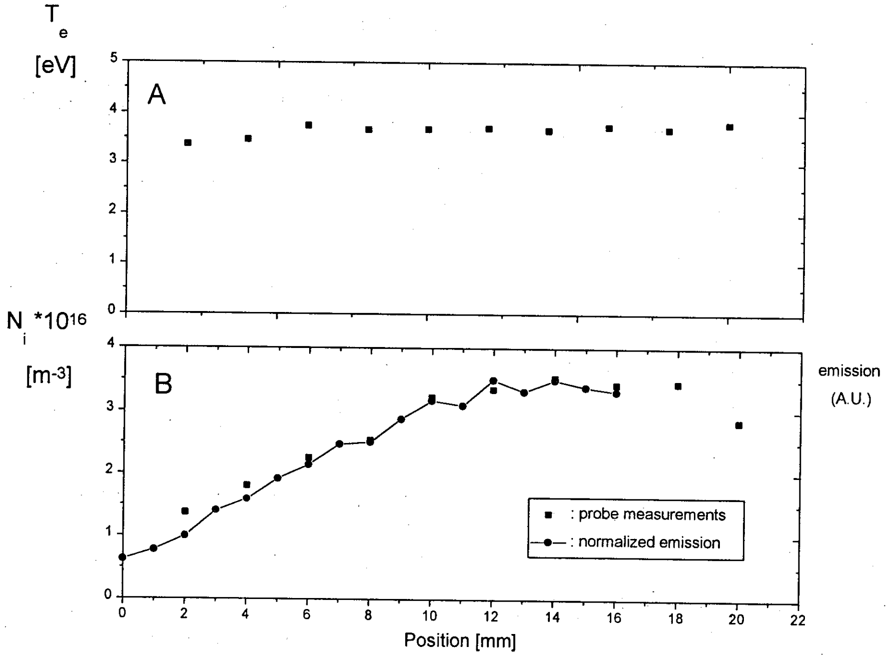

Figure 6.5 : Spatial dependence of the electron temperature (A) and ion density (B) at 200 W applied power and at a pressure of 0.2 Pa. The ion density is compared to the 750 nm emission from the $2p_1$ argon atom level.

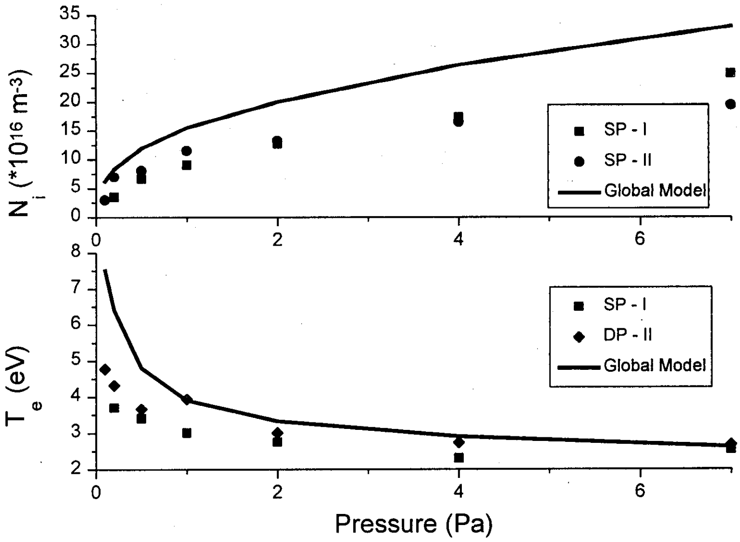

Figure 6.6: Ion density and temperature versus pressure at 200 W applied power in the center of the plasma.

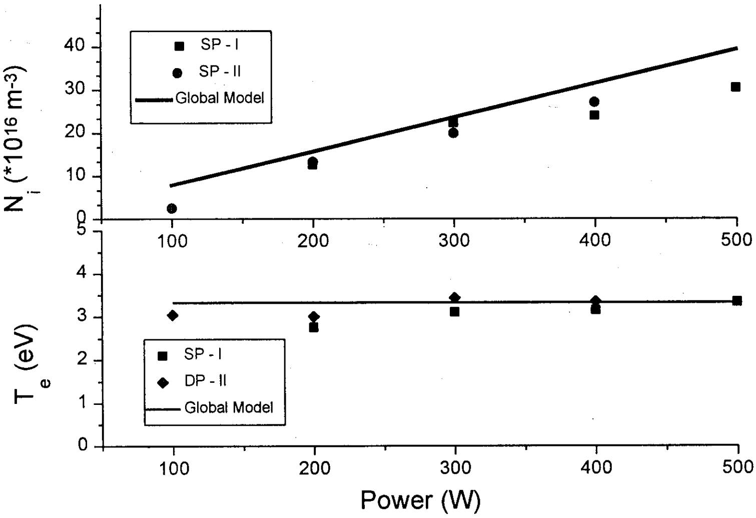

Figure 6.7 : Ion density and temperature versus the applied RF power at a pressure of 2 Pa in the center of the plasma.

The increase in power does not result in an increase in the electron temperature, but only in the ion density, see figure 6.7. Apparently, a higher power will cause an immediate increase in the ionization rate, which is balanced by an increase in the transport of charged particles to the walls. The constant electron temperature points out that both production and loss processes are linear with the plasma density.
To interpret this conclusion more thoroughly, a global model as proposed by Liebermann and Gottcho[4] is applied to the ICP discharge. Due to the uniform electron temperature the ionization rate K_{iz} can be considered to be constant over the whole plasma volume. Hence, the total production rate S of ions and electrons is :

$$S = K_{iz} N_g N_e V \,, \qquad 6.1$$

with N_g the gas density, N_e the electron density and V the volume of the plasma.
The loss mechanisms of charged particles are ambipolar flux to the walls and recombination. According to the literature[5], the rate constant for radiative recombination :

$$Ar^+ + e^- \rightarrow Ar + h\nu,$$

is $10^{-19} m^3 s^{-1}$ (for an electron temperature of 3 eV). The total recombination rate for a typical ion density of $10^{17} m^{-3}$ and a volume of 0.7 liters is $R_{rec} = K_{rec} N_e^2 V = 10^{15}\ s^{-1}$.
The rate constant for 3-body recombination :

$$Ar^+ + 2e^- \rightarrow Ar + e^-,$$

is in the order of $10^{-23}\ m^3 s^{-1}$ (for $T_e = 3$ eV and $n_i = 10^{17}\ m^{-3}$) and can be neglected. The ambipolar diffusion is typically determined by the flux of charged particles to the walls, having the Bohm velocity. For $v_B = 5\ kms^{-1}$, an ion density of $10^{17} m^{-3}$, and a wall surface of 0.05 m^2, the ambipolar loss rate is $R_{amb} \approx N_e v_B A = 3 \cdot 10^{19}\ s^{-1}$. Therefore the contribution of recombination to the total loss of charged particles can be neglected.
More accurately, the ambipolar loss rate is given by :

$$R_{amb} = 2 N_{sH} v_B A_H + N_{sR} v_B A_R \,, \qquad 6.2$$

with v_B the Bohm velocity and N_{sH} and N_{sR} the densities at the sheath edges covering the areas A_H at the top and bottom of the cylindrical reactor and A_R covering the sidewall. The relations between the densities at the sheath edges and in the center of the plasma are not trivial. They depend on the transport of the ions and electrons in the presheath. The mean free path of the ions, λ_i, determines if the presheath is collisional or not. The cross-section for ion-atom quenching collisions is 50 A^2 (see appendix A). For these pressures the corresponding mean free path, λ_i is in the same order of magnitude as the radius R and height H of the reactor. As an example, $\lambda_i = 17$ mm for 1 Pa. Therefore, the density at the sheath edge can not be described by simple theories like a free fall model or diffusion solutions. However, a rough estimate can be made by combining the results of the collisional and collisionless theories[6] :

$$\frac{N_{sH}}{N_0} = h_H \approx 0.86\frac{1}{\sqrt{3+\dfrac{H}{2\lambda_i}}}$$
$$\frac{N_{sR}}{N_0} = h_R \approx 0.80\frac{1}{\sqrt{4+\dfrac{R}{2\lambda_i}}}, \quad 6.3$$

with N_0 the density in the center of the plasma. For the pressures used here, values for h_H are typically between 0.2 and 0.4. When comparing the estimated values with the measured, shown in figure 6.5b, it can be seen that these values are of the right order of magnitude.

In steady state, the loss equals the production, so after combining equations 6.1 and 6.2 :

$$\frac{K_{iz}}{v_B} = \frac{1}{N_g d_{eff}}, \quad 6.4$$

with d_{eff} an effective size, defined as :

$$d_{eff} = \frac{RH}{2(Rh_H + Hh_R)}. \quad 6.5$$

The left hand side of equation 6.4 depends only on the electron temperature, whereas the right hand side depends only on the gas pressure. Therefore, the electron temperature can be solved as a function of pressure when K_{iz} is known (see appendix A) and equation 3.15 is used for v_B. It can also be seen that under these assumptions, the electron temperature does not depend on the applied power.

As far as the power dependence of the electron temperature is concerned, figure 6.7 shows that the theoretical curve is in good agreement with the experiment. Indeed the electron temperature does not change with the applied power.

Also the pressure dependence of the electron temperature, shown in figure 6.6, is in good agreement with the measurement. At low pressure the difference between the calculated and the experimental data is the largest. Possible causes may be a non-Maxwellian electron energy distribution function or the validity of probe theories.

To derive an expression for the dependence of the ion density on pressure and power, the energy relations have to be investigated. It is assumed that all absorbed electromagnetic power is transferred to the electrons, which is reasonable, because of the high mass of the ions. The energy of the electrons is lost by several processes :

1. Elastic collisions with atoms : The transferred energy per collision is given by :

   $$E_{el} \approx \frac{2m_e}{M}\frac{3}{2}kT_e, \quad 6.6$$

   using the fact that the mass of the electron m_e is much smaller then the mass of the atom M, see equation 2.36.

2. Excitation : The energy loss E_{exc} is at least the difference between the ground state and the first excited state of argon (11.6 eV, see appendix A).
3. Ionization : The energy loss E_{iz} is at least the ionization energy of 15.8 eV.

The total collisional energy loss per second is given by :

$$W = N_e N_g V K_{iz} E_c, \tag{6.7}$$

where the average collisional energy loss E_c is defined as :

$$K_{iz} E_c = K_{iz} E_{iz} + K_{exc} E_{exc} + K_{el} \frac{3m_e T_e}{M}, \tag{6.8}$$

using the appropriate K-factors for the various loss processes. The K-factors are calculated by integrating the corresponding cross-sections over the Maxwellian electron energy distribution function, defined by the electron temperature T_e (see Appendix A).

The total energy loss from the system is formed by collisions and kinetic energy loss from ions and electrons escaping to the walls. Again recombination is neglected for the same reasons as described above. When an ion is lost to a floating wall, it has a kinetic energy of αkT_e, which is determined by the difference between plasma and floating potential. For argon, the coefficient α is approximately 5.18, see equation 2.8. When being absorbed by the wall, the electrons lose an energy of $2kT_e$, which can be evaluated by integration of the electron energy distribution. This value is higher than the average energy, because only the fast electrons are lost and the slow electrons are reflected in the sheath. The total energy loss per created ion-electron pair is thus given by :

$$E_L = E_c + (\alpha + 2)kT_e \tag{6.9}$$

The production rate of electron-ion pairs is given by equation 6.1 and equals the loss. Now, the balance between absorbed power P_{abs} and the total energy loss per second is :

$$P_{abs} = N_e v_B E_L A_{eff}, \tag{6.10}$$

with A_{eff} the effective area, given by :

$$A_{eff} = 2\pi R^2 h_{sL} + 2\pi R H h_{sR} = \frac{V}{d_{eff}}. \tag{6.11}$$

From equation 6.10, the pressure and power dependence of the ion density can be obtained when the absorbed power is known. Figure 6.7 shows the predicted relation between the ion density and the input power, when the efficiency is taken as 35 %. From figure 6.2 can be seen that this efficiency is not constant, but depends on the pressure and power itself. In particular at powers below 200 W, the ion density is low and the power is less efficiently transferred to the plasma. Therefore, the relation between ion density and the power will not be a straight line, but will have some offset to take into account the minimum sustaining power. The theoretical curve of figure 6.7 over-estimates the pressure dependence of the ion density. This can be explained by the fact that some loss processes are neglected. These can be excitation to higher levels and the formation of double ionized argon ions. Including these in the calculation increases E_c, which results in a lower predicted value for N_i.

6.3.3 Optical emission spectroscopy

One of the easiest ways to obtain information about the plasma is by looking at the emitted light. With optical emission spectroscopy (see section 4.2) the emission intensity profiles of various lines, originating from different level transitions, provide more insight in plasma processes like excitation and ionization. The main advantages of this diagnostic are that it does not influence the plasma and that it is relatively simple. Optical emission spectroscopy is used to measure the time averaged emission from atomic and ionic argon levels in the ICP plasma as a function of the distance *z* from the top glass plate. As an example, the emission profile of the 750.4 nm ($2p_1 \rightarrow 1s_2$) atomic line is shown in the lower graph of figure 6.5. The time averaged emission $I(z)$ is directly proportional to the source term for the population of the level. For atomic levels, the main population mechanism is excitation from ground state atoms by electrons. Therefore, the intensity of atomic transition lines is linearly related to the electron density $N_e(z)$:

$$I(z) \propto N_e(z) N_g K_{exc}, \qquad 6.12$$

with K_{exc} the rate coefficient for excitation, as defined in equation 2.32. N_g is the gas density. The coefficient K_{exc} depends on the cross-section of electron-atom collisions

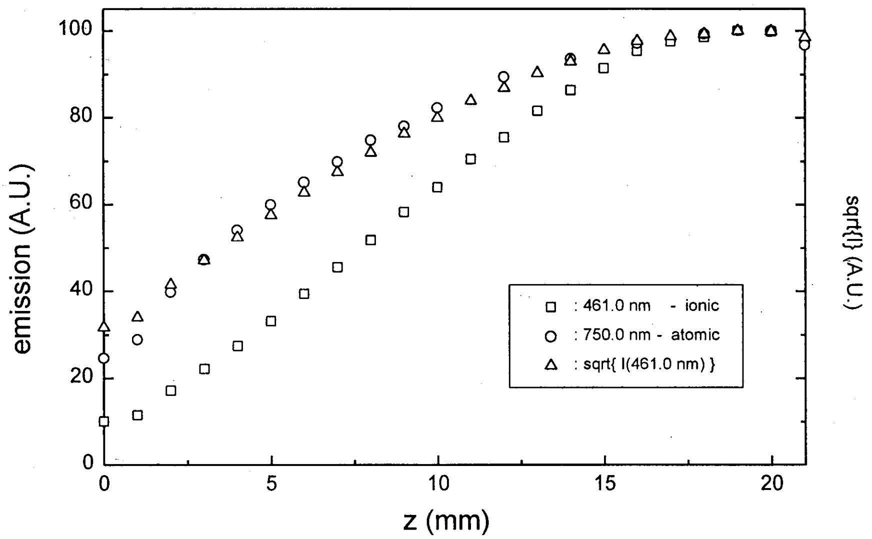

Figure 6.8 : Spatial emission profiles for atomic and ionic levels at 0.5 Pa. The position z = 0 is the top electrode.

and on the electron velocity distribution function. The latter is determined by the electron temperature T_e. Because T_e is constant over z, due to the large mean free path of electrons, the emission profile is an image of the spatial electron density profile $N_e(z)$.

For the emission from ionic levels, the source term for the population can consist of excitation from ground state atoms and from ground state ions. For direct excitation of the $4p'^2F_{7/2}$ ionic level from the ground state atom level 36.9 eV is needed, while the energy difference between the ground state ion level and the ion level is only 21.1 eV. For an electron temperature in the order of 3 eV the latter process is much more favorable, even if the ion density, which is lower than the atom density, is taken into account. Also the cross-sections of the two excitation processes will not be the same, due to the difference in interaction. The strength of coulomb interaction is much stronger than the strength of dipole interaction.

If the main excitation is excitation from the ground state ion level, the emission intensity from ionic lines must be proportional to the square of the electron density :

$$I(z) \propto N_e^2(z) K_{exc}^*, \tag{6.13}$$

with K^*_{exc} the rate coefficient for the excitation from the ground state ion level.

In figure 6.8 the spatial profiles of both 461.0 nm ionic and 750.4 nm atomic emission as well as the square root of the ionic emission profile are plotted. All curves are normalized to 100. It can be seen that the curve of the square root of the ionic line coincides with the atomic curve, indicating the quadratic and linear dependence on the spatial electron density profile. This provides a proof of the assumption that the source term for the population of the excited ionic levels from atomic states can be neglected. The comparison of the 750.4 nm atomic emission profile with the results of the Langmuir probe, as shown in figure 6.5b, shows that the emission profile is indeed an image of the ion density profile. The Langmuir probe measurements are less accurate than the emission measurements. Therefore, the spatial electron density profile can best be constructed from the emission profile which is normalized in the center of the plasma to the value of the ion density obtained from the Langmuir probe measurement. From this profile, also the potential can be deduced, using the exponential relation between the ion density and the potential (see equation 3.8). Therefore :

$$V(z) = -\frac{kT_e}{e}\ln\left(\frac{N_e(z)}{N_0}\right) = -\frac{kT_e}{e}\ln\left(\frac{I(z)}{I_0}\right), \tag{6.14}$$

with $I(z)$ the emission intensity profile, which is I_0 in the center of the plasma. Differentiation to z leads to the electric field in the presheath.

In figure 6.9 the potential deduced from the emission and from the theory of chapter 3 are compared. The theoretical curve is constructed using the cross-sections for collisions and ionization. It can be seen that the curves are in good agreement except close to the electrode. Here, the theory of chapter 3 does not take into account the transition from the presheath to the sheath, where the quasi-neutrality is violated. Therefore, the theoretical curve predicts a singularity at $z = 0$.

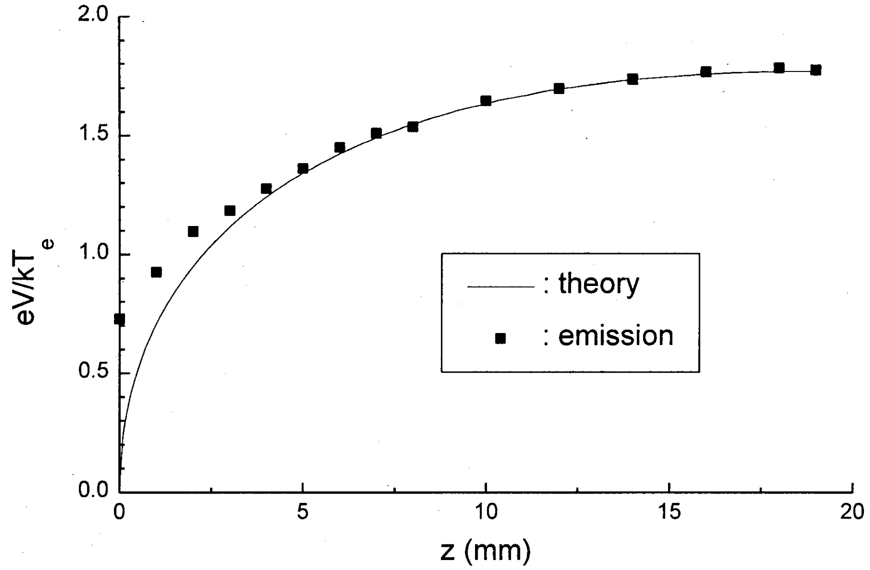

Figure 6.9 : Comparison between the potential obtained from emission experiments and from the presheath theory.

From the emission plots of figure 6.8 can also be concluded that there is no glow region with a constant electric field and that the presheath extends to the center of the plasma.

6.3.4 Doppler shifted laser induced fluorescence (DSLIF)

To determine how the velocities of the ions in the ICP change in the vicinity of the electrode, Doppler shifted laser induced fluorescence is used to measure the local ion velocity distribution function (IVDF). Metastable $3d'^2G_{9/2}$ argon ions are excited to the $4p'^2F^0_{7/2}$ level with 611.493 nm laser light. A stabilized continuous wave single mode Ar^+-pumped Coherent "899-29 Autoscan II" ring dye laser is used to scan the laser wavelength around the transition. Only ions which have a velocity component that fits to the Doppler shifted laser frequency will make the transition. The increased fluorescence from the upper level is a measure for the local density of metastable ions with velocity components corresponding to the applied laser frequency. Inside the reactor, the laser beam propagates along the reactor axis to observe $f(v_z)$, the ion velocity distribution function (IVDF) parallel to the mean drift velocity of the ions toward the top glass plate, or along the diagonal direction to observe $f(v_\perp)$, the IVDF parallel to the glass plate surface and perpendicular to the reactor axis.

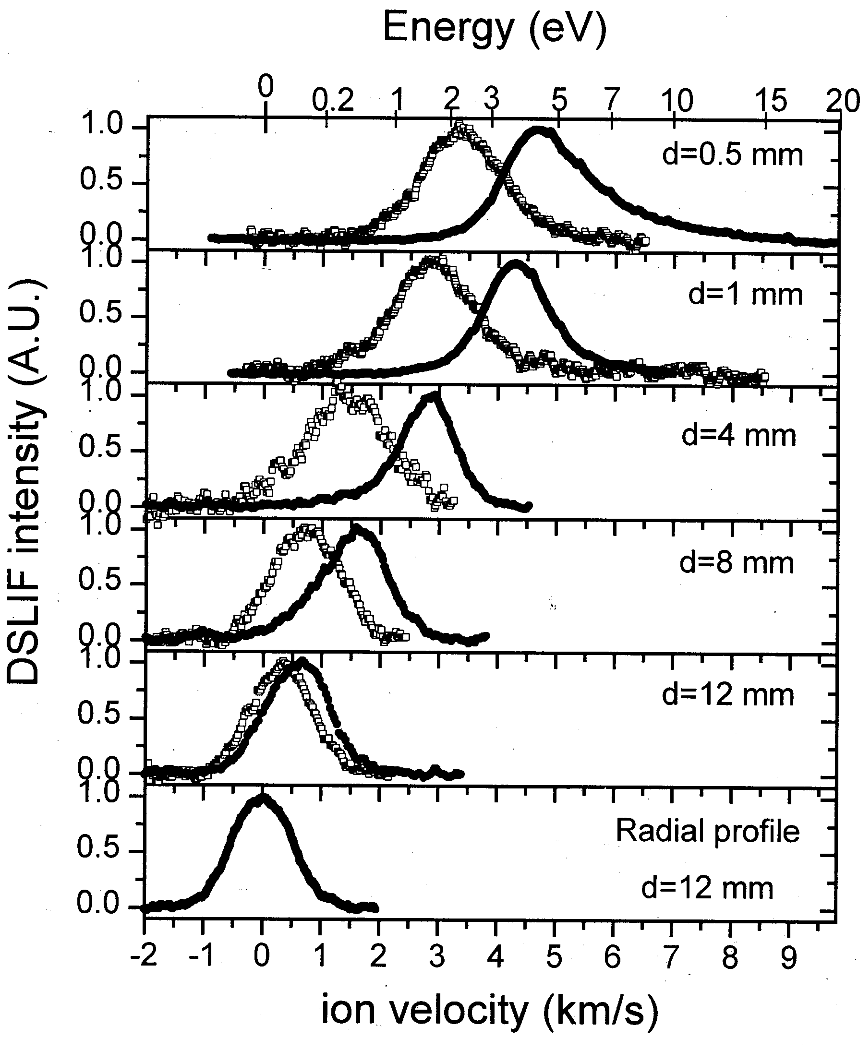

Figure 6.10 : DSLIF results for 0.5 Pa(•) and 4 Pa (□) at 400 W. d is the distance from the top glass plate.

To separate the DSLIF signal from the strong background emission signal, the laser beam is modulated at 300 Hz, before entering the reactor. The DSLIF signal is extracted using a lock-in amplifier. By tuning the laser frequency and recording the DSLIF signal, the IVDF profile is obtained. The resulting profiles for 0.5 and 4 Pa argon pressure can be seen in figure 6.10. All curves are normalized to unity. The bottom graph shows the radial profile, $f(v_\perp)$ at z = 12 mm. The profile is symmetrical around zero velocity and has a Gaussian shape. The other graphs show the axial velocity profiles, $f(v_z)$, at various distances z from the glass plate. The averages of the curves have non-zero values and shift to higher velocities when approaching the glass plate. Also can be seen that already at 12 mm from the glass plate the ions have a non-zero velocity component. Hence the presheath extends to the middle of the plasma, as was already mentioned in section 6.3.3.

The results of figure 6.10 can be separated into the mean parallel energy E_z and the ion temperatures (T_z and $T_\perp$), obtained from the directions parallel and perpendicular to the reactor axis, respectively :

$$E_z = \frac{1}{2} m_i \langle v_z \rangle^2, \qquad 6.15$$

$$kT_z = m_i \left\langle \left(v_z - \langle v_z \rangle \right)^2 \right\rangle, \qquad 6.16$$

$$kT_\perp = m_i \left\langle \left(v_\perp - \langle v_\perp \rangle \right)^2 \right\rangle, \qquad 6.17$$

with m_i the ion mass.

The spatial dependence of these quantities in electron volts are shown in figure 6.11. It can be seen that the energy, gained in the z-direction is partially transferred to the perpendicular directions by collisions. This causes a broadening in the perpendicular DSLIF profiles, indicating a higher temperature $T_\perp$. For higher pressures the energy transfer in the perpendicular directions is more efficient due to the larger number of collisions. This causes a faster increasing $T_\perp$ for higher pressures. The bulk ion temperature of 0.1 eV is higher than the gas temperature of 0.06 eV. A possible cause for this difference can be the fact that Coulomb interaction between electrons and ions is more efficient than between electrons and atoms. Also less efficient cooling by the gas at low pressures.

The DSLIF signal is obtained with a spatial resolution of Δz = 1 mm. As a result, the curves in figure 6.10 are broadened because they are averaged over the detection volume. The broadening can be neglected for the radial profiles, because the ions have no average velocity in the perpendicular direction. For the other curves the broadening is larger for the measurements close to the glass plate, where the drift velocities are higher. This effect causes an overestimation of T_z at small z values, while $T_\perp$ is not influenced.

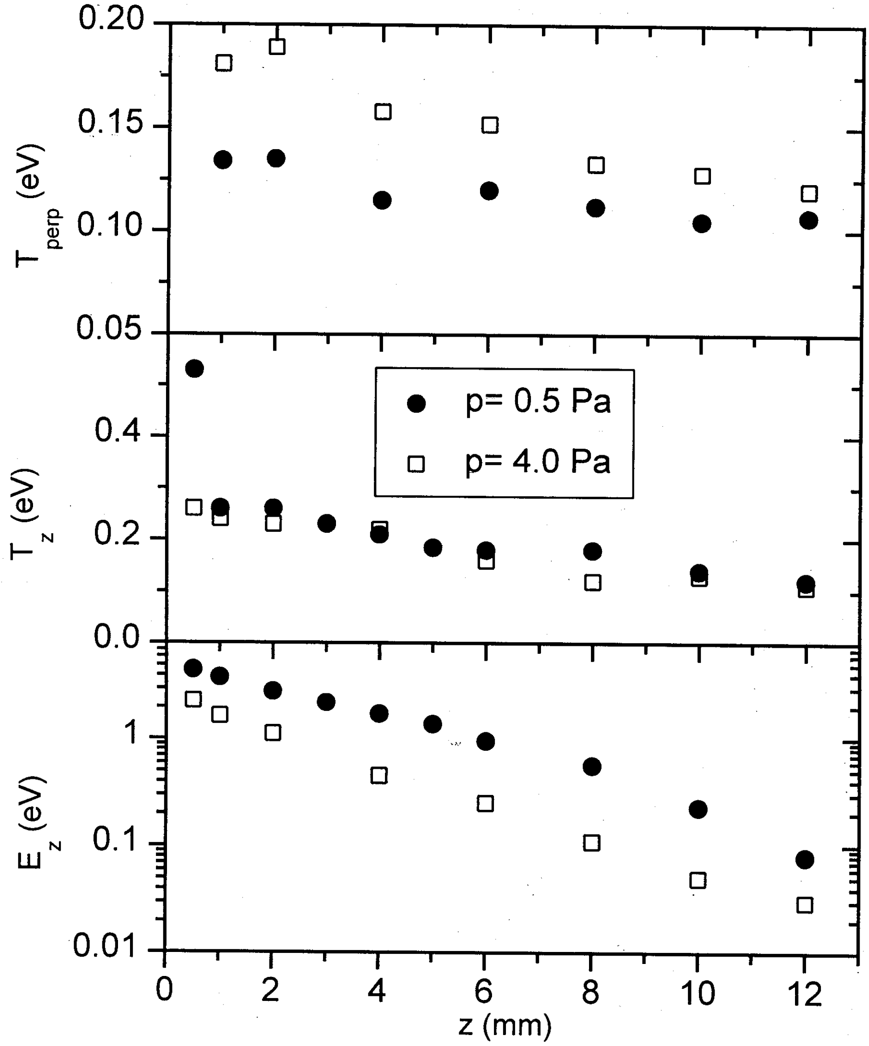

Figure 6.11 : Spatial dependence of the temperatures and ion energy derived from figure 6.8.

The spectral width of the laser is smaller than 500 kHz and the power of less than 100 mW is deposited in an area of 10 mm^2. According to equation 4.29 the theoretical value of the saturation broadening in this case is less than 300 MHz. To determine the linewidth experimentally, the lamb-dip can be measured. The laser beam is guided through the plasma and is reflected with a mirror, placed outside the vacuum chamber. The returning beam follows the same trajectory as the primary beam, but in the opposite direction. The second beam is chopped just after the mirror to measure the DSLIF signal. When the laser beam is scanned around the absorption frequency, the same Doppler profiles appear as before, only now they have a dip at the zero velocity position. This dip is called the Lamb-dip[7]. When the laser beam is set at this central absorption frequency, the second beam measures the Bennet-hole created by the primary beam, see chapter 4. The width of the Lamb-dip is linearly related to the saturation broadened absorption profile.

The measurement of the Lamb-dip under similar circumstances[8] shows that the saturation broadening is less than 200 MHz for this transition. Calculations show that a Voigt profile consisting of a 1 GHz Gauss profile and a 200 MHz Lorentz profile can be fitted with a Gaussian to give a width of 1 GHz with an error smaller than 0.5%.

The size of the sheath is in the order of the Debye length, which is smaller than the detection size. Therefore, part of the signal of the upper curve in figure 6.10 originates from the sheath, where the velocities increase much faster. This can be seen clearly from the tail to higher velocities. Because the density drops dramatically in this region, the maximum of this curve occurs at the average value of the ion velocity with which the ions enter the sheath. According to the theory of chapter 3 the average ion velocity on the sheath edge must exceed the Bohm velocity. Taking the ion temperatures close to the electrode into account, equation 3.51 predicts the Bohm velocities to be 3.1 and 2.7 kms^{-1} for 0.5 and 4 Pa, using the electron temperatures (3.5 and 2.5 eV, respectively) from the probe results. From figures 6.10 and 6.11 it can be seen that the average velocity at the end of the presheath indeed exceeds the theoretical Bohm velocity.

The average velocity of the 0.5 Pa IVDF already exceeds the Bohm velocity at more than 1 mm from the electrode surface. This can not be the edge of the sheath, which is very close to the electrode, due to the small Debye length, which is in the order of tens of micrometers.

The Bohm criterion, however, applies to the total ion distribution and not only to the metastables. Therefore, the relation between the metastable and the ground state ions should be carefully investigated, whether the metastable ion is a good representative of the ground state ion.

6.4 Monte-Carlo model

Because DSLIF measures the velocity distribution function (VDF) of the metastable ions, it should be closely investigated what the relation is between the VDF of the metastable ions and the VDF of the ground state ions. The latter have a much larger density and thus have a much larger impact on the final etching results. When the mean free path of the metastable ions is short, the DSLIF signal is produced by the metastable ions which are created very close to their observation point and can therefore be seen as a kind of probe for the ground state ions. The measured VDF is then an image of the VDF of the ground state ions.

In the low pressure case of the ICP however, the metastable ions can travel a considerable distance in the electric field of the presheath before they are observed or destroyed.

To determine the velocity distribution function (VDF) of the ground state argon ions from the measured VDF of metastable ions, it is therefore important to investigate the relation between the two ion species and to see how they contribute to their respective velocity distribution functions. The motion of the ions in the electric field E of the presheath is simulated with the use of a Monte-Carlo model.

The electric field is derived from the potential profile by differentiation. The potential profile is an input parameter for the model and is obtained in two ways.

Firstly, the spatial emission profile of the atomic line is an image of the spatial electron density, as was shown in section 6.3.3. Inside the presheath region, the electron density, which equals the ion density, is determined by the exponential Boltzmann factor, see equation 3.8. According to equation 6.14 the potential profile can directly be derived from the emission profile.

A second way to obtain the spatial potential profile is from the presheath theory of chapter 3, using the appropriate cross-sections for ionization and collisions. For each pressure the potential in the presheath can be calculated with the use of the electron temperature and ion density obtained with the Langmuir probe.

Because the ionization depends heavily on the electron temperature, a correction factor is used for the ionization rate. This factor is tuned to make the size of the presheath equal to half of the plasma length. It is supposed that this boundary condition is more accurate than the experimentally obtained value of the electron temperature and the cross-section from the literature. The correction factor is found to be 0.3 for the 2 Pa situation.

In figure 6.9 the potentials obtained with both methods are compared. It can be seen that the profiles match for positions with larger z values. Only for positions close to the electrode the two profiles differ significantly. The theoretical potential distribution assumes quasi-neutrality, which is violated close to the electrode at the transition to the sheath. The emission is obtained with a spatial resolution of 1 mm so the contributions are averaged over space. At low z values the variation in the potential is large, so the emission results are less accurate. Also the conversion of the emission intensity profile to the potential may not be valid in this region. The electrons are repelled and their temperature can change.

As a conclusion, both profiles may be used for the potential in the presheath, although not for positions closer than 1 mm from the electrode surface.

Therefore, the theoretical curves are used in this work, because the calculation of the electric field is faster and the curves are smooth. The emission experiment contains noise, which introduces peaks in the deduced electric field. These result in non-existing features in the modeled velocity distribution functions.

Starting from the numerical potential profile, the electron density and electric field are deduced. The latter determines the acceleration of the ions in the presheath. The Monte-Carlo method creates ground state ions inside the presheath, according to the ionization profile with initial velocities determined by the VDF of the ground state atoms. These are assumed to be distributed according to a Gaussian distribution function with a width determined by the gas temperature, as measured with IR absorption spectroscopy (see section 6.3.1). Subsequently, the ions follow trajectories in the presheath which consist of free flights in the electric field, separated by collisions with gas atoms. The collisions can be charge exchange or elastic, depending on the cross-section.

To calculate the time τ between two collisions, the collision frequency ν is evaluated for each type of collision :

$$\nu = N_g \sigma v \,. \qquad 6.18$$

The frequency ν depends on the velocity v of the ion and is therefore not constant during the acceleration of the ion. To avoid excessive computations, the null-collision method[9] is used to simulate the various collisions in the presheath. The flight time between two collisions is calculated from the maximum collision frequency at the highest velocity :

$$t_{flight} = -\frac{\ln(r)}{\nu_{tot}}, \qquad 6.19$$

with r a random number in the range of [0,1] and ν_{tot} the maximum total collision frequency of all collisions, here elastic and charge exchange collisions ($\nu_{\text{ec}} + \nu_{\text{ce}}$).

In figure 6.12 the method is shown in detail. The flight time calculated from equation 6.19 is in general too short because the maximum collision frequency, which is related to the maximum velocity, is used. The difference with the real collision frequency is taken into account by introducing the null-collision, which does not change the velocity of the ion. As expected, the collision frequency for the null-collision is larger at lower velocities. On average, the null-collision method follows the real collisional behavior of the ions. After the time t_{flight} the new position r_1 and velocity v_1 are calculated using the electric field. A random number on the line $v = v_1$ is taken to determine the nature of the collision. Only for the charge exchange and elastic collisions the new velocities are calculated using the collision theory.

During the trajectory between two collisions, snapshots of the position z and the velocity component v_z are taken at fixed time steps and the values in a corresponding grid are increased. The dimensions of the grid points are 0.1 mm in position and 200 ms^{-1} in velocity. The time step is determined by the ratio of the grid size over the maximum velocity in order to be sure to detect the ion at least once in each spatial grid point. After many ions are followed, the grid contains an image of the ion velocity distribution function.

A small electric field in the radial direction is used in the model to take the diffusion of ions to the walls into account.

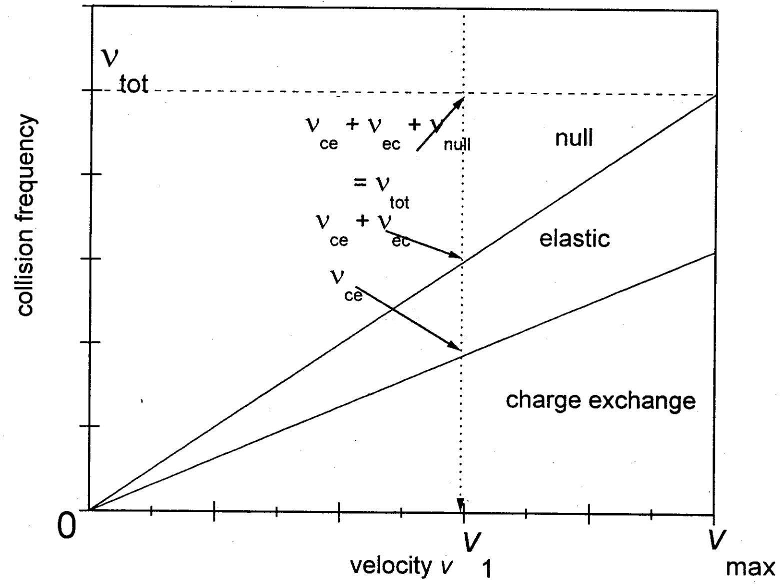

Figure 6.12 : The null-collision method.

While the ground state ions are created from the ground state atom and lost to the walls, the metastable ions are assumed to be created by excitation from the ion ground state and destroyed by collisional quenching and transport to the walls. Therefore, the VDF of the metastable ions can be obtained from the ground state ion VDF using the same procedure as before. Figure 6.13 shows both VDF's for a 2 Pa plasma. It can be seen that the metastable ions do not have exactly the same VDF as the ground state ions, but there is a strong resemblance. At higher pressures, when the mean free path of the ions is short, the metastable ions are detected very close to the position where they are created. The two VDF's are then quite similar. Here, at low pressures, the metastable ions have a considerable time to gain energy, before they are quenched. Also the production of metastable ions close to the electrode is small, due to the lower electron density, which causes a drop in the excitation. Therefore, almost all metastable ions at this position are created far away from their observation point. Unlike the ground state ions, the metastable ions are quenched by collisions and do not return to the VDF with a lower velocity. Therefore, the low velocity part of the metastable ion VDF originates from the metastable ions which are created locally. In the low pressure

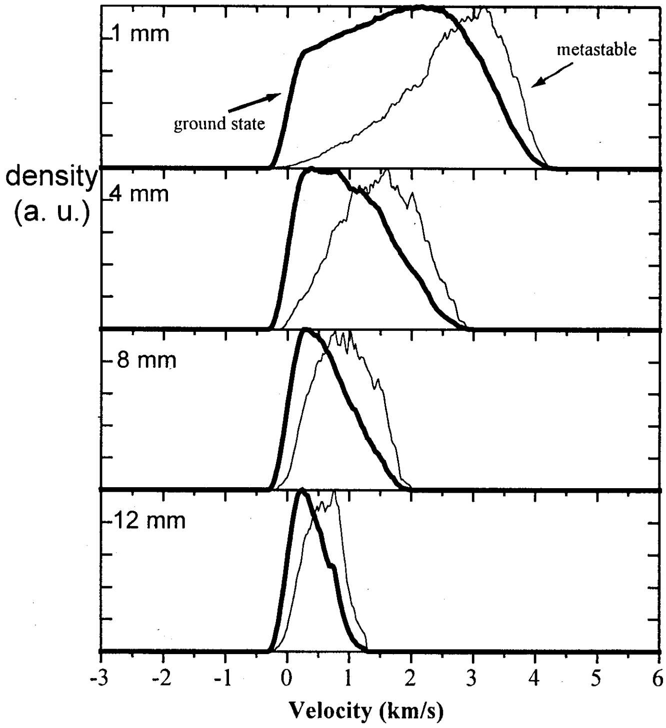

Figure 6.13 : Comparison of the metastable and ground state ion distribution functions for 2 Pa at various distances from the electrode. The top graph shows the VDF's close to the electrode.

situation, this contribution is much smaller than the contribution from metastable ions which are created before the observation point and are already accelerated. Therefore, the metastable ion VDF is depleted at low velocities, which is clearly seen in figure 6.13.

Due to this depletion, the mean velocity of the ground state ions is lower than that of the metastable ions. To check if the total ion distribution obeys the Bohm criterion, the ground state ions must exceed the Bohm velocity.

Figure 6.14 shows the comparison of the metastable ion VDF from the Monte-Carlo simulation and from the measurements. A good agreement is seen between the two curves. The theoretical curve at 12 mm is much narrower than the measured VDF. This is caused by the difference in the temperature. The measured curve shows the ion temperature to be in the order of 0.1 eV, while in the model the ions are created from the atom ground state, having a temperature of 0.06 eV. The possible heating of ions by electron collisions is not taken into account in the model.

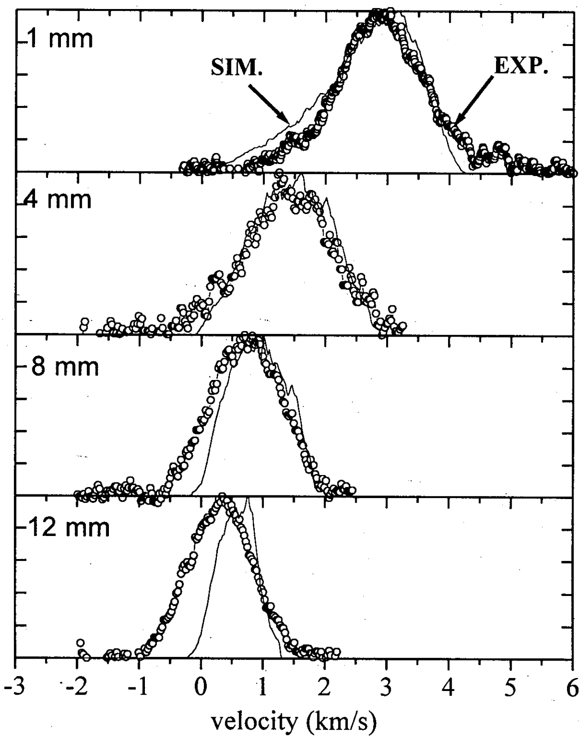

Figure 6.14 : Comparison between the experimental VDF of metastable ions (o) and the results of the Monte-Carlo simulation (-) at several distances from the electrode. The pressure is 4 Pa.

6.5 Conclusions

In this chapter, a low pressure, inductively coupled, 13.56 MHz argon plasma is investigated.

With laser absorption spectroscopy the metastable atom density and gas temperature are determined. The measurement shows no spatial dependence. Increasing the inductive power from 200 W to 500 W raises the temperature from 500 K to 700 K, independent of the pressure. The temperature of the metastable atoms can be considered equal to the gas temperature, due to the effective energy exchange between atoms. The density of metastable atoms shows only a slight dependence on the applied power, whereas the density changes from $7\cdot10^{16}$ m^{-3} at 0.25 Pa to $1\cdot10^{17}$ m^{-3} at 1 Pa.

From Langmuir single and double probe measurements the electron densities and temperatures are obtained for various inductive powers and gas pressures. It is shown that the single and double probe configurations give the same results. Hence, either of the two methods may be used to obtain the plasma parameters. The ICP is operated with the Faraday shield inside and outside the vacuum chamber. The probe results show that the plasma does not change significantly when going from one configuration to the other.

Within the accuracy, the measurements show the same dependence on pressure and power as what can be calculated from a global model. This takes the processes of ionization and ambipolar diffusion into account. Also the spatial profiles of the electron temperature and density are obtained. The first is constant over space, because the mean free path of the electrons is large, compared to the plasma dimensions. Therefore, the measured optical emission profiles of atomic levels show a linear relation with the spatial electron density profile. From the optical emission spectroscopy results it is shown that the population of the excited argon ion levels due to electron impact excitation from the ground state atom level can be neglected as compared to excitation from the ground state ion level.

Using Doppler shifted laser induced fluorescence, the metastable ion velocity distribution function on the reactor axis at various distances from a glass plate is measured. It shows the acceleration of the ions inside the presheath towards Bohm speed at the sheath edge. The average kinetic energy and temperature of the ions can be deduced from the profiles. The ion temperature increases when moving closer to the plate. A fraction of the kinetic energy is transferred into the perpendicular directions. This process is more efficient at higher pressures. The velocities at the edge of the presheath exceed the Bohm velocity, which can be calculated from the electron temperature obtained with the Langmuir probe system. A Monte-Carlo model shows the relation between the velocity distribution function of the measured metastable ions and the ground state ions. It is shown that for high pressures the two distribution functions are similar, whereas for low pressures the low velocity component in the metastable distribution function is attenuated, because the metastable IVDF is not only formed by metastable ions which are created locally, but also from metastable ions which are created before the observation point and are accelerated in the electric field of the presheath.

The modeled metastable ion VDF corresponds well with the measured profiles. An exception is in the beginning of the presheath, where the measurements show a higher ion temperature than is expected by the model. This is caused by the assumption that the ions are created from the atomic ground state velocity distribution, while no heating of the ions is taken into account.

In contrast with the average metastable ion velocity, the modeled ground state ions do not exceed the Bohm velocity in the presheath.

References

[1] R.A. Stewart, P.Vitello, D.B. Graves, E.F. Jaeger and L.A. Berry, Plasma Sources Sci. Technol. **4** (1995) pp. 36-46

[2] P.N. Wainman, M.A. Lieberman, A.J. Lichtenberg, R.A. Stewart and C. Lee, J. Vac. Sci. Technol. A **13** (1995), pp 2464.

[3] R.E. Drullinger and R. N. Zare, J. Chem. Phys. **51** (1969) , pp.5532.

[4] M.A. Lieberman and R.A. Gottcho, *Physics of Thin Films*, edited by M. Francombe and J. Vossen (Academic, New York, 1994), Vol. **18**, pp.1-119

[5] Yuri P. Raizer : *Gas Discharge Physics* ; Springer Verlag

[6] V.A. Godyak, *Soviet Radio Frequency Discharge Research* (Delphic Associates, Falls Church, VA, 1986).

[7] W. Demtroeder : *Laser Spectroscopy* ; Springer-Verlag; ISBN 3-540-57171-X

[8] N. Sadeghi, private communications

[9] H.R. Skullerud, J. Phys. D. **1**, (1968), pp.1567

Appendix A : Argon data

Argon atom :

absorption :

$\lambda = 772.376$ nm : $1s_5 \rightarrow 2p_7$: $A_{ki} = 5.6\ 10^6\ s^{-1}$, $f_{ik} = 0.0306$
$1s_5$: $J = 1$, $g = 5$ (*i*)
$2p_7$: $J = 2$, $g = 3$ (*k*)

$\lambda = 772.421$ nm : $1s_3 \rightarrow 2p_2$: $A_{ki} = 1.3\ 10^7\ s^{-1}$, $f_{ik} = 0.34$
$1s_3$: $J = 1$, $g = 1$ (*i*)
$2p_2$: $J = 0$, $g = 3$ (*k*)

electron collisions :

elastic collisions : $Ar + e \rightarrow Ar + e$: cross-section : see figure A.1.
ionization : Ar + e -> $Ar^+ + 2e$: cross-section : see figure A.2.

electronic excitation : $Ar + e \rightarrow Ar^* + e$

Rate constants for electron collisions in argon gas : excitation, ionization and elastic collisions, see figure A.3.

electronic excitation out of the metastable states :
$2p_1$: $(J = 0 \rightarrow 0)$: $\sigma < 0.2$ Å^2 (1)
$2p_6/3p_8$: $(J = 2 \rightarrow 2)$: $\sigma = 10$ Å^2 (1)

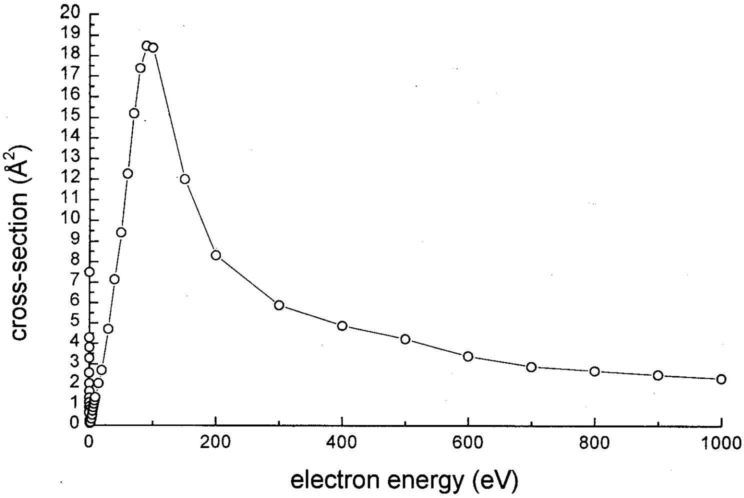

Figure A.1 : Cross-section for elastic collisions of argon.[2]

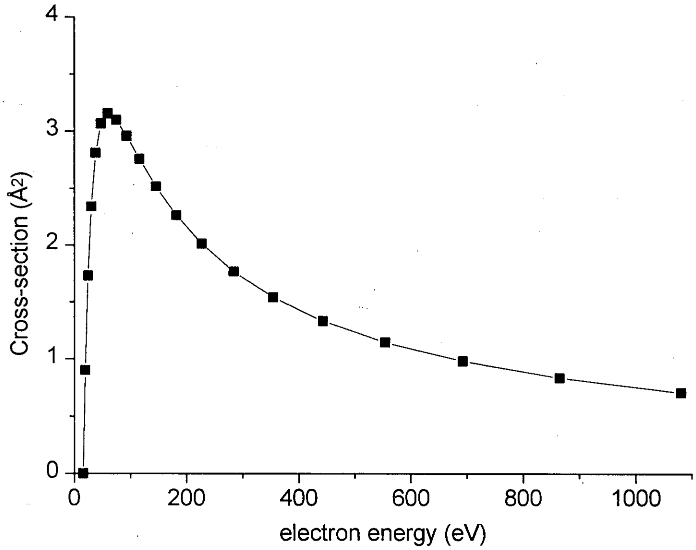

Figure A.2 : Argon ionization cross-section.[3]

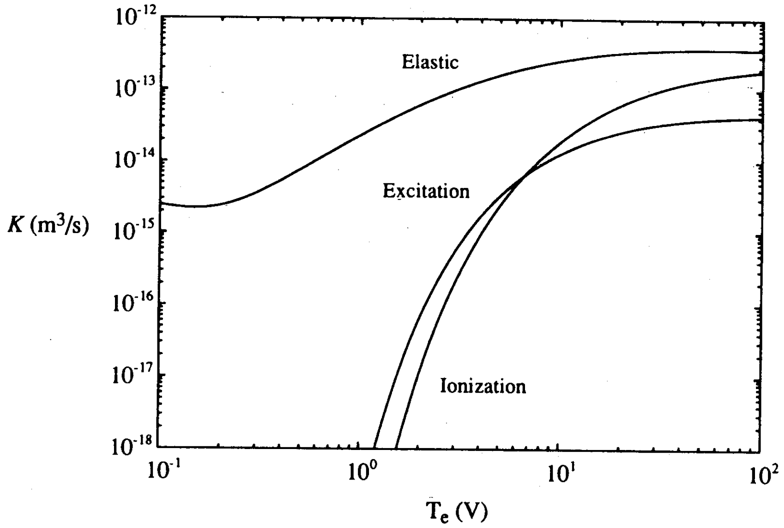

Figure A.3 : Electron-collision rate coefficients in argon gas : ionization, excitation and elastic collisions[5].

Argon ion :

Table A.1 : Parameters for the transition in Ar^+ : $3d'^2G_{9/2}$ (0) → $4p'^2F^0_{7/2}$ (1) → $4s'^2D_{5/2}$ (2)[4]

parameter	*value*
λ_{10}	611.493 nm
λ_{12}	460.96 nm
ω_{10}	3.07 10^{15} Hz
A_{10}	21.2 MHz
A_{12}	75.9 MHz
B_{10}	121.9 10^{11} m^2(Js)$^{-1}$
B_{01}	97.55 10^{11} m^2(Js)$^{-1}$
τ_1	8.5 ns
τ_0	1 μs (5 Pa)
g_1/g_0	0.8
m_i	39.962 amu

quenching :
metastable ions : $Ar^{+*} + Ar \text{->} Ar^{+} + Ar$: 110 Å^2 (^{6})

charge exchange : $Ar^{+} + Ar \rightarrow Ar + Ar^{+}$: 50 Å^2 (^{7})

Ambipolar diffusion:
$D_a = 69\ cm^2(Torr)s^{-1}$ (^{8})

Recombination :
radiative recombination : $Ar^{+} + e^{-} \rightarrow Ar + h\nu$: $2.7\cdot10^{-19}\ (T_e)^{-3/4}\ m^3s^{-1}$ (^{9})
3-body recombination : $Ar^{+} + 2e^{-} \rightarrow Ar + e^{-}$: $8.75\cdot10^{-39}\ (T_e)^{-3/4}\cdot n_e\ m^3s^{-1}$ (^{8})
(T_e in eV and n_e in m^{-3})

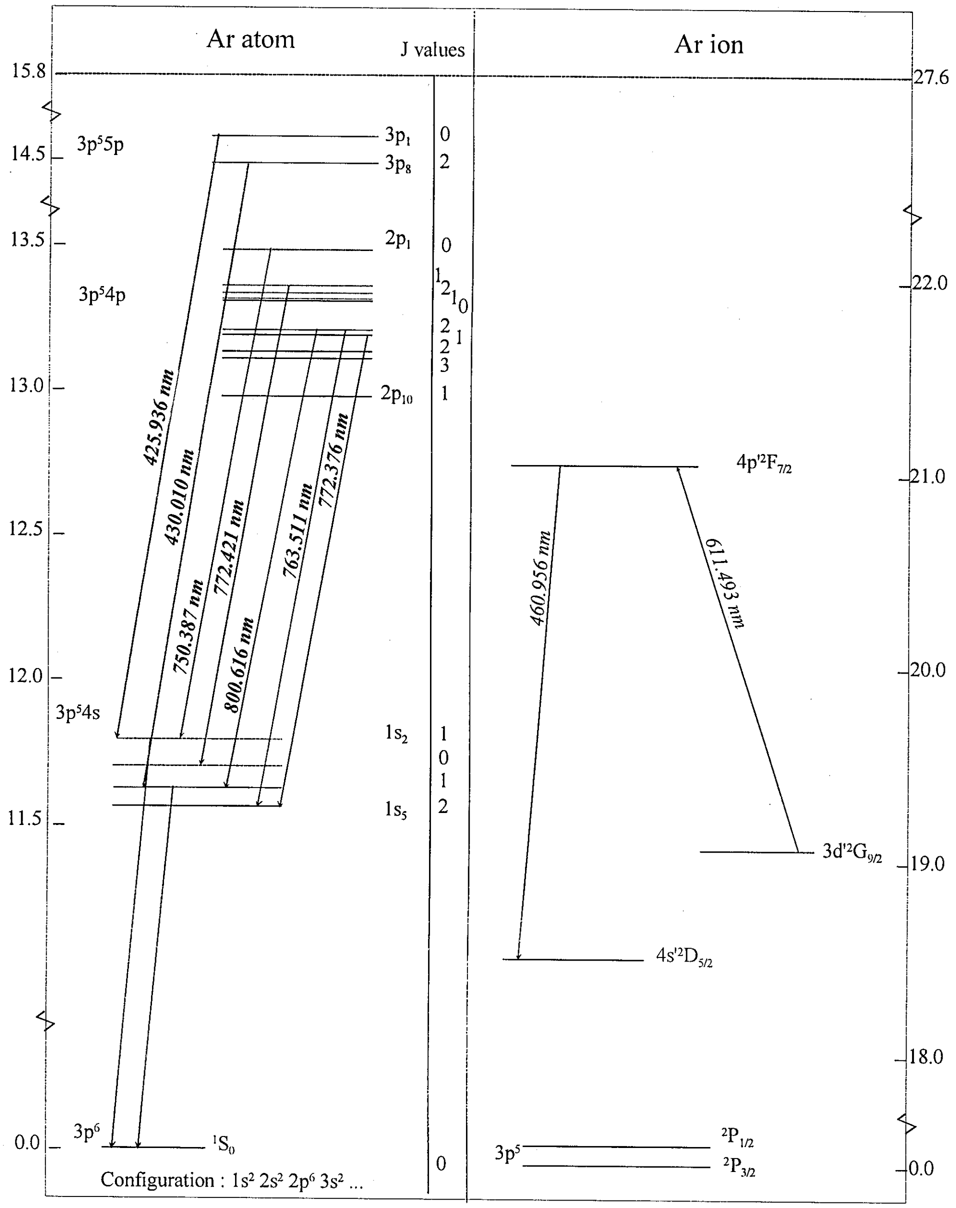

Argon energy level scheme

Figure A.4 : Argon level scheme.

References

[1] J.B. Boffard (Gaseous Electronics Conference 1997 : Madison (WI))

[2] S.R. Hunter and L.G. Christophorou, J. Chem. Phys. Vol. **80**, No. 12 (1984), pp6150-6164

[3] D. Rapp and P. Englander-Golden J. Chem. Phys. Vol. **43**, No. 5 (1965), pp1464-1479

[4] G. García and J. Campos, J. Quant. Spectrosc. Radiat. Transfer **34** (1985), pp85

[5] M.A. Lieberman, A.J. Lichtenberg, *Principles of plasma discharges and materials processing*, ISBN 0-471-00577-0, Wiley & Sons (1994)

[6] B. Pelissier and N. Sadeghi, Rev. Sci. Instrum **67** (1996), pp3405

[7] Shuji Sakabe and Yasukazu Izawa : Atomic Data and Nuclear Data Tables : Vol. **49** No. 2, (1991), pp257-314

[8] M.A. Biondi, Phys. Rev. **93** (1954), pp.1136

[9] Yuri P. Raizer : *Gas Discharge Physics* ; Springer Verlag

Appendix B: Used symbols and abbreviations

List of symbols

a	constant in probe theory
A	surface area [m^2], area element
A_H	area of top or bottom side of a cylinder [m^2]
A_p	area of probe tip [m^2]
A_R	area of sidewall of a cylinder [m^2]
A_{eff}	effective area [m^2]
A_{ki}	transition probability [s^{-1}]
b	constant in probe theory
b_0	classical distance of closest approach [m]
B_{ik}, B_{ik}	Einstein coefficients [$m^2J^{-1}s^{-1}$]
c	speed of light [$2.9979\ 10^8\ ms^{-1}$]
C_i	source term for population of level i
d	distance parameter [m]
d_{eff}	effective size [m]
D	diffusion coefficient [m^2s^{-1}]
D_a	ambipolar diffusion coefficient [m^2s^{-1}]
D_x	source term for diffusion and collisions [s^{-1}]
e	elementary charge [$1.6022\ 10^{-19}$ C]
$\mathbf{E}$,E	electric field [Vm^{-1}], energy [J]
E_e	electron energy [J]
E_{el}	energy loss per elastic collision [J]
E_{exc}	energy loss per excitation [J]
E_{iz}	energy loss per ionization collision [J]
E_c	total collisional energy loss per collision [J]
E_L	total energy loss per collision [J]
f_0, f_{ik}	oscillator strength
$f_v(v)$	velocity distribution function [m^2s]
F_r	reaction force [N]
g	distribution function [s]
g_i	statistical weight
G	Gaussian distribution function [s]
h	Planck's constant [$6.6262\ 10^{-34}$ Js]
h_H, h_R	density ratio between the sheath edge (at the sidewall (R) or top and bottom (H) of a cylinder) and the center of the plasma
H	height of a cylindrical reactor [m]
$\mathbf{H}$	Magnetic field strength [Am^{-1}]
I	intensity [Wm^{-2}]

I	current [A]
$I(\theta,v)$	differential cross-section [m^2]
$I_{e,i}$	electron and ion current [A]
I_{norm}	normalization current [A]
j_i	dimensionless ion current density
J_i	ion current density [$m^{-2}s^{-1}$]
k	Boltzmann constant [1.3807 10^{-23} JK^{-1}]
k	wave number [m^{-1}]
K	rate constant for collisions [$m^{-3}s^{-1}$]
K_{el}	rate coefficient for excitation [$m^{-3}s^{-1}$]
K_{exc}	rate coefficient for excitation [m^3s^{-1}]
K^{*}_{exc}	rate coefficient for excitation out of the ion ground state [m^3s^{-1}]
K_{iz}	rate coefficient for ionization [$m^{-3}s^{-1}$]
K_{rec}	rate coefficient for recombination [$m^{-3}s^{-1}$]
l	distance parameter [m]
L	characteristic length of the presheath [m]
L	Lorentz distribution function [s]
L_{beam}	loss term for beam electrons [Jm^{-1}]
L_c	collisional presheath length [m]
L_i	ionizing presheath length [m]
$m_{1,2}$	mass of particle 1,2 [kg]
m_e	electron mass [9.1095 10^{-31} kg]
m_i	ion mass [kg]
M	mass of atom [kg]
$n_{e,i}$	dimensionless densities of electrons and ions
n_-	dimensionless density of negative particles
N	density [m^{-3}], number of collisions
N_0	density of charged particles [m^{-3}]
$N^0_{e,i}$	electron and ion density in the center of the plasma [m^{-3}]
$N_{e,i,g}$	electron, ion and neutral gas density [m^{-3}]
N_{sH}, N_{sR}	sheath edge densities at the top and bottom (H) or at the sidewall (R) of a cylinder [m^{-3}]
p	dipole moment [Cm]
P	distribution function [s], transition probability [s^{-1}]
q	charge [C], dimensionless collision cross section
q_i	charge of particle i [C]
r	space coordinate [m], dimensionless ionization rate
R	rate [$m^{-3}s^{-1}$]
R	resistance [Ω]
R	radius of a cylindrical reactor [m]
R_0	equivalent resistance [Ω]
R_{rec}	recombination rate [s^{-1}]

R_{amb}	ambipolar diffusion loss rate [$\mathrm{s^{-1}}$]
S	total production rate [$\mathrm{s^{-1}}$]
$\mathbf{S}$	Poynting vector [$\mathrm{Jm^{-2}s^{-1}}$]
$S(\nu)$	saturation parameter
$S_{\mathrm{i,e,beam}}$	source term for the production of ions and (beam) electrons [$\mathrm{m^{-3}s^{-1}}$]
S_{α}	function in presheath theory
t	time [s]
T	time [s]
T	function in the LIF theory
$T_{\mathrm{e,i}}$	electron and ion temperature [K]
u	average ion velocity in the z-direction [$\mathrm{ms^{-1}}$]
U	interaction potential [V]
U_{f}	floating potential [V]
U_{plasma}	plasma potential [V]
$\mathbf{v}$	3-dimensional velocity vector [$\mathrm{ms^{-1}}$]
v_{B}	Bohm velocity [$\mathrm{ms^{-1}}$]
$v_{\mathrm{e,i}}$	electron and ion velocity [$\mathrm{ms^{-1}}$]
v_{z}	ion velocity in the direction of z [$\mathrm{ms^{-1}}$]
V	Voigt distribution function [s]
V	potential [V]
V	volume [$\mathrm{m^{3}}$]
V_{a}	voltage applied to double probe [V]
w	width of a laser beam [m]
W	energy [J]
W_{R}	kinetic energy of the collision particles in the center of mass system [J]
x	dimensionless presheath space coordinate
X	dimensionless variable in the ionizing presheath theory
y	dimensionless kinetic ion energy
z	space coordinate [m]
Z	charge number
Z	impedance [Ω]
α	ratio of negative particle temperatures
α	numerical factor
α_{iz}	ionization degree
β	index for various surface area configurations
χ	dimensionless potential
γ	adiabatic constant
γ	damping constant [$\mathrm{s^{-1}}$]
ε	ratio of Debye length and the characteristic presheath length
$\varepsilon_{\mathrm{beam}}$	energy of the beam electrons [J]
ε_0	dielectric constant [$8.8542\ 10^{-12}\ \mathrm{Fm^{-1}}$]

ϕ	potential [V]
ϕ	phase shift
η	coefficient in the LIF rate
κ	ratio of negative particle densities
κ	absorption coefficient [m^{-1}]
λ	distance parameter [m], wavelength [m], mean free path [m]
λ_c	ion mean free path for momentum transfer collisions [m]
λ_{ce}	ion mean free path for charge exchange collisions [m]
λ_D	Debye length [m]
λ_{el}	mean free path for elastic ion collisions [m]
λ_i	wavelength [m]
λ_i	mean free path of ions [m]
λ_m	mean free path between collisions [m]
μ	mobility [$m^2s^{-1}V^{-1}$]
ν	collision frequency for collisions [s^{-1}]
ν_0	central frequency [s^{-1}]
ν_m	momentum transfer collision frequency for collisions [s^{-1}]
θ	dimensionless effective negative particle temperature
θ	scattering angle
ρ	energy density per unit bandwidth [$Jm^{-3}s$]
σ	dimensionless ionization rate
σ	cross-section [m^2]
σ_i	ionization cross-section [m^2]
σ_m	momentum transfer cross-section [m^2]
σ_{sc}	scattering cross-section [m^2]
τ	mean time between collisions [s], time constant [s], life time [s]
ξ	time coordinate [s], dimensionless sheath space coordinate
ξ	displacement [m]
ω	oscillation frequency [s^{-1}]
$\omega_{pe,pi}$	electron and ion plasma frequency [s^{-1}]
ζ	random ion velocity in the z-direction [ms^{-1}]
ζ_L	fractional energy loss in hard sphere collisions
Φ	absorption function [Jm^{-2}]
Γ,Δ	width of a spectral profile [s^{-1}]
$\Gamma_{e,i}$	electron and ion flux [$m^{-2}s^{-1}$]
Λ_c	λ_D/b_0
Λ	diffusion length [m]

Abbreviations

cw	continuous wave
CCP	capacitively coupled plasma
DP	double probe
DSLIF	Doppler shifted laser induced fluorescence
ECR	electron cyclotron resonance
HDP	high density plasma
IC	integrated circuit
ICP	inductively coupled plasma
IR	infra red
ITF	ion transit frequency
IVDF	ion velocity distribution function
LIF	laser induced fluorescence
MIVDF	metastable ion velocity distribution function
OES	optical emission spectroscopy
OML	orbital motion limit
RIE	reactive ion etching
RF	radio frequency
SP	single probe
TSL	thin sheath limit
VDF	velocity distribution function

Summary

In this thesis the investigation of two plasma etch sources, which are operated at low pressures, is described.

In the first source a capacitively coupled plasma is created at 21 Pa argon pressure, using a 450 kHz RF voltage. The powered electrode is much smaller than the grounded one, resulting in a negative bias. This causes a thick sheath at the powered electrode, where the ions are accelerated. Due to the low applied frequency, the plasma is mainly sustained by the secondary or beam electrons, which are created at the surface of the electrode after ion bombardment. These electrons, which are accelerated in the sheath, give rise to a large time dependence in the excitation rates, which is observed experimentally in the time dependent optical emission signal.

Comparison of the excitation to various levels shows that some levels are not only excited from the ground state argon level, but also from the metastable levels, while others are not. The cross-sections for the excitation appear to follow the quantum rules for electric dipole transitions, which forbid the transition between two levels with $J = 0$.

Close to the powered electrode the fast ions create fast neutrals in charge exchange collisions. The fast atoms and ions can excite argon atoms to higher states. The excitation rate of this process depends on the energy of the fast particles, which is determined by the ratio of the electric field over the gas density. Closer to the electrode this ratio has a maximum, resulting in the highest production rate of excited states. This is clearly observed in the spatial dependence of the emission signal. Again the excitation rates are state dependent. The excitation by fast atoms and ions to the state with $J=0$ is not observed, while for the other states a clear maximum emission signal is found close to the electrode.

Also in the spatial profile of the metastable density, which is measured with IR absorption spectroscopy, a maximum is seen close to the electrode. The local density of this level is determined by the direct excitation from the ground state by collisions with fast atoms and neutrals as well as by radiative decay from higher excited levels, which in their turn are created by the same process.

With Doppler shifted laser induced fluorescence (DSLIF) the time resolved velocity distribution function (VDF) of metastable ions is measured at the transition between the negative glow and the sheath, including the presheath. The size of the sheath at the powered electrode is 8 mm at maximum for 18 W applied power. The size of the presheath, which is related to the mean free path of the ions, is in the order of 0.2 mm, which can not be resolved by DSLIF. Due to the short mean free path, the observed metastable ions are created locally by electronic excitation from the ground state atom. Again a clear time dependence in the metastable density is observed. Only during the most cathodic phase in the period the sheath extends to 8 mm from the powered electrode surface. Within their 250 ns life time, the metastable ions are accelerated and a clear velocity shift is observed at this position. Measurements at 9 mm show no velocity change, while closer to the electrode the ion density decreases and can not be

measured. The VDF of the metastable ions is not the same as that of the ground state ions. Although they are both created from the ground state atom, the metastable ions are quenched in collisions, while the ground state ions only change their velocity and travel across the sheath in several RF periods before reaching the electrode.
The spatial electron density and temperature are measured with a Langmuir probe.
A 1-dimensional fluid model shows the same spatial profiles for the ion and metastable density although the large uncertainty in the secondary emission coefficient gives rise to a difference in the absolute values of the densities. Also the time and spatially resolved excited state densities correspond well with the measured emission profiles. The excitation by fast atoms and ions, which causes the enhanced densities at the powered electrode, is not taken into account in the model.

The second source is an inductively coupled plasma (ICP), which uses a three-turn helical coil to create a 13.56 MHz magnetic field in the plasma region leading to an electric field which heats the electrons. A Faraday shield blocks the capacitive coupling. The source is operated at low pressures (0.1-4 Pa) which causes the mean free path of the ions to be comparable to the reactor dimensions. The presheath, therefore, extends to the middle of the plasma. The sheath thickness is in the order of the Debye length, which is tens of micrometers thin.
The same set of diagnostic tools is applied to this source. Langmuir probe measurements show the pressure and power dependence of the electron density and temperature. They correspond well to the values predicted by a global model, which only takes into account losses by ambipolar diffusion. Emission experiments show that excited ion states are mainly created from the ion ground state. The spatial profile of emission from atomic lines follows the electron density and from this the electric field can be deduced.
DSLIF is used to measure the VDF of metastable ions. The acceleration of the ions is observed from the middle of the plasma to the sheath edge, where the ions exceed the Bohm velocity. Inside the presheath collisions and ionizations take place, which give rise to ions having zero velocity components. In the measured metastable ion distribution function this is not observed. Due to their long mean free path, the local production of metastable ions in the observation region is much smaller than the flow of particles which are created earlier. A Monte Carlo model is used to show the relation between the VDF of the ground state ions and the metastable ions. It points out that the ground state ions have a zero velocity component and the average velocity exceeds the Bohm velocity much closer to the electrode. The metastable ion VDF as calculated by the model fits well with the measured curves.

The two low pressure etch sources show some clear differences. In the capacitively coupled source, the ions hit the electrode with large energies, due to the large voltage needed to obtain a sufficiently high ion density. In the ICP source the ions arrive at the electrode with only a small energy, which can be tuned by applying a bias voltage. In the 450 kHz source the plasma is mainly sustained by the electrons which are created at the electrode by secondary emission, induced by ion bombardment. These electrons are accelerated in the sheath and cause a large time dependence of the emission signal. In the ICP source the electrons are heated directly by the inductive field.

Samenvatting

In dit proefschrift wordt het onderzoek aan twee lage-druk-etsplasma's beschreven.
Het *eerste*, een 21 Pa capacitief gekoppeld argonplasma, wordt opgewekt met een radiofrequente (RF) 450 kHz wisselspanning. Het oppervlak van de bekrachtigde elektrode is veel kleiner dan de geaarde vlakken in het plasma, wat leidt tot een negatieve offset-spanning. Als gevolg daarvan strekt de grenslaag, waarin de ionen versneld worden, zich uit tot enkele millimeters van het elektrode oppervlak. De lage frequentie veroorzaakt dat het plasma voornamelijk door de secundaire elektronen in stand wordt gehouden, die tijdens het ionenbombardement vrijkomen van het elektrode-oppervlak. Deze elektronen worden versneld in de grenslaag, waardoor het excitatieproces een zeer sterke tijdsafhankelijkheid vertoont. Dit is duidelijk te zien in de tijdsopgeloste optische emissiemetingen.
De vergelijking van excitaties naar verschillende niveaus leert dat deze niveaus niet alleen gevormd worden vanuit de grondtoestand, maar ook vanuit metastabiele toestanden. De excitatiesnelheden blijken de selectieregels voor optische overgangen te volgen, welke de overgang van een niveau met J=0 naar een ander niveau met J=0 verbieden.
Dicht bij de bekrachtigde elektrode worden bij botsingen van energetische ionen met atomen snelle neutralen gevormd door middel van ladingsruil-processen. Deze snelle neutralen en ionen kunnen andere atomen door excitatie in een aangelagen toestand brengen. De excitatiesnelheid van dit proces hangt af van de energie van de snelle deeltjes, die bepaald wordt door de verhouding tussen de sterkte van het elektrische veld en de gasdichtheid. Deze verhouding is vlak voor het elektrode-oppervlak maximaal, waardoor daar de productie van geëxciteerde niveaus het hoogst is. Dit effect is duidelijk te zien in het plaatsopgeloste emissiesignaal. Ook hier zijn de excitatiesnelheden afhankelijk van de begin- en eindtoestand. De excitatie van een niveau met J=0 naar een ander niveau met J=0 is niet zichtbaar, terwijl andere overgangen duidelijk vlak voor het elektrode-oppervlak een maximum in het emissiesignaal laten zien.
Ook in het tijdsopgeloste dichtheidsprofiel van de metastabiele atomen (gemeten met infrarood spectroscopie) is een duidelijk maximum vlak voor het elektrode-oppervlak te zien. De lokale dichtheden van de metastabiele niveaus worden bepaald door botsingen van snelle neutralen en ionen met atomen en door stralingsovergangen vanuit hogere toestanden, welke door hetzelfde proces worden gevormd.
Met Doppler shifted laser induced fluorescence (DSLIF) is de tijds- en plaatsopgeloste snelheidsverdeling van metastabiele ionen bepaald in de overgang van het plasma naar de grenslaag, inclusief de "presheath". De dikte van de grenslaag voor de bekrachtigde elektrode is maximaal 8 mm voor een argonplasma van 18 W. De dikte van de "presheath", die bepaald wordt door de vrije weglengte van de ionen, is ongeveer 0.2 mm, wat kleiner is dan de resolutie van de DSLIF meting. Door de korte vrije weglengte zullen de gemeten metastabiele ionen lokaal gevormd zijn uit de atomaire

grondtoestand. Ook hier is er een sterke tijdsafhankelijkheid in de dichtheid van de metastabiele ionen gemeten. Alleen tijdens de fase waarin de elektrodespanning uiterst negatief is, strekt de grenslaag zich uit tot 8 mm van het elektrode-oppervlak. Tijdens de levensduur van de metastabiele ionen (250 ns) worden de deeltjes versneld en is een verschuiving van de snelheidsverdeling gemeten. Metingen op 9 mm afstand van de elektrode laten geen versnelling van de ionen zien, terwijl op posities dichter bij de elektrode de dichtheid van de metastabiele ionen dramatisch zakt en niet meer gemeten kan worden. De snelheidsverdeling van de metastabiele ionen is niet dezelfde als van de ionen in de grondtoestand. Hoewel ze beide gevormd worden vanuit de atomaire grondtoestand veranderen de metastabiele ionen van toestand tijdens een botsing terwijl voor de ionen in de grondtoestand alleen hun snelheid verandert. Zij versnellen in de grenslaag tijdens meerdere RF perioden, voordat ze op het elektrode-oppervlak terecht komen.

De plaatsafhankelijkheid van de elektronendichtheid en -temperatuur is bepaald met een Langmuir sonde.

Een eendimensionaal vloeistofmodel levert dezelfde dichtheidsprofielen op als de metingen, hoewel de onzekerheid in de secundaire emissiecoëfficiënt leidt tot een andere absolute dichtheidswaarde. Ook de tijds- en plaatsopgeloste dichtheidsprofielen komen goed overeen met het gemeten emissiesignaal. Het maximum vlak voor het elektrode-oppervlak, veroorzaakt door botsingen van snelle atomen en ionen, is niet berekend uit het model, omdat dit proces niet in het model opgenomen is.

Het *tweede* plasma is opgewekt in een inductief gekoppelde plasmareactor. Deze bron gebruikt een spoel met drie windingen om een 13.56 MHz magnetisch veld in de plasmakamer op te wekken. Dit induceert een elektrisch veld dat de elektronen laat versnellen. De bron gebruikt lage argondrukken (0.1 - 4 Pa), waardoor de vrije weglengte van de ionen vergelijkbaar wordt met de reactorafmetingen. De "presheath" zal zich daardoor uitstrekken tot het midden van het plasma. De dikte van de grenslaag is slechts ongeveer gelijk aan de Debye-lengte, welke enkele tientallen micrometers bedraagt.

Dezelfde diagnostische technieken zijn gebruikt voor deze reactor. De Langmuir sonde meet de druk- en vermogensafhankelijkheid van de elektronendichtheid en -temperatuur. De resultaten komen goed overeen met een globaal model dat alleen het verlies van geladen deeltjes door ambipolaire diffusie meeneemt.

Emissiespectroscopie laat zien dat de aangeslagen ion-toestanden voornamelijk vanuit de ion-grondtoestand gevormd zijn. De plaatsafhankelijkheid van de emissie door atomaire overgangen is evenredig met de elektronendichtheid, waaruit het elektrische veld afgeleid kan worden.

DSLIF is gebruikt om de snelheidsverdeling van metastabiele ionen te bepalen. De versnelling van een ion vanuit het midden van het plasma tot aan de rand van de "presheath" wordt gevolgd totdat het deeltje de Bohmsnelheid heeft en overgaat naar de grenslaag. Als gevolg van ionisatie en botsingen in het "presheath"-gebied zullen er

ionen in de grondtoestand met een lage snelheid gevormd worden. In de snelheidsverdeling van de metastabiele ionen is dit effect echter niet gemeten. Door de grote vrije weglengte van de deeltjes zal de lokale productie van metastabiele ionen in het observatiepunt veel kleiner zijn dan de instroom van eerder gevormde en inmiddels versnelde deeltjes.
Om het verband tussen de snelheidsverdeling van metastabiele- en grondtoestand-ionen te onderzoeken is gebruik gemaakt van een Monte Carlo-model. De resultaten laten zien dat de snelheidsverdeling van ionen in de grondtoestand een duidelijke nul-snelheidscomponent hebben en dat hun gemiddelde snelheid vlak voor het elektrode-oppervlak gelijk wordt aan de Bohmsnelheid. De door het model bepaalde snelheidsverdeling van de metastabiele ionen komt goed overeen met de gemeten curven.

Er is een aantal duidelijke verschillen tussen de twee onderzochte lage-druk-etsplasma's. Door de hoge spanning, die nodig is om een voldoende hoge ionendichtheid te creëren, treffen de ionen het elektrode-oppervlak met een hoge snelheid. In het inductief gekoppelde plasma treffen de ionen de elektrode met een lage snelheid, die bepaald kan worden door de elektrodespanning. Het 450 kHz plasma wordt voornamelijk in stand gehouden door de secundaire elektronen, die gevormd worden door het ionen-bombardement. Deze elektronen worden versneld en veroorzaken een sterke tijdsafhankelijkheid. Bij het inductief gekoppelde plasma worden de elektronen direct verhit door het inductieve veld.

Dankwoord

Nu dat mijn proefschrift na vier jaar onderzoek voor u ligt, is ook een woord van dank op zijn plaats voor allen die hebben meegeholpen aan de totstandkoming van dit werk. Allereerst wil ik Jackeline bedanken voor de steun die zij mij in deze tijd heeft gegeven. Zij voelde als geen ander aan hoe belangrijk het is om af en toe afstand van het werk te kunnen nemen en samen andere dingen te gaan doen. Mijn ouders stonden aan de basis van mijn opleiding. Zij waren er altijd om advies te geven en om me aan te moedigen in het maken van de juiste keuzen.

Ik wil Frits de Hoog en Gerrit Kroesen bedanken voor de begeleiding tijdens mijn onderzoek. Ook de andere leden van de groep Elementaire Processen in Gasontladingen hebben hun bijdrage geleverd aan de totstandkoming van dit werk. Dankzij Lambert Bisschops, Hans Freriks en de mensen van de werkplaats werden technische problemen vaak snel opgelost. Stéphan Vernay, Marie-Claude Peignon, Edwin Knols en Alison Loudon hebben allen een deel van het werk op zich genomen.

I would like to thank Tarik Hbid for his work on the modeling site of this thesis.

Daarnaast hebben Rina Boom, Marianne van den Elshout, Marco Haverlag, Rob Snijkers, Hans den Boer, Ewa en Winfred Stoffels, David Vender, Milan Hain, Akihiro Kono, Tad Adamowicz, Frank Commissaris, Holger Kersten, Geert Swinkels, Marcel Hemerik, Gerjan Hagelaar, Leon Bakker, Wilfred Hoeben, Eddy van Veldhuizen, Wijnand Rutgers, Loek Baede, Gijs Meeusen en vele anderen gezorgd voor een gezellige sfeer in de groep.

I especially would like to thank Nader Sadeghi for his cooperation. His help has been of great value and has lead to the understanding of the difference between apples and pears.

Tenslotte wil ik iedereen, die in de afgelopen jaren geïnteresseerd was in mijn werk, in mijn dankbaarheid betrekken.

Over de auteur

Marc van de Grift is op 21 juli 1970 in Eindhoven geboren. Na een groot aantal jaren spelend te hebben doorgebracht, is hij in 1982 begonnen aan het atheneum van het Anton van Duinkerken College te Veldhoven. Nadat hij het eindexamen in 1988 met goed gevolg had volbracht is hij verder gegaan op de Technische Universiteit Eindhoven, waar hij de studie Technische Natuurkunde heeft gevolgd. Na het behalen van de ingenieurstitel is hij als Assistent in Opleiding (AIO) voor vier jaar bij de groep Elementaire Processen in Gasontladingen (EPG) gaan werken. Dit proefschrift is de afsluiting van deze periode, waarmee de titel doctor is verworven.

Stellingen

behorende bij het proefschrift :

"A diagnostic Study on Two Low Pressure Plasma Sources"

Marc van de Grift

1 december 1997

1) Als in een plasma van lage druk de vrije weglengte van ionen van dezelfde orde wordt als de reactorafmetingen bevat het plasma geen glimlicht, maar strekt de presheath zich uit tot het midden van het plasma. *Hoofdstuk 6 van dit proefschrift.*

2) Bij het toepassen van Doppler-verschoven laser geïnduceerde fluorescentie (DSLIF) voor het meten van deeltjessnelheden in plasma's moet men voor wat betreft de laserintensiteit een compromis sluiten tussen enerzijds het verlangen naar een groot fluorescentiesignaal en anderzijds het verlangen naar een goede oplossing in de snelheidsruimte. *Hoofdstuk 4 van dit proefschrift.*

3) Bij de toepassing van DSLIF voor de bepaling van de snelheidsverdelingsfunctie van argon ionen wordt er vaak ten onrechte van uit gegaan dat de metastabiele ionen representatief zijn voor de ionen in de grondtoestand. *Dit proefschrift.*

4) Bij de toepassing van het Bohm criterium moeten alle ionen meegenomen worden en niet slechts een deelverzameling. *Hoofdstuk 6 van dit proefschrift.*

5) Een muzikant die in zijn jeugd deelneemt aan een aantal solistenconcoursen heeft later minder moeite met het spreken voor grote groepen mensen.

6) Voor de zoektocht naar de goedkoopste hypotheek is een bezoek aan een hypotheekadviseur over het algemeen slechts goed voor de bepaling van de bovengrens.

7) Het gebruik van real-time video- en audio-applicaties via het internet verlangt niet alleen een verbetering van de hard- en software, maar ook een (tot nog toe uitblijvende) verandering in het communicatieprotocol.

8) De toepassing van het internet in zijn huidige vorm voor iedereen maakt het principe van "voordeurdelen" noodzakelijk, omdat er maar 4 miljard internetadressen voorhanden zijn.

9) De historisch bepaalde plaats van de CapsLock-toets op een toetsenbord is een aanleiding tot typefouten.

10) Bij snelheden te land in de buurt van de geluidssnelheid is het beter om het Mach-getal als snelheidsmaat te gebruiken dan de snelheid ten opzichte van de lucht, omdat de ontwikkeling van supersone schokgolven van grote invloed is op de beweging van het voertuig. *http://thrustssc.digital.co.uk*

11) In de loodgietersbranche worden medewerkers met weinig ervaring vaak eerst op "leiding-gevende" posities ingezet.